Characterization of CdTe Based Photodetectors, ZnO Nanowires and Nanostructures for Photonic Applications

BY

SIDRA FARID
M.S., University of Engineering & Technology, Lahore, 2009.
B.Sc., University of Engineering & Technology, Lahore, 2006.

THESIS

Submitted as partial fulfillment of the requirements
for the degree of Doctor of Philosophy in Electrical and Computer Engineering
in the Graduate College of the
University of Illinois at Chicago, 2016

Chicago, Illinois

Defense Committee:

Mitra Dutta, Chair and Advisor
Michael A. Stroscio
Vitali Metlushko
Zheng Yang
Alan Nicholls, Research Resource Center, UIC

This thesis is dedicated to my parents, Mr. Javaid Alam and Mrs. Farhat Javaid, who gave me so much love and encouragement from my childhood until now. I also dedicate this to my husband Farid Pasha for being by my side throughout this long journey with patience, dedication, love and support.

ACKNOWLEDGEMENTS

I would first like to thank my advisor, Prof. Dr. Mitra Dutta, for her continuous guidance, immense support and trust in me. I feel very fortunate to work under her guidance, thank you for giving such a free hand and flexibility in conducting research projects and always encouraging and correcting me. I can't thank you enough for allowing me to avail the internship opportunities I got during my doctoral studies at Intel Corporation, and Facebook, Inc. CA and supporting me through out that time which were a life time game changer experiences for me. I still remember how you encouraged me and helped me settle down when I first brought my family in USA. You are a great person and your wisdom, vision, administration and especially leadership will benefit me in my future life and will serve as a great inspiration for me.

Many long days were spent at the Center for Nanoscale Materials Division (CNM) at Argonne National Laboratory (ANL) working to make the in plane cylinders into standing ovation. The end result would not have been possible without the experience and guidance of Dr. Seth Darling at CNM Division of ANL. I would like to express my sincere thanks to Seth for providing me the opportunity to work under his guidance and making me use every possible equipment needed for research at CNM. I would also like to thank the post docs Wei Chang and Maxim with whom I have collaborated during my project working on gold nanoparticles synthesis using block co polymer nanolithography at ANL.

ACKNOWLEDGEMENTS (continued)

I would also like to thank Prof. Dr. Michael Stroscio for providing helpful insights when I started studying phonon modes in CdTe/CdS thin films, for his brilliant classes in quantum physics and for his useful discussions during group meetings. I would especially like to extend my appreciation to Dr. Zheng Yang whose classes on device fabrication were particularly helpful to me in learning the basics. Thanks for all the help and guidance in troubleshooting PL setup and sharing his expertise with us. I learned tremendously having informative discussions with him anytime I need and he is always willing to help. I thank Prof. Vitali Metlushko for serving on my thesis committee and taking time to go over my thesis. I would also like to thank Dr. Alan Nicholls at the Research Resource Center at UIC for being on my thesis committee as well as for helping me in performing TEM and Raman spectroscopy and for the data analysis.

I would also like to thank the entire graduate students with whom I have worked alongside in Dr. Dutta's and Dr. Stroscio's lab. My sincere thanks to some of my senior fellows at UIC such as Hyeson Jung, Banani Sen and Mohsen Purahmed who helped me in the start of my PhD and also to my fellow graduate students Souvik, Min, Mojgan, Ketaki, Elaine, Debopam and former students Xenia, Robin, Shripriya, Undarma and Rade. To them, I looked towards for friendship, insight and camaraderie. My special thanks to Souvik for being a great lab mate, and for always being very helpful. I also had the opportunity to work alongside with many world class individuals during my internships at Intel and Facebook. I would specially like to thank Roshan George for

being a great mentor I could have asked for. Thank you for showing great opportunities to me and making me work to the best of my abilities. I would also like to thank Jeffrey Driscoll for being a great teacher and friend at the same time, and extend my appreciation to all my coworkers as well especially Dr. Kang and Krishna. My acknowledgment would be less if I don't thank Srinivasan Giridharan for being a true inspiration for me. Thanks Sri for the guidance and setting an example of how to respect everyone and their opinions. You are truly an inspiration, a great mentor and a legend for the team. Thanks Katharine and Abhijit for all your help, guidance and useful discussions. I have learnt a lot from you!

Finally I would like to thank my family and dedicate this thesis to them. My mom, dad, sisters, brother and my in-laws, thank you for your warmth, love and support. To my husband Farid Pasha, who has always been by my side in this whole journey, truly believing in me, supporting me, encouraging me during rough days, taking care of our boys throughout my research and especially during long internship days. You are the right combination of love, encouragement and motivation whenever I needed. My boys- my world, Noor and Rahim, I would be less without you all.

Thank you.

SF

Table of Contents

CHAPTER PAGE

1. INTRODUCTION 1
1.1. Nanotechnology: A Disruptive Technology 1
1.2. CdTe based photodetectors 1
1.3. History and modern use of metallic nanoparticles 4
1.4. Block co polymer nanolithography 5
1.5. Semiconductor nanowires 8
1.6. Doping in Zinc oxide 10
1.7. Structure of this thesis 10

2. MULTIPHONON RAMAN SCATTERING AND PHOTOLUMINISCENCE STUDIES OF AS-GROWN AND ANNEALED CADMIUM SUPLHIDE NANOCRYSTALS 12
2.1. Purpose of annealing CdS thin films 13
2.2. Experimental 13
2.3. Results and Discussions 14
2.3.1. Optical Phonon Modes investigation using Raman Spectra 14
2.3.2. Spatial Correlation Model 16
2.3.3. Photoluminescence spectra 18
2.3.4. Excitation dependence of the Raman and Luminescence Signals 20
2.4. Conclusions 22

3. ANALYSIS ON THE STRUCTURAL, VIBRATIONAL AND DEFECT STATES OF CHLORINE TREATED CADMIUM TELLURIDE STRUCTURES 23
3.1. Advantage of using e-beam evaporation for CdTe deposition 23
3.2. Challenges with polycrystalline CdTe thin films 24
3.3. Fabrication procedure 25
3.4. Results and Discussions 26
3.4.1. Low Temperature Photoluminescence Characterization 26
3.4.2. Raman analysis on the CdTe films 31
3.4.3. Quasi Phonon Modes 32
3.5. Conclusions 34

Table of Contents (continued)

CHAPTER PAGE

4. SYSNTHESIS OF UNIFORM GOLD NANOPARTICLE ARRAYS AND NANOPOROUS TEMPLATES USING BLOCK CO POLYMER LITHOGRAPHY ... 35
4.1. Experimental Protocol ... 36
4.2. Preparation and neutralization of substrate ... 37
4.3. Application and orientation of block copolymer (PS-b-PMMA) nanostructures ... 38
4.4. Nanopatterning ... 39
4.5. Applications in fabricating hybrid photovoltaic cells ... 41
4.6. Conclusions ... 42

5. ZINC OXIDE NANOWIRES: OPTICAL, STRUCTURAL AND ELECTROSTATIC FORCE ANALYSIS UNDER DIFFERENT GROWTH CONDITIONS ... 44
5.1. Growth mechanism of ZnO Nanowires ... 45
5.2. Experimental procedure for growth of ZnO nanowires ... 47
5.3. Investigations into growth conditions and structures of ZnO Nanowires ... 48
5.4. Photoluminescence studies of ZnO Nanostructures ... 57
5.5. Raman studies of ZnO Nanostructures ... 62
5.5.1. Raman of As-grown Nanowires ... 62
5.5.2. Raman spectra at varied growth times ... 66
5.6. Electrostatic force analysis for zinc oxide nanowires and nanostars ... 67
5.6.1. Spontaneous Polarization in ZnO ... 67
5.6.2. Electric field estimation from Electrostatic Force analysis ... 69
5.7. Conclusions ... 75

6. INDIUM INCORPORATED ZINC OXIDE NANOWIRES ... 76
6.1. Background on Indium doped zinc oxide nanostructures ... 76
6.2. Experimental ... 79
6.3. Results and Discussions ... 80
6.3.1. Structural Analysis of Indium doped ZnO NWs ... 80
6.3.2. Defect State analysis of Indium doped ZnO NWs ... 83
6.3.3. Effect of indium doping Concentration variations ... 90
6.3.4 Zinc-indium oxide as a promising candidate of TCO ... 91
6.4. Conclusions ... 93

Table of Contents (continued)

CHAPTER PAGE

7. CONCLUSIONS AND FUTURE WORK 95
7.1. Conclusions 95
7.2. Future Work 99

APPENDICES 101
APPENDIX A 102
APPENDIX B 103
APPENDIX C 104
APPENDIX D 105

CITED LITERATURE 106

VITA.. 117

List of Figures

FIGURES PAGE

1: Schematic illustration of formation of gold nanoparticles utilized in this work.....8

2: Room temperature Raman spectra of the as grown and annealed films excited using 514 nm laser..... 15

3: 1-LO phonon mode peak fitting using SCM for the a) as grown and b) annealed. 17

4: Photoluminescence spectra for the as grown (solid line, lower spectra) and annealed CdS films (solid line, top spectra) at 441.6 nm laser line excitation while Lorentzian modes for annealed films are shown by dotted lines. 19

5: Raman spectra at varied excitation power (decreasing power from top to bottom curve). 21

6: (a) PL spectra of CdS as grown films excited at varied laser power (decreasing power from top to bottom curve) using neutral density filters; (b) Variation of laser power on the photo luminescence integrated intensity area of dominant PL peak (straight line indicated linear fit)..... 22

7: PL spectrum of the chlorine treated CdTe sample at 10 K including the Gauss profiles fit. The inset shows a magnification of the 1.55 – 1.56 emission range. 27

8: AFM measurements of a) CdTe without CdCl2 annealing treatment: grain size 0.2 μm b) CdTe with $CdCl_2$ annealing treatment: grain size 2-3 μm. 29

9: a) Low temperature (10K - 90K decreasing order) photoluminescence spectra for the annealed CdTe films with at 633 nm laser line excitation. The inset shows a magnification of the 1.55 eV – 1.61 eV range. b) Temperature dependence of emission bands at 1.5577 eV and 1.45 eV for extrapolating activation energies. 31

10: Raman spectrum of polycrystalline CdTe thin films excited using 633 nm laser line..... 32

11: Schematic illustration of process flow for the formation of gold nanoparticles using block copolymer nanolithography..... 36

12: (a) Atomic force micrograph (topography) of a self-assembled BCP film (in-plane cylinders) obtained by direct application of BCP on the ITO surface, (b) Atomic force micrograph of a self-assembled BCP film on ITO (standing cylinders) after RCP surface. 39

List of Figures (continued)

FIGURES PAGE

13: (a) AFM height image of closely packed nanoscale pores of diameter 25 - 30 nm following RIE treatment of the BCP film (now comprised of PS only) (b) AFM height image of the textured film following Au deposition. 40

14: AFM topographic image of <30 nm Au nanodot array following the liftoff procedure. 41

15: Schematic illustration for the future steps of CdS/polymer based hybrid PV device. 42

16: Schematic of VLS growth setup. 48

17 (a)-(b): Sample A: SEM images showing inappropriate growth of zinc oxide nanowires at different scale bars 49

18 (a)-(d): Sample B: SEM images of ultra long As-grown ZnO NWs under appropriate growth conditions with different scale bars images (5, 10, 20 & 50 μm respectively). 50

19: a) Selected area electron diffraction pattern (SAED) of ZnO nanowire; inset shows a TEM image of a single nanowires; b) Lattice fringes from a ZnO nanowire; c) XEDS profile of as grown ZnO nanowires showing zinc, oxygen and carbon content taken from a SEM operating at 5 keV. 51

20 (a)-(d): Sample C: Over growth of zinc oxide nanowires at different scale bars; highlighted area in figure 20(d) indicates excessive growth layer on top of ZnO nanobelt-like structures. 52

21: Sample D: Star-shaped formation of Zinc oxide Nanostructures; a) 0 degree angled image; b) 40 degrees angled image. 53

22: Schematic illustration of growth mechanism of star shaped zinc oxide nanostructures. 55

23: TEM images of (a)-(b) ZnO star showing corners of six legs marked; (c),(e),(f) HRTEM image showing lattice fringes of the selected area; (g),(e)-(f) SAED patterns of different areas of stars as indicated in image (b) 56

24: Room temperature photoluminescence spectra of ZnO nanowires and ZnO stars excited at 325 nm laser. 58

List of Figures (continued)

FIGURES PAGE

25: Photoluminescence spectra of ZnO nanowires with 50-100 nm diameter and ZnO nanowires with 500 nm diameters excited at 325 nm laser. 59

26: Room temperature PL spectra of as grown nanowires at densely packed (top curve) and less dense regions (bottom curve) of nanowires excited by 325 nm laser line. 60

27: Room temperature PL spectra of ZnO nanowires annealed at 500 ^{o}C and 700 ^{o}C in oxygen for 2 hr. 61

28: Raman spectrum of ZnO nanowires having 50 -80 nm diameters. 63

29: Raman spectrum of ZnO nanowires on decreasing laser excitation power from 100 % (top curve) to 75%, 50%, 25% and 1%. 65

30: a) Raman spectrum of ZnO nanowires and Si at varied growth times ranging from 5 – 60 min; b) Offset y-axis for clarity. 67

31: Schematic illustration of (a) growth direction and c-axis for ZnO NW; (b) Different scenarios for the net dipole moments (DM) of random orientations of a ZnO NS [82] 69

32: SEM image of a (a) single nanowire; (b)-(c) Nanostar dropped on gold coated substrate after scratching the sample for AFM measurements. 70

33: Typical AFM patterns with corresponding height profiles for selected (dashed lined) regions of (a) a gold coated Si substrate (b) ZnO NW; (c) ZnO NS [82] 71

34: a) Interleave amplitude for Si and gold coated substrate for reference; b) Interleave amplitude for ZnO NW with red solid circles indicating areas of NWs, subset indicates SEM image of a single NW; c) Interleave amplitude for ZnO NS with small red solid circles indicating single NS areas while bigger red circle indicating multiple stars as shown by SEM images in subsets; (d)-(f) Displacement profile images for the Si+Au substrate, NW and NSs respectively whereas dashed and solid lines in (a)-(c) indicate areas scanned for displacement profiles 73

35: SEM image of a) ZnO NWs; b) IZO NWs and NBs; c) IZO NWs with ~50-100 nm diameter; d) IZO NBs with ~500 nm diameter. 80

List of Figures (continued)

FIGURES PAGE

36: a) TEM image of IZO nanowires showing lattice spacing of 0.294 nm; b) TEM image of undoped ZnO nanowires with 0.283 nm lattice spacing; c) SAED pattern for indium doped zinc oxide nanostructures; d) TEM image of 100 nm IZO NW (inset shows Fast Fourier transform measurements for IZO nanostructures); e) TEM image of a non-uniform IZO NB; f) EDX profile for obtaining elemental composition of IZO nanostructures..... 82

37: a) Room temperature (RT) PL spectra for the ZnO & IZO NWS; ZnO VE is fitted with Gaussian fit to account for peak variances; Inset indicates schematic of possible transitions from ZnO structures, (NBE emission at 3.25 eV, oxygen antisite (O_{Zn}), oxygen vacancies (V_o) or Zinc vacancies (Zn_o), Zinc antisites in the oxide (Zn_i)); b) PL spectra at 20K for ZnO & IZO NWs with Gaussian peak fits presented for IZO nanowires. 86

38: a) Temperature dependent PL spectra of a) ZnO; b) IZO NWs (The inset shows temperature dependence of DAP on PL intensities) 89

39: a) Photoluminescence spectra for the 3% - 15% wt. indium doped ZnO nano structures; b) Plot of photon energy on variation of indium oxide concentration in ZnO.91

40: Optical transmittance data for doped and undoped doped zinc oxide nanostructures. 93

LIST OF ABBREVIATIONS

1D	1-Dimensional
Ar^+	Argon Ion
AFM	Atomic force microscopy
BCP	Block copolymer
CCD	Charge Coupled Detector
CBD	chemical bath deposition
CSS	closed-space sublimation
DAP	Donar-acceptor pair
EBE	electron beam evaporation
EDS	Energy Dispersive Spectroscopy
FWHM	Full Width Half Maximum
HeCd	Helium Cadmium
HRTEM	High-Resolution Transmission Electron Microscopy
IR	Infrared
IZO	Indium zinc oxide
LED	Light emitting diode
mW	milli Watt
NBE	Near band edge
NB	Nanobelt
NS	Nanostar
NW	Nanowire
PL	Photoluminescence
PS-b-PMMA	Polystyrene-block-Poly methyl metha acrylate
PS-r-PMMA	Polystyrene-random-Poly methyl metha acrylate
RIE	Reactive ion etching
SEM	Scanning Electron Microscope
SAED	Selected area electron diffraction

LIST OF ABBREVIATIONS (continued)

STEM	Scanning Transmission Electron Microscopy
SCM	Spatial correlation model
TCO	Transparent conductive oxide
TE	Thermal evaporation
TEM	Transmission Electron Microscopy
UV	Ultraviolet
VLS	Vapor Liquid Solid
ZnO	Zinc oxide

SUMMARY

Cadmium telluride (CdTe) has been regarded as a promising semiconductor material for the detection of infrared (IR) radiations, hard *X*-rays, *γ*-rays and also in photovoltaics applications. As compared to Silicon based detectors, CdTe possess higher atomic no.s of Cadmium (Z_{Cd}: 48) and Tellurium (Z_{Te}: 52) and large energy band gap at room temperature (~1.45 ev) that makes it a favorable material that could achieve higher quantum efficiencies. Despite the wonderful charge transport properties and energy resolution of Silicon (Si) and Germanium (Ge) based photodetectors, its applications are limited for radiation detection due to their indirect bandgap and low stopping power for higher energetic photons. If we consider Hg based CdTe structures (HgCdTe detectors) for infrared (IR) detection, or CdTe/CdS based photovoltaic cells, an important limiting factor for device performance is recombination and noise limitations. Problems and efforts to improve the properties of CdTe thin films are discussed in this thesis. We propose a method to study and optimize electrical and optical parameters of individual layers of CdTe/CdS based devices that can help tremendously improve the performance and thus enhance the overall efficiency of cells. We have employed e-beam evaporation technique which has not been paid much attention in the past for growing CdTe thin films and reported excellent film quality. Detailed analysis of the structural, defect states and vibrational characteristics of chlorine treated polycrystalline CdTe thin films has been done using photoluminescence measurements, Raman analysis and atomic force microscopy. We have also characterized

the CdS layer used for fabricating CdTe/CdS based devices and analyzed the effects of annealing and excitation dependent input by using optical characterization techniques and presented a model for evaluating Raman line shape of phonon modes with spatial correlation model that matches well with the experimental data. This analysis can also be applied for other kinds of CdTe based detectors such as HgCdTe for IR detection, X-ray and γ-ray detections and for photonics applications.

Further blockcopolymer lithography self-assembly approach that has obtained significant attention in the past years as a candidate to overcome the limits imposed by conventional lithography technique is utilized to obtain highly ordered nanostructures of metal nanoparticles, expected to be more robust in comparison. Successful fabrication of gold nano particles using properties of the block co polymer self-assembling into highly ordered and periodic nanodomain is achieved. These materials can serve as templates for various applications in optoelectronics devices or can also be utilized in the vapor-liquid-solid (VLS) growth of semiconductor nanowires, whereas gold nanodots also possess attractive applications in optoelectronic devices, photonics and plasmonics applications. This work was done at the CNM division of the Argonne National Labs, USA.

Further, study on the oxide based semiconductor nanowires (NWs) such as ZnO owing to its large excitonic binding energy and a potential candidate of optical devices is presented. Wide ranges of chemical and electrical properties of such metal oxides semiconductor nanomaterials makes them attractive candidate for variety of applications and also for basic research.

These metal oxides cover a diverse variety of electrical properties that ranges from wide band gap insulators, to metallic and further superconducting materials. In comparison with elemental semiconductors materials, growth behavior for oxide based semiconductor NWs is still not very well understood. We present a detailed study of the optimized growth conditions of ZnO NWs via carbothermal reduction process. We also present formation of complex nanostructures by changing growth profiles that results in increased build in polarization and a unique method is proposed to estimate the electric field profiles of ZnO nanostructures using atomic force microscopy. Lastly doping and band gap engineering of ZnO nanowires using vapor liquid solid (VLS) technique by alloying it with indium oxide is done and enhanced optical properties due to indium incorporation is reported. Further indium doped zinc oxide nanowires is presented to be a potential candidate for transparent conducting oxide material owing to its high transmittance and thus comprising an important element for optoelectronic and display applications.

1. INTRODUCTION

1.1. Nanotechnology: A Disruptive Technology

The influential talk presented by Richard Feynman in 1959 stating '*there is plenty of room at the bottom'* opened up a new field of physics [1]. It is widely stated by many knowledgeable people that this talk laid the foundation of '*nanotech*' [2-3]. In the 1970s, the term nanotechnology was developed further and new discoveries and remarkable progresses in the "*nanoworld*" followed – that often resulted in a Nobel Prize for the respective scientists [4]. Photonics in this respect is gaining significant momentum in the field of nanotechnology for its vast range of applications in sensing [5-6], spectroscopy [7], detectors [8-9], electro-optic devices such as modulators [10], switches [11-12], plasmonics [13], labs-on-a-chip [14], nonlinear devices and systems for quantum computing [15]. Ongoing device scaling for integrated circuit industry in this scenario is the utmost factor for survival of economy. However, the problem has started to occur in terms of reaching the limits in reduction of device dimensions. These concerns aggressively initiate the development and investigations of new technological concepts, materials and devices. No matter what is the application, a detailed study of these photonics based devices has revealed a rich physics within them which is discussed heavily in this thesis.

1.2. CdTe based photodetectors

CdTe is an important semiconductor material that belongs to II-VI class of compound crystals having a band gap of ~1.45 eV at room temperature [16]. This

material can be used for variety of applications that includes infrared (IR) optical windows and lenses, IR detectors, detection of *X*-rays, *γ*-rays and most importantly in photovoltaics applications [17-19]. CdTe semiconductor material when used as an infrared optical window has proved to show significantly better performance over a wide temperature ranges [20]. It can operate at room temperature that makes it a suitable candidate for allowing construction of compact detectors that can be used for applications specifically in nuclear spectroscopy [21]. CdTe when alloyed with mercury (Hg) makes *HgCdTe* detector that is also used to make a versatile IR detector [22]. CdTe can also be alloyed with zinc and the resulting *CdZnTe* compound can be used for excellent detection of gamma rays and solid state X-rays [23]. It can also be doped with chlorine and can be employed as radiation detector like x-rays and gamma rays as well as for alpha and beta particles and also can be used in photovoltaics applications [24]. Some of the versatile properties that makes CdTe such a superior semiconductor in detecting high performance radiations includes its larger band gap, large atomic. no.s such as Cadmium *Z:*48 and Tellurium *Z*:52 and high electron mobility resulting in excellent charge collection and high spectral resolution [25]. These materials also possess applications in electro optic modulators due to their higher electro optic coefficient amongst other II-VI based compound [26].

Another important application of CdTe semiconductor is in photovoltaics where this material is usually sandwiched with cadmium sulphide (CdS) compound to form a pn junction [27]. This PV cell is based on thin films structure of CdTe and CdS in order to absorb sunlight into electricity. CdS is an important semiconductor material with a direct band gap of 2.4 eV at room temperature that has been extensively used for variety of

applications such as solar cells [28-30], LEDs [31], displays [32-33], waveguides [34], inverters sensors [35-37] and optoelectronic devices [38-39]. Several deposition techniques have been tried in the past in order to grow CdS thin films such as chemical vapor deposition [40], pulsed laser evaporation [41] and sputtering [42] but there has been very limited studies on the growth of CdS thin films using thermal evaporation (TE) techniques. We developed a method to grow CdS thin films using TE technique and enhance film quality using low cost method. Further properties of polycrystalline CdTe based cells is investigated that represents the lowest cost cells that are growing rapidly in acceptance and represent the second most utilized solar cell material in the world due to its near optimum bandgap, high absorption coefficient and lower manufacturing costs [30]. In the past decade, there has been tremendous amount of work done for fabricating potentially economical CdTe/CdS based devices yet reported efficiencies are still lower than theoretically achievable limits [43-44]. Several efforts have been made to improve the device performance and in understanding the charge transport mechanisms of these nanostructured devices yet the role played by grain boundaries associated with polycrystalline nature of CdTe thin film and activation of cells is not completely understood until now. If we consider Hg based CdTe structures (*HgCdTe* detectors) for infrared (IR) detection, or CdTe/CdS based photovoltaic cells, an important limiting factor for device performance is recombination and noise limitations [45]. Thus knowledge about transport properties, defect states and phonon vibration states for polycrystalline CdTe thin films is of immense consideration in order to fabricate and optimize the nanostructures for attaining higher quality films that can be employed for variety of applications. We have tried to develop a method to understand and optimize

the structural, vibrational and energy transitions of CdTe thin films as well as CdS window layer that can be applied for applications in optoelectronic devices and can also help achieve higher efficiencies in CdTe based thin films solar cells [9]. Problems and efforts in order to improve the properties of CdTe thin films are also illustrated in this thesis.

1.3. History and modern use of metallic nanoparticles

Although metal nanoparticles have been in use for a long time; the properties of metallic nanoparticles were not explored until mid-19th century when Faraday first examined and described interesting properties of these nanoparticles [46]. He was very fascinated by the colors of metal nanoparticles and was able to produce successfully a colloidal solution of gold nanoparticles by reducing Nobel metal salt with phosphorous. However, he was unable to explain the color of the suspension and the variations in colors happening due to variations in size of particles. Some decades later, Zsigmondy continued this work initiated by Faraday on metal nanoparticles and developed an ultra-microscope where he could examine a single gold nanoparticle and verified its nanoscale dimensions while working together with Henry Siedentopf [47]. After this pioneer work by Faraday and Zsigmondy, variety of different methods have been developed in the past decade to produce metallic nanoparticles and very well defined nanostructures have been created. Such advancements in developing nanoparticles enabled fabrication of nano patterns with tunable size, shape and pitch with various optical properties [48].

Such metallic nanoparticles have potential applications in various fields such as nanoplasmonic sensing devices [49], biomedical sciences [50], photovoltaics [51] etc. The sensitivity of these devices can significantly improve if metallic nanoparticles are

fabricated with high uniformity, size tuning capability and stability. Although there has been advancements in this area but still production at large scale of highly defined metallic nanoparticles with lower cost and higher throughput fabrication techniques needs improvement. Top down lithography method such as e-beam evaporation technique can produce metallic nanoparticles with good control but this technique is very expensive and thus causes some limitation in high production volumes [52]. Thus interest in developing bottom up techniques in order to serve as an attractive alternative to top down approach has grown dramatically [53]. In this scenario, self-assembled materials particularly those with a length scale smaller than conventional manufacturing limits are going to occupy an important position in industry for a long time. Polymers in this context are likely to play a major role for their ease of processing and synthesis, low cost, variability of physical and chemical properties and most importantly their intrinsic nanoscale dimensions [54]. Among various techniques to fabricate gold nanoparticles, block co polymers have found significant attention due to its peculiar mesophase segregation and ease of processing [55]. We have employed block co polymer (BCP) lithography to fabricate gold nanoparticles of ~ 20nm sized using the self-assembly properties of BCP allowing a simpler yet very attractive route for controlling size, shape ad spacing of metallic nanostructures with ease and flexibility.

1.4. Block co polymer nanolithography

Block co polymers belong to a particular class of polymers also called ‘soft materials’ consisting of two or more chemically bonded homopolymer fragments blocks joined with each other by strong covalent bonding [56]. Considering simplest scenario with two different monomers, blocks named *A* and *B* could form diblocks of linear (*A*-*B*),

triblock (*A-B-A),* star or multi block copolymers [57]. The interactions between these chemically distinct blocks drive them to phase separate into different structures. By changing the lengths of each block, solution environment, chemical chemistry of monomers and the chain architectures such as linear or multi blocks, self-assembly can be manipulated [58].

Depending on the monomer type, polymers can be classified as either homopolymer or copolymers. When all the monomer chains are similar, the resulting molecule is known as 'homopolymer', whereas when more than one type of monomer is present, it is called a 'copolymer'. Different types of copolymer arrangements exist such as random copolymer, block copolymer, alternating copolymer or graft copolymer [59]. Phase separation and morphology of the diblock co polymer chains depends on various parameters such as temperature dependent Flory- Huggin interaction parameter (χ), degree of polymerization and volume fraction of one block (A) with respect to another (B) [60]. A-B incompatibility will drive a phase separation and covalent bond between the two blocks prevents bulk phase separation resulting in assembly of nanoscale domains with a morphology depending on the ratios of one block length with respect to another. Most common observed morphologies are hexagonally packed cylinders, cubic spheres, lamellae etc [61].

In the case of thin films, along with the composition of blocks and polymer-polymer interactions, the domain structure depends on surface interactions of the film introduced by confinement effects and surface energies [62]. Balanced interfacial interactions between the polymer blocks with the substrate and the free-space interface are essential in order to controllably obtain the required morphology. Further improved

ordering of BCP can be imparted using solvent annealing, chemical prepatterning, thermal gradients, shear, electric fields, or graphoepitaxy in order to obtain orientational as well as translational ordering [63]. We have taken advantage of BCP self-assembly characteristics and used it as a structure director for obtaining a nanoporous template for fabrication of Au nanoparticles. Cylindrical block copolymer films when oriented perpendicular to the substrate can provide a straight forward route to produce a nanoporus template after removing the cylindrical domains by chemical etching or UV degradation. Because the self-assembly of BCP occur in parallel, this technique provides a very low cost and fast route to obtain ultra high pore densities.

One key application arena for this class of materials is photovoltaics. For such applications, BCPs can be used either as structural directors or as an active layer or a combination of both [64-66]. Also these arrays can be used as templates for the vapor-liquid-solid (VLS) growth of materials for their potential applications in optoelectronic devices. The purpose of the present work is to obtain inexpensively and efficiently uniform nanostructures of gold particles and utilize these templates to pattern other devices and materials that can be beneficial in solar energy conversion devices as well as other applications. Figure 1 schematically conceptualizes the formation of gold nanodots using block copolymer lithography. Since substantial effort has been directed toward fabrication of vertically-aligned nanowires having highly controlled length, diameter and placement, gold nanoparticles fabricated using BCP nanolithography can serve as catalysts for the initialization of VLS growth of highly ordered and periodic structures of semiconductor nanowires arrays.

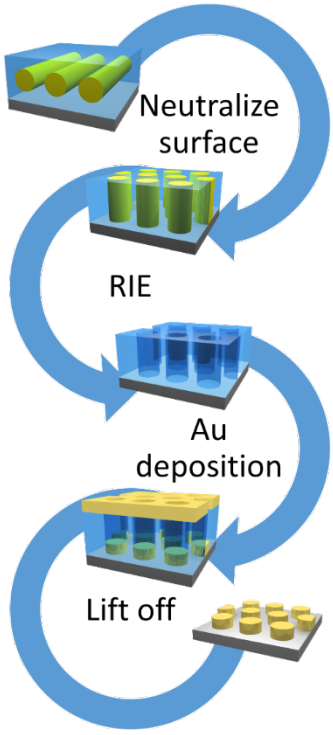

Figure 1: Schematic illustration of formation of gold nanoparticles utilized in this work

1.5. Semiconductor nanowires

One dimensional (1-D) semiconductor nanowires have gained a great interest in the field of nanotechnology and for technological applications [67]. It is well know that dimensional and size reduction- (quantum confinement) of these one dimensional nanostructures cause significant impact on their optical, electrical and mechanical properties [68]. These nanowires are used in variety of application such as photodetectors [69], transistors [70], lasers [71], biosensors [72], gas sensors [73], optical switches [74] etc. Controlled nanowire synthesis reveals that materials with different sizes, structures and shapes, morphology and composition such as alloying or doping are able to be integrated. This property of integrating various variables and specific properties into one system can develop integrated circuits using bottom up assembly. This technique of assembling structures using bottom up method is a commonly used approach to grow

nanowires structures [75-76]. This approach is based on using a catalyst normally metal that enables the formation of complex 1-D device structures. Such a growth technique is normally achieved by commonly employed vapor liquid solid mechanism first introduced by Wagner and Ellis with the growth of *Si* whiskers [77]. This vapor liquid solid (VLS) growth technique is a highly controlled and flexible growth mechanism for the formation of complex nanodevices that can be used for various applications [78].

Zinc oxide (ZnO) belongs to II-VI class of compound semiconductor with a wide bandgap of ~3.37 eV and large excitonic binding energy at room temperature. It has received a lot of attention in the past decade due to its unique optical and electrical properties and wide applications [79]. It is very important to precisely control the dimensions of nanowire for some applications one of which is in photovoltaics [80]. In order to maintain efficient charge separation in nanowires based devices, wire dimensions should be thin and densely packed. A dense and every distributed array of ZnO nanowires will provide a direct route for the photo generated electrons to be collected at the electrodes and thus enhance device performance. We have employed VLS growth method which is one of the most effect ways for nanowires synthesis and variations in size, position, shape and composition of wires. The morphology and density of as-deposited nanowires can be determined by factors like temperature, gas flow, substrate, catalyst, reaction times etc [81]. We have investigated the luminescence and structural properties of different grown ZnO nanostructures and developed a unique way to calculate the magnitude of electric field for ZnO nanowire and nanostar from the electrostatic force analysis by measuring the amplitude change in the AFM probe due to its spontaneous polarization effects [82].

1.6. Doping in Zinc oxide

In order to manipulate and control the properties of semiconductors to obtain desired properties, intentional doping is achieved by incorporating specific atoms of interest. [83]. Doping also plays an important role in the field of nanotechnology and nanoscience by formation of doped nanostructures with exciting characteristics. ZnO when doped with transition metals has variety of applications in optoelectronics and has also been proved to be a diluted magnetic semiconductor after doping [84]. Also for formation of ZnO LED, we need both n type and p type ZnO in order to form a pn junction thus adding small amount of dopant in ZnO can change its behavior significantly. ZnO has a band gap of 3.37 eV at room temperature. In order to shrink its band gap or expand its band gap, we need to do band gap engineering. We can shrink the band gap and push it into visible region or can expand its band gap by alloying it with elements based on specific applications [85]. Here in this thesis, Farid *et al.* [86] demonstrate an approach to dope zinc oxide nanowires with indium oxide by employing VLS growth method. Shape evolution from ultra-thin nanowires to nanowires with wider diameter and nanobelts are also discussed. Defect state analysis is done using detailed low temperature photoluminescence measurements which have been rarely explored until now. We have reported enhanced optical properties due to indium incorporation in zinc oxide nanowires. Alloying with indium oxide is done in order to tune the band gap of zinc oxide and their changed optical properties are also investigated.

1.7. Structure of this thesis

Chapter 2 discusses characterization of CdS layer required for the growth of CdS/CdTe based detectors. CdS films on ITO coated glass substrates is fabricated using

thermal evaporation techniques and effects of annealing and excitation dependent input of CdS thin films using Raman and photoluminescence spectroscopy is explored [30]. Chapter 3 represents my published manuscript [9] that discusses temperature dependent photoluminescence (PL) measurements on chloride treated polycrystalline cadmium telluride (CdTe) thin films grown by e-beam evaporation technique. Also effects of cadmium chloride treatment on morphology and device optimization are discussed and the defect states analysis is presented. In chapter 4, we fabricated high density arrays of uniform gold nanodots and nanopores using block co polymer nanolithography technique. Chapter 5 discusses growth mechanism of ZnO nanowires and optimal reaction conditions for the growth of ZnO NWs via VLS growth mechanism are presented. Complex nanostructures formation due to change in experimental growth condition is presented and analysis on the complex nanostructure formation and diameter dependent optical characterization is discussed [82]. Chapter 6 shows doping in zinc oxide nanowires with indium oxide using VLS growth mechanism that is reproduced from my published article [86]. Band gap engineering by varying indium content is presented and its potential application as a candidate of transparent conductive oxide is evaluated. Lastly chapter 7 shows conclusions and future work.

2. MULTIPHONON RAMAN SCATTERING AND PHOTOLUMINISCENCE STUDIES OF AS-GROWN AND ANNEALED CADMIUM SUPLHIDE NANOCRYSTALS

We have already provided a brief background on the applications and importance of fabricating low cost CdS thin films for various applications in optoelectronic devices in Chapter 1. In this chapter, we discuss successful growth of high quality CdS films on ITO coated glass substrates by thermal evaporation techniques and presented analysis on the effects of annealing and excitation dependent input of CdS thin films using Raman and photoluminescence spectroscopy. Our results reveal Raman surface optical phonon modes at 303 cm^{-1} and 606 cm^{-1} for the as grown films while annealed films shows a dramatic increase in Raman intensity along with clear indication of four overtones. LO phonon modes have been analyzed quantitatively considering the contributions due to anneal induced effects on film quality using phonon spatial correlation model, line shapes and defects to the line broadening. Slight asymmetry in the Raman line shape towards the low frequency side is related to the phonon confinement effects and is modeled by the spatial correlation model. Calculations of width (FWHM), integrated intensity, and line shape for the longitudinal (LO) optical phonon modes indicate improved crystalline quality for the annealed films as compared to the as grown films. With increase in laser power, intensity ratio of 2-LO to 1-LO optical phonon modes is found to increase while multiple overtones upto fourth order are observed. Power dependent photoluminescence data indicates direct band-to-band transition in CdS thin films.

2.1. Purpose of annealing CdS thin films

Improving film quality and crystalline properties is an important subject for device applications that can lead to enhanced device performances. One of the issues reported with growing CdS by thermal evaporation (TE) technique is detoriation of film crystallinity due to low substrate temperatures employed in deposition and researchers have reported significantly lower Raman peaks as compared to other deposition techniques such as pulsed laser evaporation [89-90]. Annealing can give rise to changes in nano crystal sizes and phase that can significantly alter the device performance [91]. We have grown CdS thin films using TE technique and later underwent CdS thin films into post annealing treatment. We have successfully reported multiphonon Raman scattering in post annealed CdS nanocrystals grown by thermal evaporation techniques and presented a comprehensive study on the width, line shape and intensity of longitudinal (LO) optical phonons modes in Raman spectra using spatial correlation model. In section 2.3, we have compared as grown and post annealed CdS films and presented anneal induce effects on the crystal quality using Raman and PL spectroscopy. One can probe anneal induced vibrational and structural changes by Raman spectroscopy. On the other hand excitation dependent structural changes can affect electron phonon interactions [92]. By varying excitation conditions, annealing temperatures and duration, the particles sizes and band gap can be varied and controlled [93-94].

2.2. Experimental

A 200 nm thick CdS layer is obtained using thermal evaporation (TE) techniques on ITO coated glass substrate at room temperature keeping the base vacuum pressure at ~ 10^{-7} Torr range. CdS evaporation source in this work was purchased from Cerac, Inc

(99.999% source). CdS samples were annealed for 30 min in air ambient at room temperature for 30 min in air ambient at room temperature for 450 ^{o}C. Optical characterization of the as grown and annealed films have been carried out using photoluminescence (PL) and Raman spectroscopy. PL setup used in this work consist of Acton SpectraPro 2500i spectrometer with three grating imaging monochromatic. Grating used was 1200 g/mm and the experiment was carried out with a back scattered geometry. PL spectra was taken at room temperature in the 45" reflection geometry with the samples placed on the micrometer stage of the single grating spectrograph. PL emission was excited using CW He-Cd laser source from KIMMON Koha Co., Ltd., with wavelength of 441.6 nm. Room temperature Raman scattering experiment was performed using a Raman Reinshaw 2000 microscope system with a 1800 g/mm grating and an excitation source of 514 nm wavelength with input power varied from 6-24 mW.

2.3. Results and Discussions

2.3.1. Optical Phonon Modes investigation using Raman Spectra

Room temperature Raman spectra for the CdS thin films grown by thermal evaporation technique using 514 nm laser line excitation is shown in figure 2.

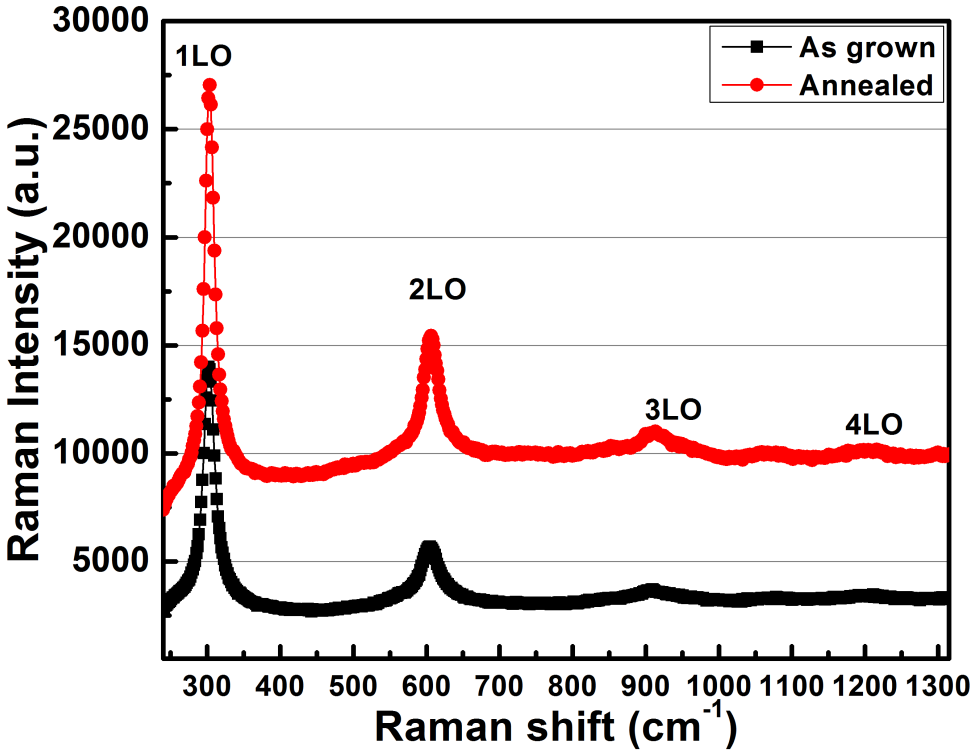

Figure 2: Room temperature Raman spectra of the as grown and annealed films excited using 514 nm laser.

For the as grown films, we observe two dominant peaks showing the 1-longitudinal optical (LO) phonon mode at 303 cm^{-1} and 2-LO mode at 606 cm^{-1}. There is almost negligible indication of multiple over tones while the line width (FWHM) for 1-LO phonon mode is found to be ~17cm^{-1}. For single CdS crystal, 1-LO phonon mode is reported to be at 305cm^{-1} while fwhm is ~12cm^{-1} [95]. Observed shift in low frequency side and broadening in line shape as indicated in fig. 4 can be attributed to the confinement of optical phonons in CdS nanocrystals since CdS exhibits strong size dependent optical and electrical properties [96]. In the case of a perfect crystal, phonon Eigen state is a plane wave and only the optical phonons at the zone center ($q=0$), where q is the wave vector, contribute to the first order Raman scattering process. For

nanocrystals, this *q=0* selection rule is relaxed due to the phonon confinement within the nanocrystals which allows a range of *q* vectors away from the center in the Brillouin zone to also contribute to the resultant Raman line. As a result, Raman line shape exhibits a change depending on the phonon dispersion curve $\omega(q)$. CdS dispersion curve exhibits a negative slope at *q=0* hence contributions from higher *q*'s result in asymmetry of the line shape towards the low frequency regime of the LO phonon mode which we observe in our study [97].

2.3.2. Spatial Correlation Model

In order to calculate the phonon line shape, spatial correlation model (SCM) proposed by Campbell and Fauchet is used [98]. This model has been extensively used to understand the Raman line shape of crystals with various sizes [99-100]. According to this model, Raman intensity for a nano crystal of diameter *d* can be expressed as

$$I(\omega,d) = \int \frac{|C(q,d)|^2 \, d^3q}{[\omega - \omega(q)^2] + \Gamma o/2)^2} \tag{1}$$

Where Γo is the intrinsic phonon line width and *q* is usually expressed in units of $2\pi/a$ where *a* is the lattice constant for CdS. $|C(q,d)|$ is the Fourier transform of the confinement function which is given by

$$C(q,d) = \exp \frac{-q^2 d^2}{2\alpha} \tag{2}$$

Many studies have satisfied the Gaussian confinement model using values of α as $8\pi^2$ so we will be using this value for our calculations [101]. Using this expression, equation (1) can be expressed as

$$I(\omega,d)=\int\frac{\exp\frac{-q^2d^2}{2\alpha}d^3q}{[\omega-\omega(q)^2]+\Gamma o/2)^2} \quad (3)$$

To evaluate (3), phonon dispersion curve expression for LO phonon is fitted from the calculations by S. Sahoo *et al.* [101]. Assuming a spherical particle size, line width calculated from SCM is ~14cm^{-1} which is fitted well for a particle size of ~ 45-55 A^{o} as shown in figure 3.

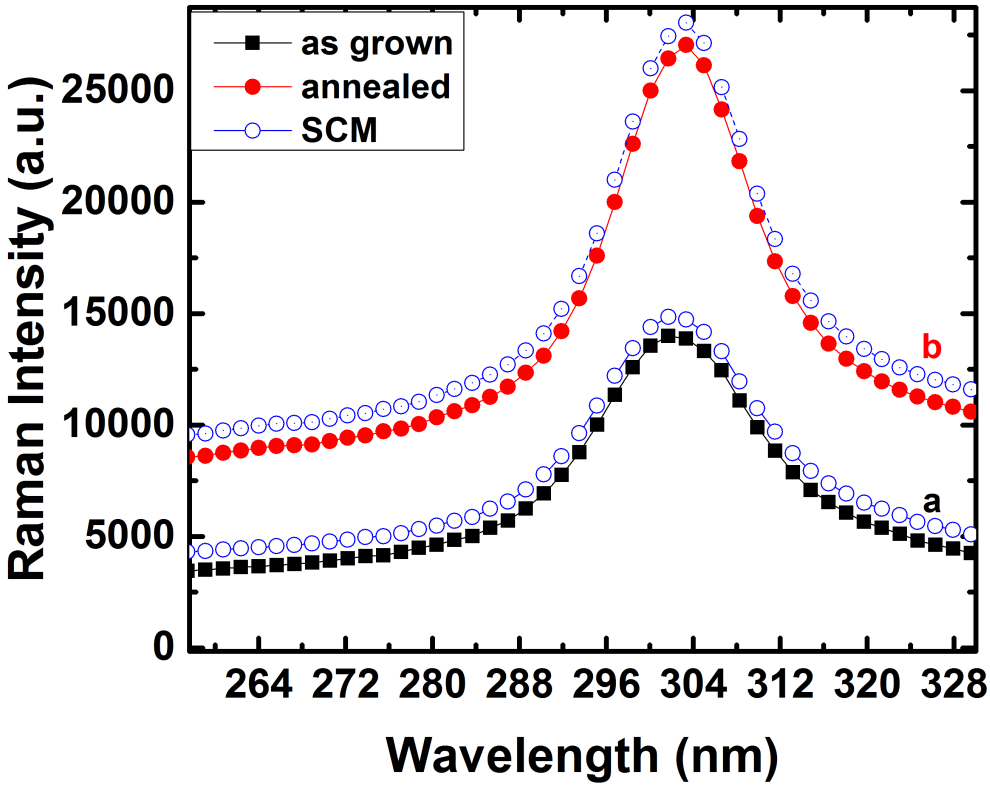

Figure 3: 1-LO phonon mode peak fitting using SCM for the a) as grown and b) annealed.

Raman spectra for the films annealed at higher temperatures (450^{o}C) for 30 min in air ambient is also shown in figure 4. We observe a dramatical increase in Raman intensities with much clear indication of multiple overtones (3-LO & 4-LO) which are not significantly observed for the as grown samples. Peak positions seems to be

unchanged but the FWHM appear to reduce for annealed samples (15.7 cm^{-1}). R. Prabhu *et al.* [102] reported that in case of nanoparticles, surface layers occupy a significant volume of the material and atomic arrangement at the surface or the grain boundaries are away from its equilibrium. If the heat treatment causes a more regular arrangements of atoms in the surface layers, it results in reduction of the width of Raman signals and also a reduction in the defect density which results in significant improvement of Raman signals and improved crystalline quality. Later in this chapter, we present photoluminescence data to understand the defect states in CdS films. However calculations for the integrated intensity ratio of 2-LO to 1-LO phonon modes has been done.

It is well known that the degree of electron-phonon coupling at a particular wavelength can be quantified by calculating the ratio of integrated overtone intensity to that of the fundamental, thus the ratio I_{2LO}/ I_{1LO} is an important tool in order to measure the disorder in the film [103]. Some studies have shown that the ratio of 2-LO to 1-LO phonon increases with the increase in particle size [104]. However this ratio can vary upon variations in different incident wavelengths. For our case, it is found that the ratio increased from 0.4 for the as grown films to 0.53 for annealed samples showing an improvement in crystalline quality for the annealed films as compared to as grown films.

2.3.3. Photoluminescence spectra

For further characterization of the CdS film, room temperature photoluminescence (PL) measurements are performed for the annealed samples and for the as grown films recorded at an excitation wavelength of 441.6 nm using He-Cd laser. Figure 4 shows the PL spectra from CdS layer grown by TE and after annealing at a

temperature of 450 ^{o}C. We observe a broad green luminescence peak at ~2.42eV (514nm).

The intensity of green band emission was found to increase enormously when the films were subject to annealing as compared to the as grown samples. This green band peak is found to be asymmetric as well as relatively of wide broadness and is fitted further with two Lorentzian fits shown in figure 6 (dotted lines). Band gap for the CdS single hexagonal crystal is at ~500 nm (2.48eV) [105]. Studies shows that CdS films might get sulfur deficiencies as sulfur is found to be more volatile than Cd and annealing at higher temperatures causes sulfur to dislocate from CdS which may result in asymmetry of the luminescence band [92].

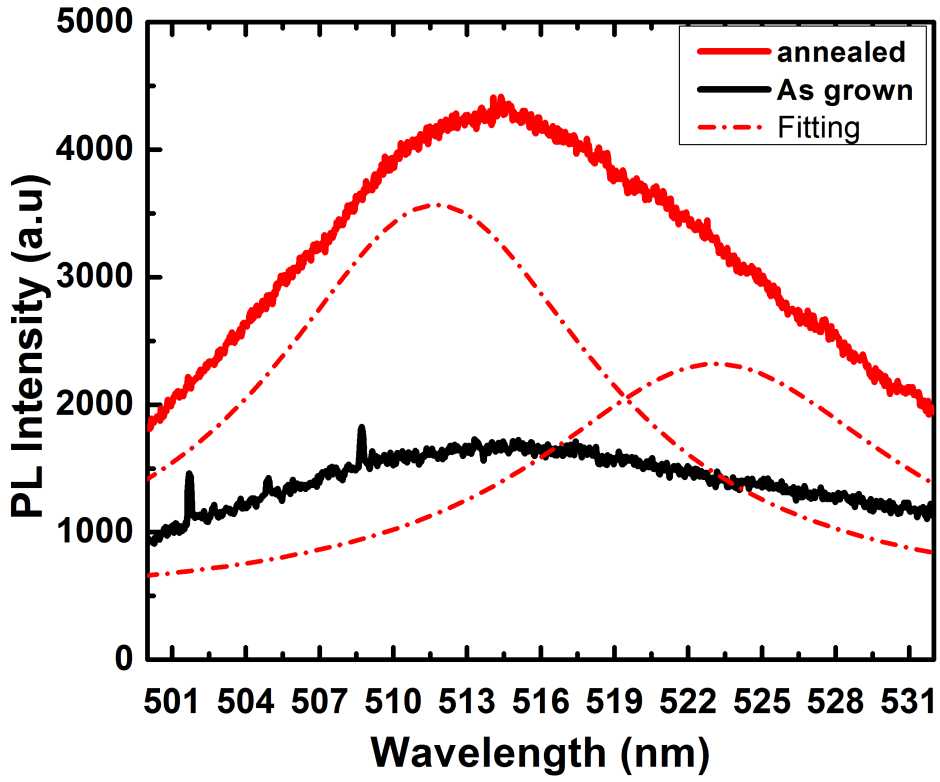

Figure 4: Photoluminescence spectra for the as grown (solid line, lower spectra) and annealed CdS films (solid line, top spectra) at 441.6 nm laser line excitation while Lorentzian modes for annealed films are shown by dotted lines.

2.3.4. Excitation dependence of the Raman and Luminescence Signals

In order to analyze the effects of CdS thin films on the excitation input conditions, Raman and photoluminescence measurements are carried out as a function of input excitation power. Excitation input is varied from 6 mW to 24 mW for the as grown CdS films. Figure 5 indicates the Raman spectra of the CdS thin films at laser power of 6 mW, 12mW and 24 mW using emission line of 514 nm.

As shown in figure 5, it is observed that for all input excitations Raman data indicates two dominant peaks indicating the longitudinal optical (LO) phonon mode at approximately 303 cm^{-1} (1LO) and its overtone (2LO) at about 606 cm^{-1} with a linear increase in integrated intensity on increasing input power. It is noticeable that negligible 3-LO and 4-LO phonon modes are visible for the samples excited at low excitation power but the multiple overtones effects become more visible after increasing the excitation power to enhanced power levels (~24mW). Calculation of integrated intensity ratio of 2-LO to 1-LO phonon mode from our experimental data shows 0.38 for 6mW, 0.4 for 12mW to 0.43 for 24mW with input excitation power variations.

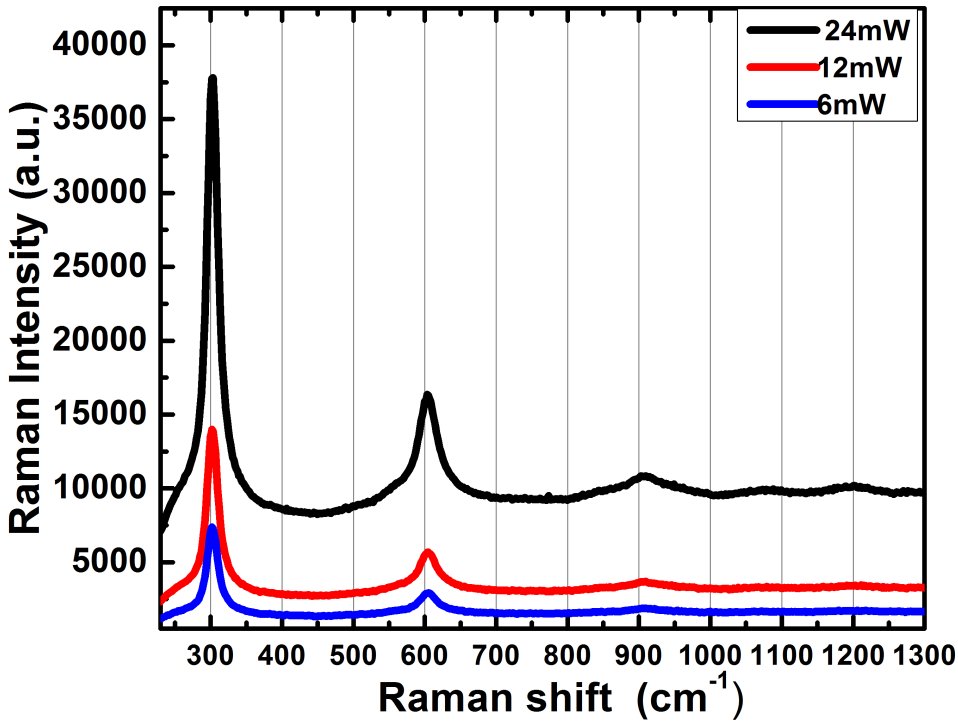

Figure 5: Raman spectra at varied excitation power (decreasing power from top to bottom curve).

To understand more on the effects of electron phonon interactions and underlying recombination processes, transmission laser power dependence photoluminescence spectra is obtained as shown in figure 6(a) using different neutral density filters (Thorlabs). We observe a slight shift in energy from 2.43eV (510.2nm) to ~2.412 eV (514nm) with the increase in photo excitation powers. Also it is noticed that the the plot of PL integrated intensity with respect to excitation input variations shows near linear behavior with a positive slope indicating that the recombination was mainly band to band as indicated in figure 6(b).

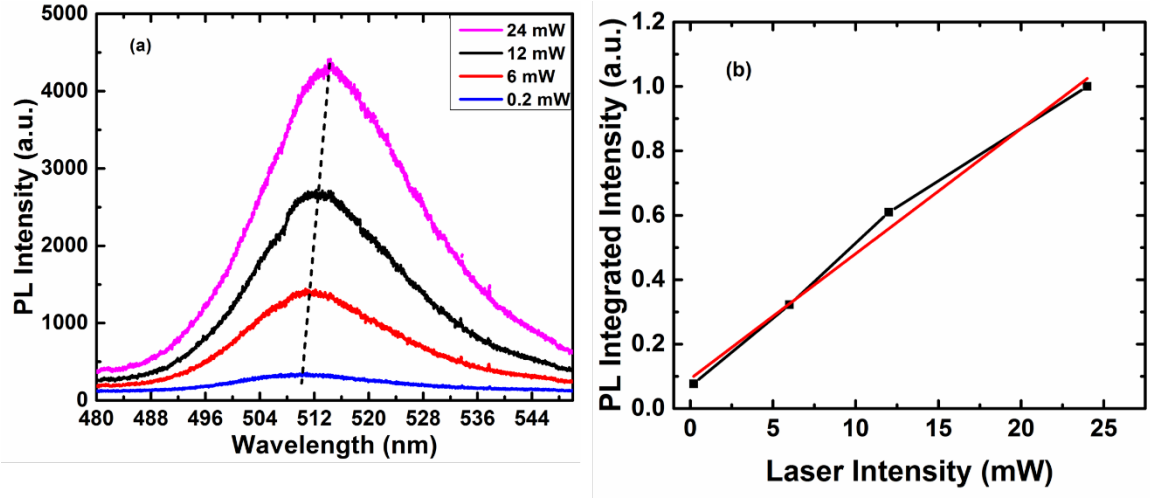

Figure 6: (a) PL spectra of CdS as grown films excited at varied laser power (decreasing power from top to bottom curve) using neutral density filters; (b) Variation of laser power on the photo luminescence integrated intensity area of dominant PL peak (straight line indicated linear fit)

2.4. Conclusions

We have characterized as deposited and annealed CdS thin films grown by thermal evaporation technique and reported multiple phonon Raman peaks upto fourth order for the annealed CdS nanocrystals. Asymmetry in the line shape of LO phonon modes is attributed to the phonon confinement effects and fitted well with the spatial correlation model. Improved crystalline quality is achieved for annealed CdS films as compared to as-grown samples and knowledge of line widths and integrated intensities ratio of 2-LO to 1-LO phonon modes is revealed. Asymmetry and wide broadness indicated from photoluminescence green emission peak around 2.42 eV is attributed to the sulphur deficiencies in CdS films. Excitation dependent photoluminescence and Raman spectra shows band to band transition and improved CdS film quality is reported.

3. ANALYSIS ON THE STRUCTURAL, VIBRATIONAL AND DEFECT STATES OF CHLORINE TREATED CADMIUM TELLURIDE STRUCTURES

In this chapter, temperature dependent photoluminescence (PL) measurements are performed in order to study the defect states in cadmium chloride treated polycrystalline cadmium telluride (CdTe) thin films grown by e-beam evaporation technique. Three luminescence bands are observed including a double peak emission at 1.577 eV and 1.573 eV corresponding to free electron to acceptor transition and a donor acceptor pair transition respectively along with a broad peak at 1.45 eV. This broad band emission is related to A-center chlorine based complex and also includes longitudinal (LO) phonon emission lines for CdTe spaced by ~21meV. Investigation into grain sizes revealed grains of 0.2 μm for as grown films and ~2-3 μm for chlorine activated films shown by atomic force microscopy (AFM). Raman analysis indicate that the films have been grown with excess of Te leading to p- type conductivity in the structure whereas LO phonon mode of polycrystalline CdTe reveals quasi phonon modes nature. This work is reproduced from my published article as mentioned in ref [9].

3.1. Advantage of using e-beam evaporation for CdTe deposition

So far several deposition techniques have been tried to grow CdTe thin films such as close-spaced sublimation (CSS) [106], chemical bath deposition (CBD) [107], vacuum evaporation [108], spray pyrolysis [109], sputtering [110] and electrodeposition [111]. A feasible alternative to these processes which has not been paid sufficient attention to is the electron beam evaporation (EBE) technique in order to deposit the CdTe thin films.

As compared to the traditional chemical methods, physical methods tends to appear more promising candidate for growing active layer [112]. Specifically physical vapor deposition method such as e-beam evaporation poses several advantages as compared to other traditional deposition approaches such as excellent film purity due to high vacuum condition, higher deposition rates, less surface damage of the substrate due to impinging atoms while film deposition, less tendency for unintentional heating of substrate, low cost, and environmental friendliness [113]. We have successfully prepared CdTe films using EBE technique and investigated film quality using optical characterization techniques in order to enhance device performance for its potential applications in solar cell technology.

3.2. Challenges with polycrystalline CdTe thin films

Polycrystalline CdTe materials with grains limits the recombination velocity and life times of carriers that affects the device performances. $CdCl_2$ post activation treatment which is a necessary and critical step in the complicated procedure of fabricating CdTe/CdS thin films solar cell is believed to enhance the p- type doping in CdTe layer [114] and is also associated with recrystallization [115], grain growth [116], reduction in stress and the defect density, which ultimately raises the efficiency. Therefore knowledge about the defect states of these chlorine activated CdTe films is very important for solar cell applications. Due to the polycrystalline nature of CdTe films, these defect states exhibit slightly different nature of transitions compared to single crystalline CdTe layers [117]. Many studies have been done analyzing single crystalline CdTe structures but very little attention is emphasized on understanding the defect states and crystal quality of polycrystalline CdTe cells that could potentially result in lower cost and higher efficiency

PV devices. In this work, low temperature photoluminescence measurements are performed for a detailed defect states analysis. Effects of $CdCl_2$ treatment on the grain sizes of polycrystalline CdTe layer is also presented that can help understand the crystal structure and optimize the device for applications in optoelectronic devices.

For CdTe/CdS based devices, another limitation to increase efficiency is the difference between the crystal structures of CdTe and CdS. It is important to obtain CdTe in hexagonal phase as the CdS is more stable in the hexagonal phase that could result in growing two layers with the same phase [118]. Also it has been established that tellurium excess in CdTe structure lead to p-type conductivity that plays the role of absorber layer for CdTe/CdS based solar cells [119]. Thus it is important to understand the vibrational states of these films to optimize device performance. The objective of this work is to identify and analyze the energy transitions which may result due to recombination caused by intrinsic defects and also due to chlorine activation process in polycrystalline CdTe films. Vibrational analysis using Raman spectroscopy is also performed which shows Te rich surface and quasi phonon modes of mixed symmetry is revealed.

3.3. Fabrication procedure

Samples used for characterization of CdTe thin films have been taken fabricated by the coauthor of our published work Hyeson Jung from University of Illinois at Chicago [9]. Polycrystalline CdTe thin films have been deposited by e-beam evaporation technique on CdS/SnO_2:F (FTO)/glass substrate structures. The cell was developed in a superstate configuration using vacuum deposition techniques followed by annealing treatments. For the deposition of CdS on the FTO, thermal evaporation technique was used keeping the base vacuum pressure at ~10^{-7} Torr range and substrate at room

temperature, growing approximately 200 nm thick CdS layer. CdS evaporation source (99.99%) was purchased from Cerac, Inc. CdS is followed by deposition of about 4 μm CdTe layer by e-beam evaporation at 300 ^{o}C at a higher vacuum pressure of 10^{-7} Torr using CdTe evaporation source (99.999%) purchased from Cerac Inc. Further CdTe films were annealed using cadmium chloride ($CdCl_2$) vapor process treatment utilized for activation of the cell junctions. The as-grown CdS/CdTe thin film was placed on the graphite plate, and the samples were baked at 425 ^{o}C for 20 minutes under continuous $CdCl_2$ vapor flow generated by a vaporizer. This technique was carried out under atmospheric pressure without the use of high purity gases or a vacuum system.

The analysis of the surface morphology of these cells was done by atomic force microscopy (AFM) technique using tapping-mode atomic force microscope (Nanoscope V, Veeco). The defect states for the $CdCl_2$ treated CdTe layers was studied using photoluminescence spectroscopy done at room temperature that consists of Acton SpectraPro 2500i spectrometer with three grating imaging monochromatic equipped using liquid nitrogen cooled charge coupled device. The grating used for current experiment was 600 g/mm with an excitation input of 633 nm. Low-temperature PL measurements were carried out using a closed-cycle Janis CCS-150, 10 K cryogenic system. The vibrational states of $CdCl_2$ treated and untreated films was studied using Raman spectroscopy excited by 633 nm (HeNe) laser line using a Reinshaw inVia Raman spectroscope at room temperature.

3.4. Results and Discussions

3.4.1. Low Temperature Photoluminescence Characterization

Low temperature PL spectra of chlorine treated polycrystalline CdTe films measured at 10K at a nominal power of 20 mW and 633 nm excitation input is shown in figure 9. Transitions can be seen at energies of a) 1.577 eV, b) 1.573 eV and c) at 1.45 eV (including LO phonon lines). The transition regions from 1.55 – 1.6 eV is also shown on wider energy scale in the inset of figure 9. Two distinct peaks seen between 1.55 – 1.6 eV energy range correspond well to the literature data [120-121]. The whole PL spectrum is also fitted with several Gauss peaks as shown in figure 7. Two closely packed peaks at 1.577 eV and 1.573 eV with energy separation of 4 meV are seen. Peak at 1.577 eV is associated with electron to acceptor (e, A0) transition while a donar-acceptor pair (DAP) transition is expected to happen at 1.573 eV [122]. Some authors report only a single peak between 1.55 eV to 1.57eV range which they assign to DAP transition related either to a cadmium vacancy or oxygen related DAP transition [123].

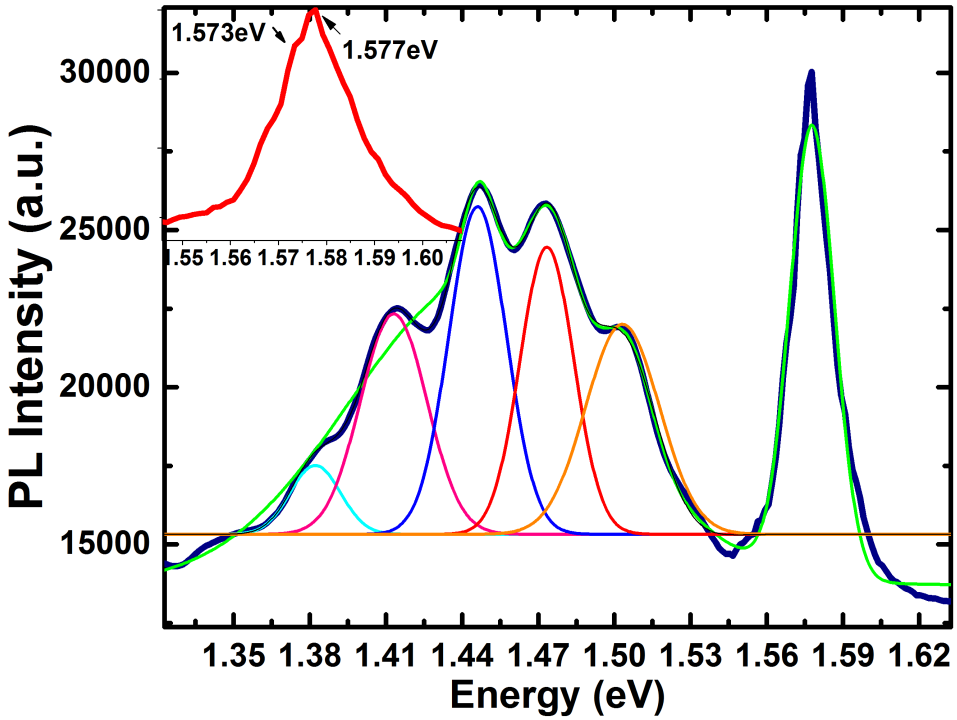

Figure 7: PL spectrum of the chlorine treated CdTe sample at 10 K including the Gauss profiles fit. The inset shows a magnification of the 1.55 – 1.56 emission range.

A broad defect band around 1.45 eV is observed in our study which is commonly associated with A- center often related to chlorine based acceptor complex. Such broad emission is usually associated with the polycrystalline nature of CdTe and not significantly observed in single crystal CdTe structure [124]. Since the area illuminated by the laser excitation beam is much larger as compared to grain sizes, many grains with different dislocation densities, sizes, defect concentrations and recombination sites makes it very hard to detect an individual homogenously broadened emission line. This broad defect band consists of several peaks with an energy separation of approximately 21 meV which is the optical longitudinal phonon line energy of CdTe films [122]. These several orders of LO- phonon lines shows a strong coupling of the respective defect to the lattice structure.

In order to analyze these grains in polycrystalline CdTe films, AFM was performed for the chlorine activated as well as untreated films as shown in figure 8. Our as-deposited CdTe films have average grain sizes of approximately 0.2 μm whereas chlorine activated films showed a larger grain size of around 2-3 μm.

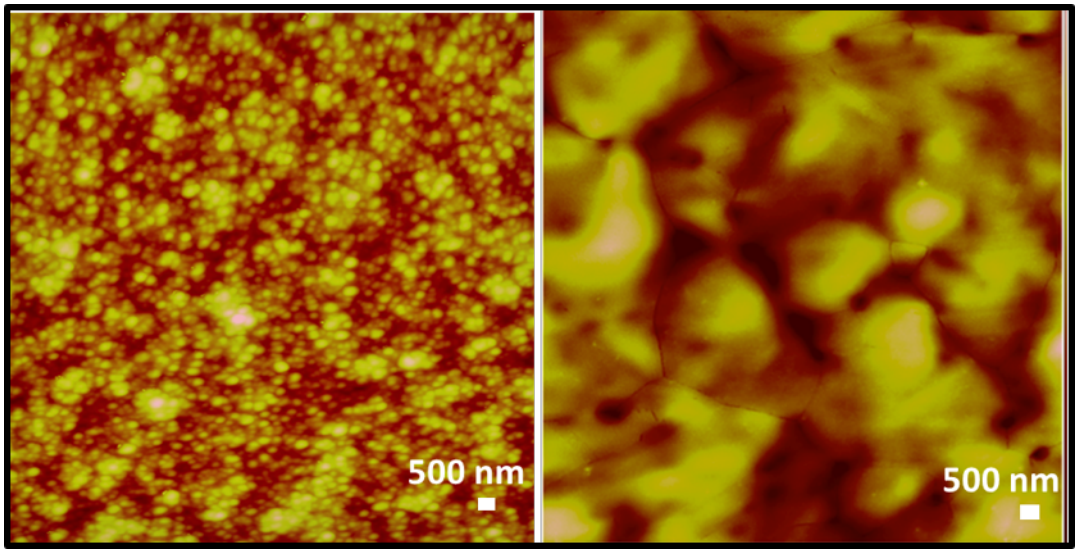

Figure 8: AFM measurements of a) CdTe without CdCl2 annealing treatment: grain size 0.2 μm b) CdTe with $CdCl_2$ annealing treatment: grain size 2-3 μm.

These enhancement in grain sizes due to annealing treatment is associated with the recrystallization process. Studies have shown that this low temperature annealing treatment is used to promote recrystallization, grain growth, and diffusion between the CdS and CdTe layers which enhances the p-type conductivity in the CdTe layer [125]. This enhancement in grain sizes facilitates the passivation of grain boundary traps and improves device performance [126]. Considering an average size of 3 μm for our chlorine treated samples, 20 μm spot size for laser excitation beam will lead to several grains under examination for the photoluminescence study resulting in broadened PL emission lines.

Temperature dependent photoluminescence spectra from 10K – 90K is shown in figure 9a. For the 1.45 eV peak, initial studies have shown that the origin of this band is associated with the recombination of the excitons with a localized center [124] but later it is revealed that this band is associated with the A center related peak [123]. As the

temperature is increased, quenching of the PL intensities of the luminescence signal is observed. When the temperature reaches to higher values, the free electrons thermalizes and phonon replicas becomes less distinct and merge into a single broader peak emission band. For the double emission peak at 1.57 eV, a decrease in 1.577 eV peak is observed on increasing the temperatures as compared to 1.573 eV emission. This temperature dependent behavior is assumed to be associated with the donar acceptor (DA) pair transition which switches to the transition of an electron from the conduction band to the energy state of an acceptor as the shallow donar thermalizes. This acceptor is known to be related to the cadmium vacancy V^{cd-} as found in previous studies [127-128].

It is possible to deduce the activation energy directly from the temperature dependent plot of the PL intensity. This temperature dependence of the luminescence intensity can be expressed according to well known Arrhenius equation as shown in eq 4 [9].

$$I(T) = \frac{I_0}{1 + A\exp(-\Delta E / K_b T)} \tag{4}$$

Where I_o is the emission intensity at 0 K (10 K for our case), K_b is the Boltzmann's constant and ΔE is the activation energy. A log plot of integrated intensity versus 1000/T is used to extrapolate the activation energy of the thermal quenching process as shown in figure 9b. From our experimental results, we obtain an activation energy of 49 meV for the 1.577 eV band whereas 100 meV for the 1.45 eV which is in good agreement with the values obtained by Kraft *et.al.* [123], Neu *et.al.* [129] and Krustok *et.al.* [130].

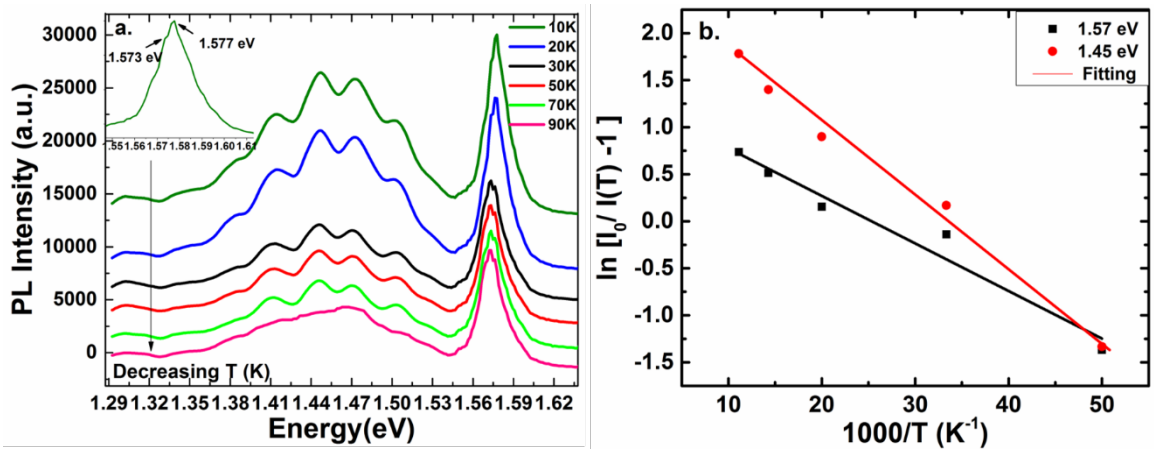

Figure: 9 a) Low temperature (10K - 90K decreasing order) photoluminescence spectra for the annealed CdTe films with at 633 nm laser line excitation. The inset shows a magnification of the 1.55 eV – 1.61 eV range. b) Temperature dependence of emission bands at 1.5577 eV and 1.45 eV for extrapolating activation energies.

3.4.2. Raman analysis on the CdTe films

In order to observe the phonon vibrational states of the CdTe films, Raman spectrum of the as grown as well as $CdCl_2$ treated polycrystalline CdTe films excited with 633 nm laser is done as shown in figure 10. We observe three clearly distinguishable bands at 118.9 cm^{-1}, 136.5 cm^{-1} and 166 cm^{-1} for both CdTe samples. Sharp band at 118.9 cm^{-1} is associated with contribution from Te rich surface and is assigned as A1 mode corresponding to the phonons vibrations in the hexagonal Te structure [123]. This A1 band seem to reduce significantly for as- grown samples since these films consists of several smaller sized grains as compared to chlorine treated films that has larger grains which can also contribute to improved Raman signal and better film quality. The TO mode (Te) is seen at 136.5 cm^{-1} and the LO mode (Cd-Te) is observed at 166 cm^{-1}. Appearance of LO phonon mode at 166.3 cm^{-1} is observed by other researchers on a

polycrystalline CdTe structure fabricated on CdS/ ITO/ glass substrate which indicates composites of hexagonal and cubic CdTe structures according to their respective phonon dispersion curves [131][118]. Our key observation is that the Raman mode frequency observed for the CdTe thin films is different from either mode of the single crystal. This can be interpreted as the quasi phonon modes nature of the polycrystalline CdTe films.

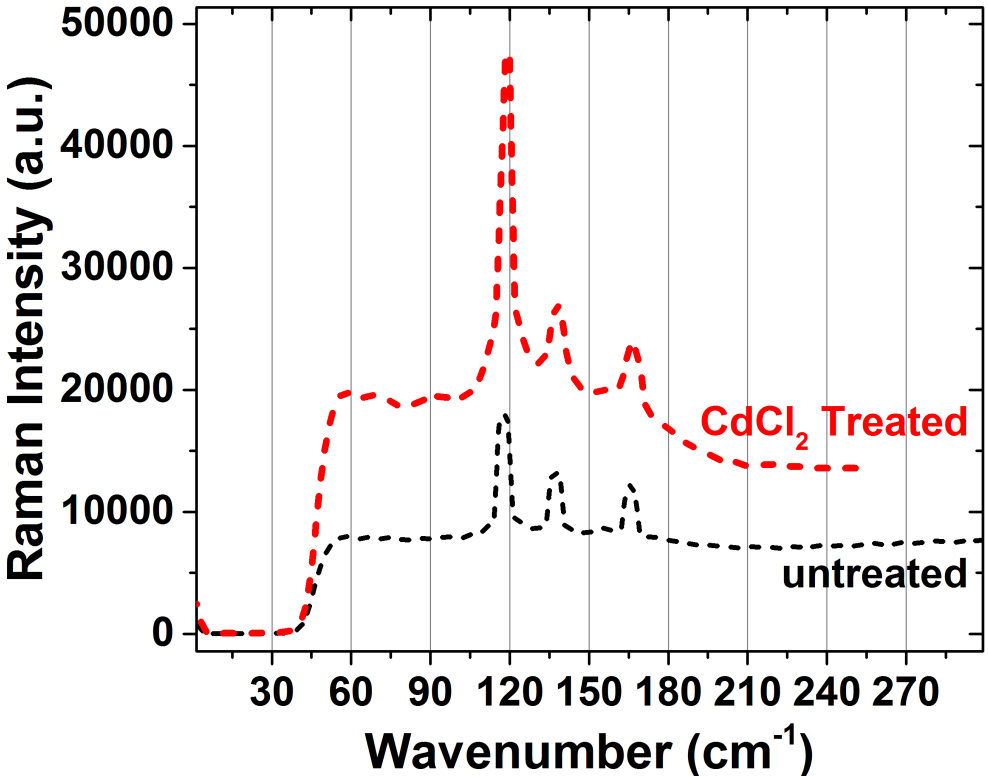

Figure 10: Raman spectrum of polycrystalline CdTe thin films excited using 633 nm laser line.

3.4.3. Quasi Phonon Modes

According to the Raman selection rules, Raman modes observed in a spectrum depends not only on the polarization of incoming and outgoing light but also depends on the crystal orientation relative to light propagation. This cause the Raman modes to be visible at a particular geometry. Raman scattering from the crystal axis which are not the *a* or *c* symmetry axis results in quasi phonon modes nature of the crystallites [132].

According to Loudon's model, these quasi modes results in intermediate valued frequencies deviating from the pure LO and TO modes of well-defined oriented crystallites due to the phonons propagating between crystal symmetry axis. Quasi longitudinal optical phonon mode frequency lies between the frequency of pure $E_1(LO)$ and pure $A_1(LO)$ of the bulk material while the transverse optical mode falls between the frequency of pure $E_1(TO)$ and pure $A_1(TO)$. For our case where polycrystalline CdTe grains consists of varied sizes and orientation, quasi nature of the phonon modes is observed. This is verified by the well-known Loudon's model calculations.

According to this model, the quasi LO mode frequency can be described from the relation

$$\omega_q{}^2(LO) = \omega^2{}_{A1(LO)} \cos^2\theta + \omega^2{}_{E1(LO)} \sin^2\theta \qquad (5)$$

Where θ is the phonon propagation angle with respect to c- axis of the crystal lattice [132]. By rearranging equation 5 and ignoring the higher order terms, we have

$$\langle \omega_q(LO) \rangle = \left[1 + \frac{1}{3} \frac{\omega^2{}_{A_1(LO)} - \omega_o{}^2}{\omega_o{}^2} + \frac{1}{6} \frac{\omega^2{}_{E_1(LO)} - \omega_o{}^2}{\omega_o{}^2} \right] \omega_o \qquad (6)$$

From equation 6, ω_o can be given as

$$\langle \omega_q(LO) \rangle^2 = \omega_o{}^2 = \frac{2\omega^2{}_{A_1(LO)} + \omega^2{}_{E_1(LO)}}{3} \qquad (7)$$

Inserting the values for $A_1(LO)$ and $E_1(LO)$ modes as reported as 169.4 cm^{-1} and 156.1 cm^{-1} respectively, we obtain quasi LO mode at 165.1 cm^{-1} which is very close to the observation at 166 cm^{-1} in our study, thus can be associated with the quasi phonon modes nature.

3.5. Conclusions

We have characterized as deposited and $CdCl_2$ treated polycrystalline CdTe thin films deposited by e-beam evaporation techniques. Temperature dependent PL spectra reveal energy transitions at 1.577 eV which is assigned to electron to acceptor transition while a donar to acceptor transition occurs at 1.573 eV. A broad spectrum at 1.45 eV is associated with A-center chlorine based acceptor complex. AFM study on the grain sizes for as grown and chlorine treated films revealed grains of 0.2 μm and approximately 2-3 μm respectively. Quasi mode nature for the LO phonon modes of mixed symmetry is observed from the Raman spectra of the polycrystalline CdTe structures at 166 cm^{-1} whereas A1 and TO modes at 118.9 cm^{-1} and 136.5 cm^{-1} respectively correspond to phonon vibrations from hexagonal Te structure indicating Te rich surface.

4. SYSNTHESIS OF UNIFORM GOLD NANOPARTICLE ARRAYS AND NANOPOROUS TEMPLATES USING BLOCK CO POLYMER LITHOGRAPHY

Historical and modern use of metallic nanoparticles and block co polymers are discussed already in Chapter 1. In this chapter, high-density arrays of gold nanodots and nanoholes on indium tin oxide (ITO)-coated glass surfaces are discussed that are fabricated using a nanoporous template fabricated by the self-assembly of diblock copolymers of poly (styrene-*block*-methyl methacrylate) (PS-*b*-PMMA). By balancing the interfacial interactions between the polymer blocks and the substrate using random copolymer, cylindrical block copolymer microdomains oriented perpendicular to the plane of the substrate have been obtained. Nanoporous PS films are created by selectively etching PMMA cylinders, a straightforward route to form highly ordered nanoscale porous films. Deposition of gold on the template followed by lift off and sonication leaves a highly dense array of gold nanodots. These materials can serve as templates for the vapor-liquid-solid (VLS) growth of semiconductor nanorod arrays for optoelectronic applications. Figure 11 represents schematic illustration for our fabrication steps in formation of gold nanodots that will be explained in detail in this chapter.

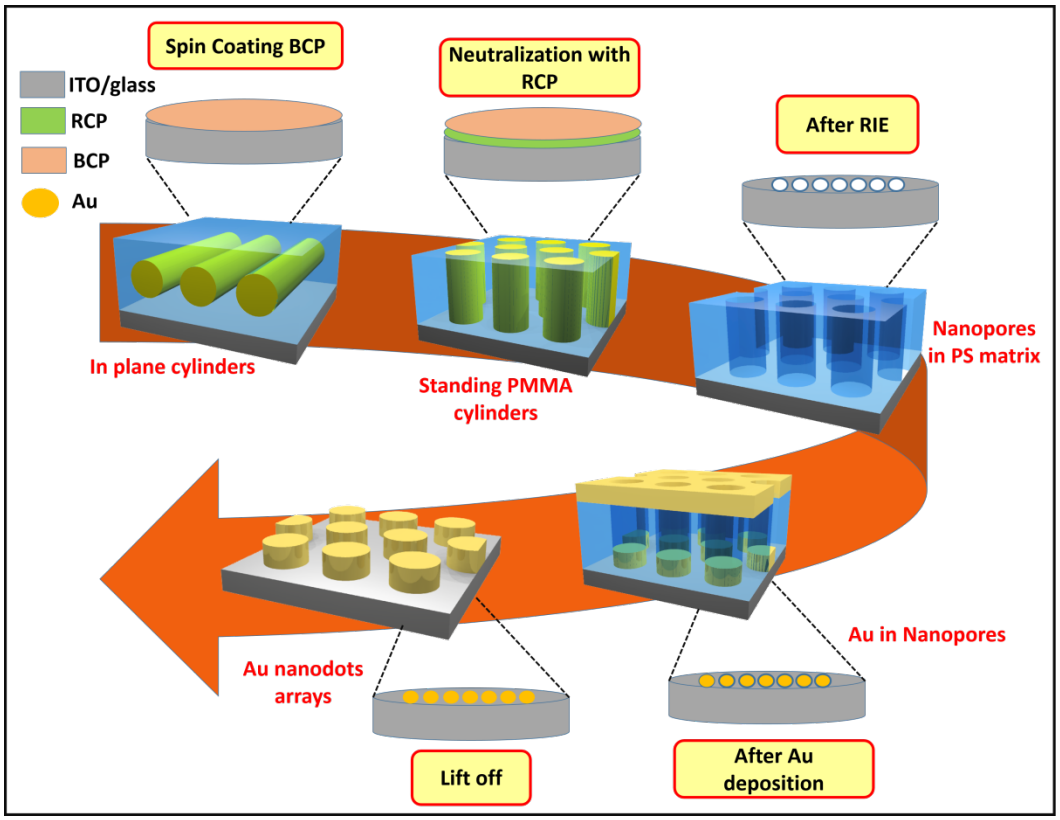

Figure 11: Schematic illustration of process flow for the formation of gold nanoparticles using block copolymer nanolithography

4.1. Experimental Protocol

Block copolymers of polystyrene (PS) and poly (methyl methacrylate) PMMA with a moderately asymmetric weight composition of 30% of PMMA and 70% PS have been utilized in this work to obtain a nanoengineered template on ITO-coated glass substrates. The diblock copolymer of poly (styrene-*block*-methyl methacrylate) (PS-*b*-PMMA) was purchased from Polymer Source, Inc. and purified using Soxhlet extraction to remove excess homopolymer. The number-average molecular weight for PS is M_n=68,000 g/mol and M_w=73,000 g/mol with a polydispersity index (PDI) of 1.08. The surface of thin films was characterized using tapping-mode atomic force microscopy (Nanoscope V, Veeco) in order to observe the topography.

4.2. Preparation and neutralization of substrate

Controlling the orientation of microdomains in thin films is a key parameter for fabricating block copolymer nanostructures. For obtaining cylindrical microdomains perpendicular to the plane of the substrate, an ultra-thin cross-linkable brush film of a random copolymer (RCP) of poly (styrene-*ran*-methyl methacrylate) (PS-*r*-PMMA) is utilized in this work for interface-energy neutralization of the surface before application of BCP films. This treatment ensures there are no preferential interactions of either of the two polymer blocks with the substrate. Using this technique, the surface energy of the substrate is controlled by tuning the relative composition of the RCP and thus can be optimized for a particular BCP.

ITO surface preparation for the application of BCP was done initially by dipping the substrate in a solution of H_2O_2/ NH_4OH/ DI H_2O at a ratio of 1:1:5 on a hot plate at 60^oC for 3 hrs. This step is essential to generate OH^- bonds on the ITO surface to enhance bonding with the random copolymer film. Further DI water rinsing and air gun drying of ITO completed the cleaning procedure. For surface neutralization, a random copolymer of PS-*r*-PMMA is used. The solution was prepared using 1% (w/w) of PS-*r*-PMMA mixed in toluene with $f_{PS} = 0.59$. 100 ml of this solution was spin coated at 2000 rpm for 40-50 sec while keeping it on a hot plate in a N_2 atmosphere at 250 °C for 30-35 min. This procedure results in a ~40 nm-thick film of random copolymer. Since we need a relatively thin RCP layer for providing an adhesion layer for application of the BCP, excess RCP was removed using toluene rinsing. Following rinsing, the RCP film thickness is reduced to a ~7 nm brush layer.

4.3. Application and orientation of block copolymer (PS-b-PMMA) nanostructures

Solutions of PS-*b*-PMMA were prepared in the same manner as with the RCP using 1 wt% BCP mixed in toluene and applied using spin coating. Direct application of PS-*b*-PMMA on ITO-coated glass substrates results in formation of in-plane or mixed morphology of PMMA cylinders surrounded by a PS matrix as shown in figure 12(a). In-plane microdomain orientation is due to the unbalanced interfacial interactions between the ITO substrate and the polymer blocks, thus application of RCP for surface modification becomes an essential step in fabricating vertically oriented PMMA cylinders.

75 ml of the 1% (w/w) PS-*b*-PMMA solution with $f_{PS} = 0.7$ was spun at 2500 rpm for 45 sec after substrate neutralization with PS-*r*-PMMA followed by annealing the samples in a vacuum oven at 190 °C for 24 hours. This step resulted in highly oriented vertical PMMA cylinders of ~25 nm diameter surrounded by a PS matrix as shown in figure 12(b). Annealing conditions and film thickness were optimized to both promote microphase separation of the BCPs and to obtain uniform standing-cylinder morphology.

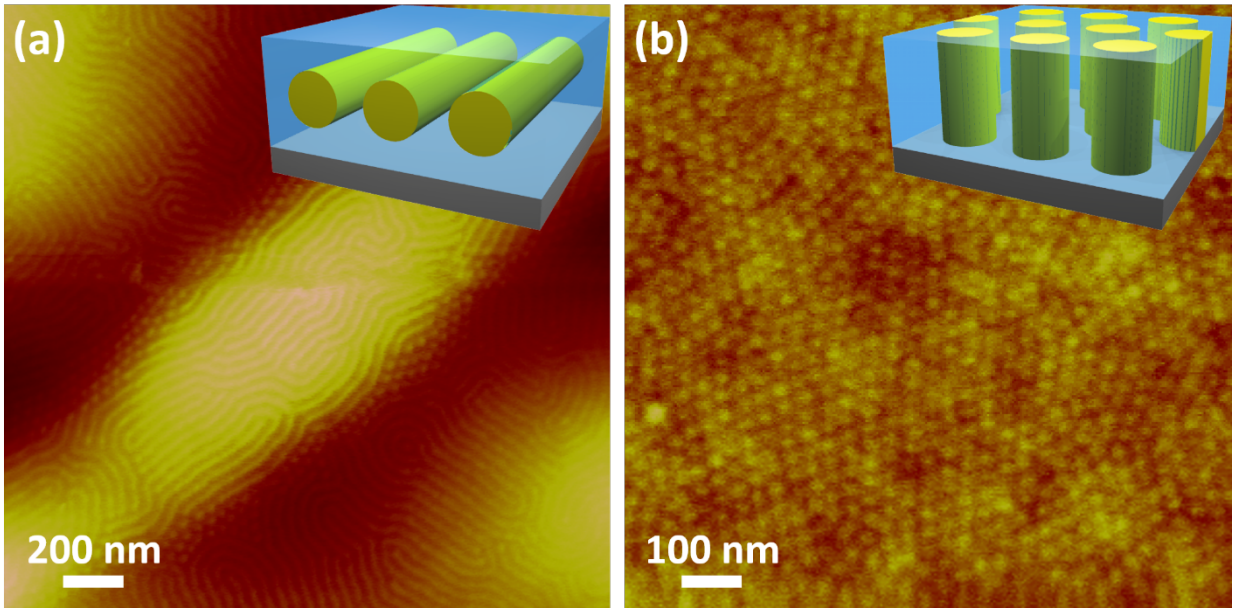

Figure 12: (a) Atomic force micrograph (topography) of a self-assembled BCP film (in-plane cylinders) obtained by direct application of BCP on the ITO surface, (b) Atomic force micrograph of a self-assembled BCP film on ITO (standing cylinders) after RCP surface.

4.4. Nanopatterning

In order to remove PMMA cylinders from the PS matrix, reactive ion etching (RIE) is applied. This RIE tool (March Plasma RIE CS-1701) was used under oxygen atmosphere at a power of 40W for ~40 sec keeping the pressure at 160 Torr. Since the PMMA oxygen plasma etching rate is faster than that for PS, RIE selectively removes the PMMA domains resulting in a smooth nanoscale geometry of closely packed holes in a PS matrix on the ITO surface. Formation of closely packed nanoscale pores of diameter 25 - 30 nm are shown in figure 13(a). RIE parameters were adjusted to ensure that not only were the PMMA microdomains completely removed, but also the random copolymer brush layer residing under the BCP film. After obtaining a nanoporous PS

template on the ITO substrate, ~4 nm thin Au film was sputtered over this nanoporous template using an Emitech K675X Sputtering tool at a deposition rate of 0.1 A^{o}/sec as shown in figure 13(b).

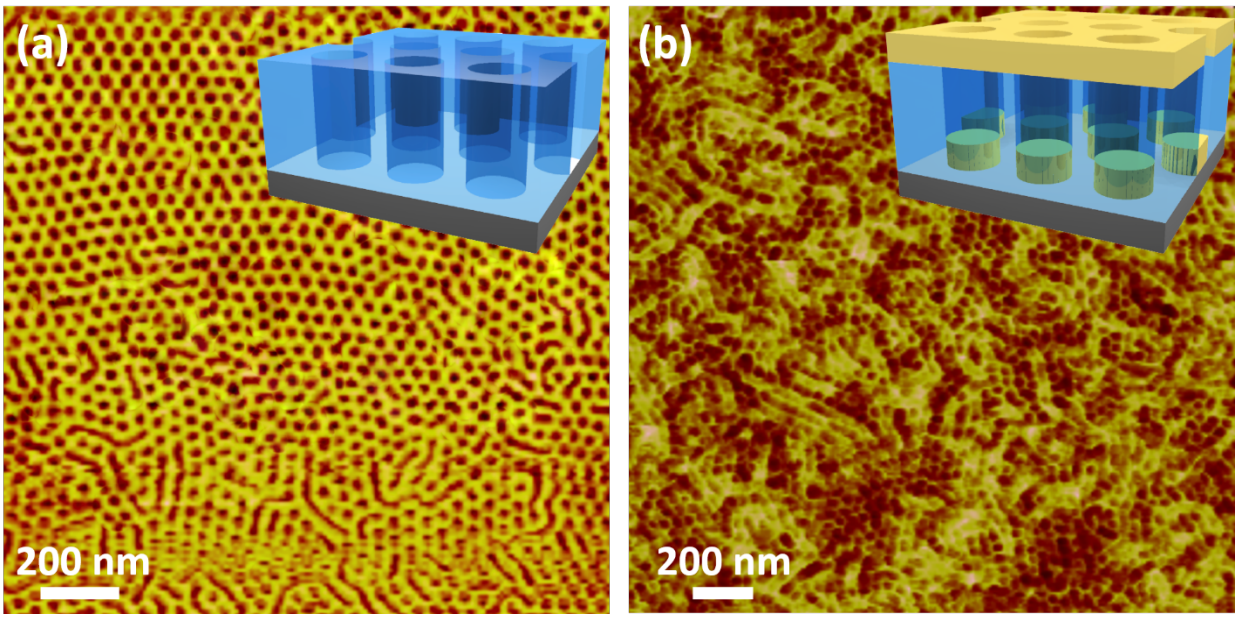

Figure 13: (a) AFM height image of closely packed nanoscale pores of diameter 25 - 30 nm following RIE treatment of the BCP film (now comprised of PS only) (b) AFM height image of the textured film following Au deposition.

In order to remove the PS mask and the gold on top of the mask, a lift-off technique was adopted. Lift off was achieved by sonicating the sample in photoresist remover (1165, Shipley Ltd.) for 10 min under room temperature in order to etch the underlying cross-linked PS matrix along with the overlaying Au so that only the Au sitting within the pores of the PS template remained on the surface to form the nanoscale features. These samples were washed in deionized water and dried by blowing N_2 gas on the surface. After drying, a final, brief RIE in oxygen plasma was done for 5 s in order to remove the remaining organic material. Densely packed nanosized Au dots of about ~25

nm in diameter and center-to-center spacing of ~30 nm is revealed as shown in figure 14. Particle analysis reveals similar features when compared to the PS template showing spacing between particles around 35 - 40 nm and dot size of 25 - 30 nm, which is in line with the reverse pattern of the PS porous matrix. Thus successful formation of closely packed Au nanoparticles is obtained using a simple and high-throughput block copolymer lithography technique as compared to conventional serial lithography techniques.

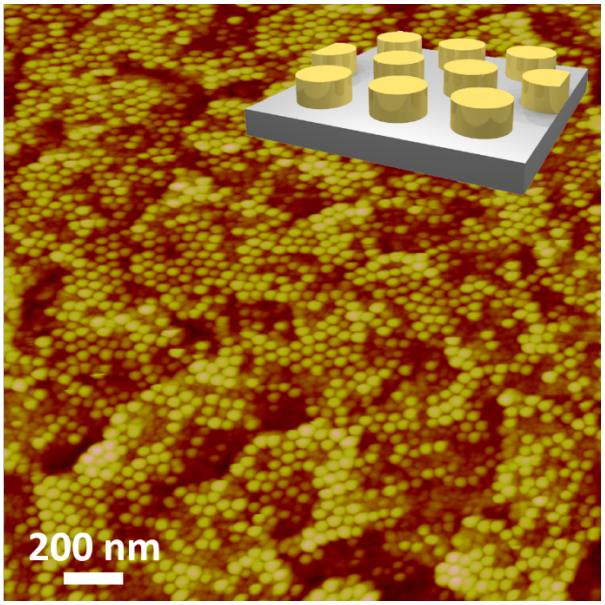

Figure 14: AFM topographic image of <30 nm Au nanodot array following the liftoff procedure.

4.5. Applications in fabricating hybrid photovoltaic cells

Block copolymer self-assembly can be utilized for many technologies, including photovoltaic applications [133]. Owing to the property of BCPs to create uniform, ordered, and dense nanoscale patterns over a large area with morphological tunability, efficient generation and extraction of photogenerated charge carriers are achievable [134]. Thus, an array of Au nanoparticles fabricated using BCP-based techniques can be utilized for the synthesis of hybrid PV devices using inorganic and organic materials such

as CdS and P3HT as *n*-type and *p*-type materials, respectively. Au nanoparticles can serve the role of catalyst in the formation of CdS nanorods with high aspect ratio using vapor-liquid-solid (VLS) growth; such an approach is anticipated to result in high-density, closely packed arrays of CdS nanowires resulting in enhanced absorption efficiency [135]. These CdS nanowires can further be surrounded by a conjugated polymer matrix resulting in improved photocarrier separation and enhanced conversion efficiencies. A schematic illustration for such hybrid CdS/P3HT PV cell is presented in fig. 17 to understand the picture with more clarity.

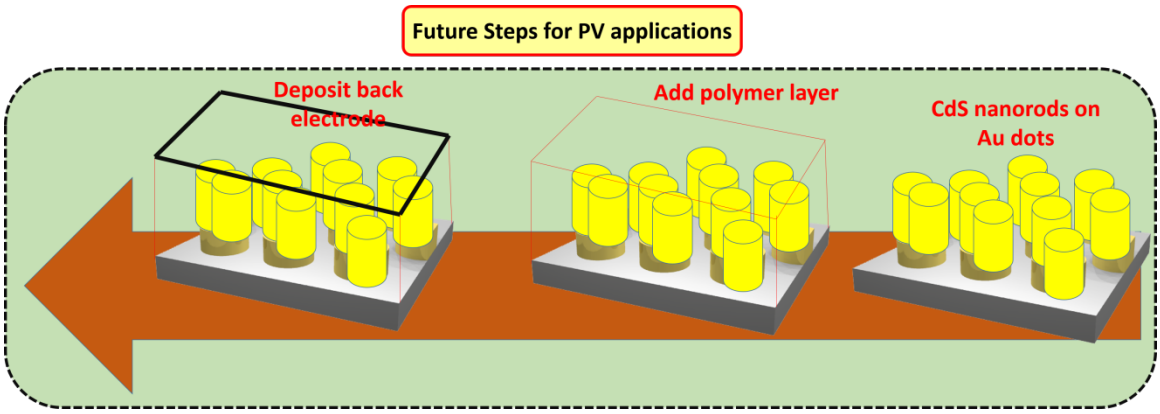

Figure 15: Schematic illustration for the future steps of CdS/polymer based hybrid PV device.

4.6. Conclusions

A simple and flexible route to the fabrication of nanoscale arrays of Au metal dots and nanoporous films has been presented. Block copolymer self-assembly is used to fabricate oriented cylindrical microdomains with potential use either as a positive or a negative template. In this context, the cylindrical patterns we obtained can be extended further into not only applications in photovoltaics but also fabrication of high-density arrays of more complex or striped patterns that can be utilized for bit-patterned media and in the semiconductor industry. After removal of cylinders and cleaning the pores with

oxygen plasma etching, successful fabrication of highly dense Au nanoparticles is realized on the nanoporous film. These materials are anticipated to be of use in the fabrication of hybrid solar cells involving inorganic semiconductor nanorods grown using VLS methods.

5. ZINC OXIDE NANOWIRES: OPTICAL, STRUCTURAL AND ELECTROSTATIC FORCE ANALYSIS UNDER DIFFERENT GROWTH CONDITIONS

We have fabricated various shaped zinc oxide nanostructures via controlled growth atmosphere using VLS growth mechanism and studied its optical, structural and electrostatic force characteristics in detail. Further a unique method is developed to study spontaneous polarization induced electric field from zinc oxide nanowires and nanostars using electrostatic force spectroscopy technique. Such an effect in these nanostructures due to inbuilt spontaneous polarization can be utilized for many applications such as nano-bio interfaces or HEMT structures that takes advantage of inbuild electric field from polar crystals that lacks an inversion symmetry, thus opening up many possibilities in various applications.

Zinc oxide (ZnO) materials have attracted great interest in the last decade due to their potential applications in the field of optoelectronics, spintronic, sensors, energy storage, piezoelectric and thermoelectric devices [79-80]. ZnO has a large band gap of 3.37 eV at room temperature which corresponds to near ultra violet region. It has a large excitonic energy of ~ 60 meV that makes it a favorable candidate for many applications such as laser diodes or light emitting diodes (LEDs) [136]. Due to such rapid progress on nanoscale electronics and optical devices, one dimensional semiconductor nanowires or nanobelts have gained significant attraction in past years because of their unique electrical and optical properties. These 1-D semiconductor nano structures have a broad range of applications ranging from sensors, field effect transistors (FETs), opto electronics devices and piezo electronics [137]. Among the 1-D semiconductor, huge

variety of electronic and chemical properties of semiconductor metal oxide materials made them exciting candidate for technological applications. Thus zinc oxide (ZnO) is an important material amongst these metal oxide semiconductors that is used in number of optoelectronic devices.

Due to promising applications of zinc oxide nanomaterials, it is of utmost need to control the shape of nanocrystals and study their optical properties that can be employed for many applications. Inspite of significant advances in growth and development of ZnO nanowires, various growth conditions and mechanism still remain incompletely understood and is a subject of discussion. Altering growth conditions could result in entirely different morphology that could change the device properties. Different shapes such as nanowires, tetrapods, flower-like structure or nanobelts have been reported in the past [138-139]. In this work, we have studied the morphology, luminescence properties and spontaneous polarization effects of ZnO nanostructures grown under different conditions and demonstrated formation of complex nanostructures under varying growth conditions.

5.1. Growth mechanism of ZnO Nanowires

Different fabrication techniques have been reported in order to synthesize zinc oxide nanostructures such as vapor phase transport [140], metal organic chemical vapor deposition (MOCVD) [141], thermal evaporation [142], hydothermal synthesis [143], solution based synthesis [144] etc. We have used vapor liquid solid (VLS) growth in our work in order to grow zinc oxide nanostructures. This technique is based on carbothermal reaction process which is typically divided into three steps [145].

- First step involves preparation of a liquid alloy droplet of nano sized dimensions on which the nanowire is grown.
- Secondly introduction of the grown substance and dissolution of gaseous reactants are done that diffuses on the catalysts droplet and adsorbs on the liquid-surface phase.
- Formation of nuclei, growth of nanowires and further super saturation of the wires at its liquid solid interface leads to formation of single crystalline axial crystal growth of nanowires.

Our reaction source for the VLS growth of ZnO NWs consists of zinc oxide powder mixed with graphite in a weight ratio of 1:1 in order to carry a carbothermal reaction. We have chosen Au as a catalyst seed for the growth of ZnO NWs for a variety of reasons. At the growth temperature of ZnO NW, gold (Au) catalyst forms a liquid solution with the crystalline material which is one of the main requirements for the catalyst to be chosen. Secondly Au is inert to the reaction products and also possess a small equilibrium vapor pressure over the alloy which makes it a favorable candidate to use as a catalyst to grow ZnO NWs. It is also well documented that physical characteristics of nanowires grown by described VLS growth mechanism grow favorably only in the areas that is activated by these metal seeds and the size and position of the wires are determined by that of the metal catalysts [146]. This is true but in some cases the diameter of NWs is not constant along the length of wires and also based on different growth mechanism and experimental conditions, complex nanostructures can be obtained instead of only nanowires.

ZnO has proven to be an interesting as well as complex material at the same time that can form a variety of structures such as nanowires, tetrapods, nanobelts, flower-like

structures based on different growth mechanisms and under different thermodynamic conditions [138-139]. These different shapes of the semiconductors at the nanoscale sizes can find unique applications in photonics and electronics. Inspite of considerable advances in the growth mechanism of ZnO NWs, growth of such complex nanostructures still remains controversial and a subject to immense discussion. Detailed clarification on the role of different experimental conditions that could result in complex ZnO structures is discussed and their optical and structural properties are investigated.

5.2. Experimental procedure for growth of ZnO nanowires

VLS growth of ZnO NWs is carried in a 2" diameter quartz tube at atmospheric pressure with the tube inserted inside an isothermal furnace. The source mixture was placed in the center of the quartz tube with source consisting of zinc oxide (99.99%, Sigma Aldrich) mixed with graphite (Aldrich Company) in a weight ratio of 1:1. The silicon substrate (n-type, 100 plane) with 4 nm gold catalyst is placed downstream from the quartz tube 2 cm away from source powder. Gold is deposited on Si substrate using e-beam evaporation tool (Varian) at a deposition rate of 1 A^o/s. One end of the tube was connected to a gas flow controller (Argon for our case) while the other end was outflowing gas through the exhaust. The system was heated at 910 ^oC with a constant gas flow of Ar at ~150 sccm for ~ 40-50 min after the system was stabilized at desired temperature. The schematic for the VLS growth setup is depicted in figure 16.

The carbothermal reaction at the growth temperature can be explained as the following reaction equations:

Carbothermal reaction: $ZnO(s) + C(s) = Zn(v) + CO(g)$ (8)

Catalyst alloy formation reaction: $Zn(v) + Au(s) = Au - Zn(l)$ (9)

Overall NW formation reaction: $Au - Zn(l) + Zn(v) + \frac{1}{2} O_2 = Au - Zn(l) + ZnO(s)$ (10)

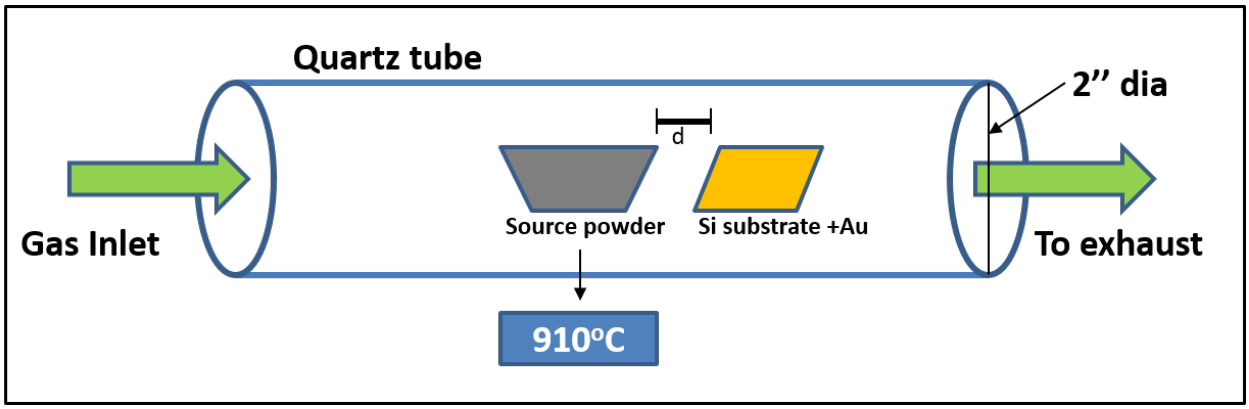

Figure 16: Schematic of VLS growth setup.

5.3. Investigations into growth conditions and structures of ZnO Nanowires

Four different growth mechanisms and conditions have been tried and discussed here.

1. Sample A: Improper growth of Zinc oxide Nanowires

Figure 17 (a)-(b) shows the scanning electron microscopy (SEM) images of improper ZnO NWs growth. SEM was carried using a variable pressure S-3000N Hitachi instrument. For the *sample A*, VLS growth was carried out at the desired temperature of 910 ^{o}C at a constant Ar gas flow for ~ 45 min. The gas flow for this growth was kept lower at ~60 sccm that results in inappropriate or almost no growth of nanowires on Silicon substrate keeping in view our wider diameter quartz rod for VLS growth (2'' dia). Appropriate gas flow is important to transfer the zinc oxide vapor onto the substrate that will result in formation of nanowires assisted with catalyst seed. Rate of gas flow should

vary between one research group to another depending on their diameter of tube, growth temperature, duration and pressure.

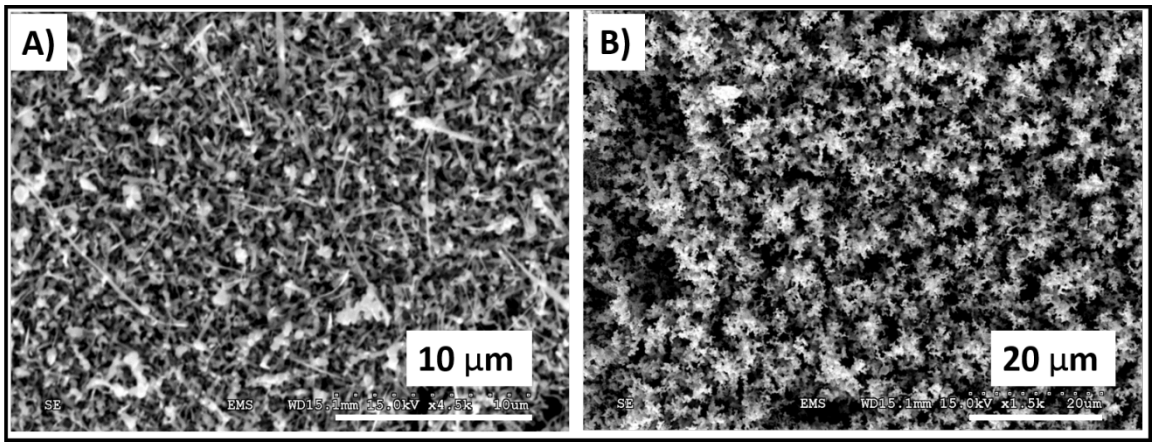

Figure 17 (a)-(b): Sample A: SEM images showing inappropriate growth of zinc oxide nanowires at different scale bars

2. Sample B: As-grown ultra-long single crystalline ZnO Nanowires under appropriate growth conditions

Figure 18 shows SEM images for the growth of as-grown ZnO nanowires under appropriate growth conditions as described in section 5.2. The grown ZnO nanowires have an average diameter of 50-100 nm and they are ultra-long nanowires with average lengths of approximately 50-100 μm. Figure 18(a)-(d) shows images at different scale bars showing densely pack nanowires on the whole surface. Diameter of the nanowires appears to be uniform throughout their axis. We investigated more into the crystallinity of these as-grown nanowires using transmission electron microscopy (TEM) measurements using JEOL JEM 3010 electron microscope as shown in figure 19. Inset of figure 19a shows a HR-TEM image of a 65 nm diameter as grown ZnO nanowire where the zone pattern coherence in the SAED structure is also indicated in figure 19(a) which clearly

indicates that the nanowire is single crystalline. These zinc oxide nanowires have a hexagonal crystal structure with the nanowires preferentially grow along the [0001] direction (figure 19b). At this point it is important to realize that because of the sample preparation process involve in TEM measurements, this may not give us accurate wire dimensions as expected. EDS measurements is also made on many as-grown nanowires showing indication of zinc and oxygen in all samples as shown in figure 19c.

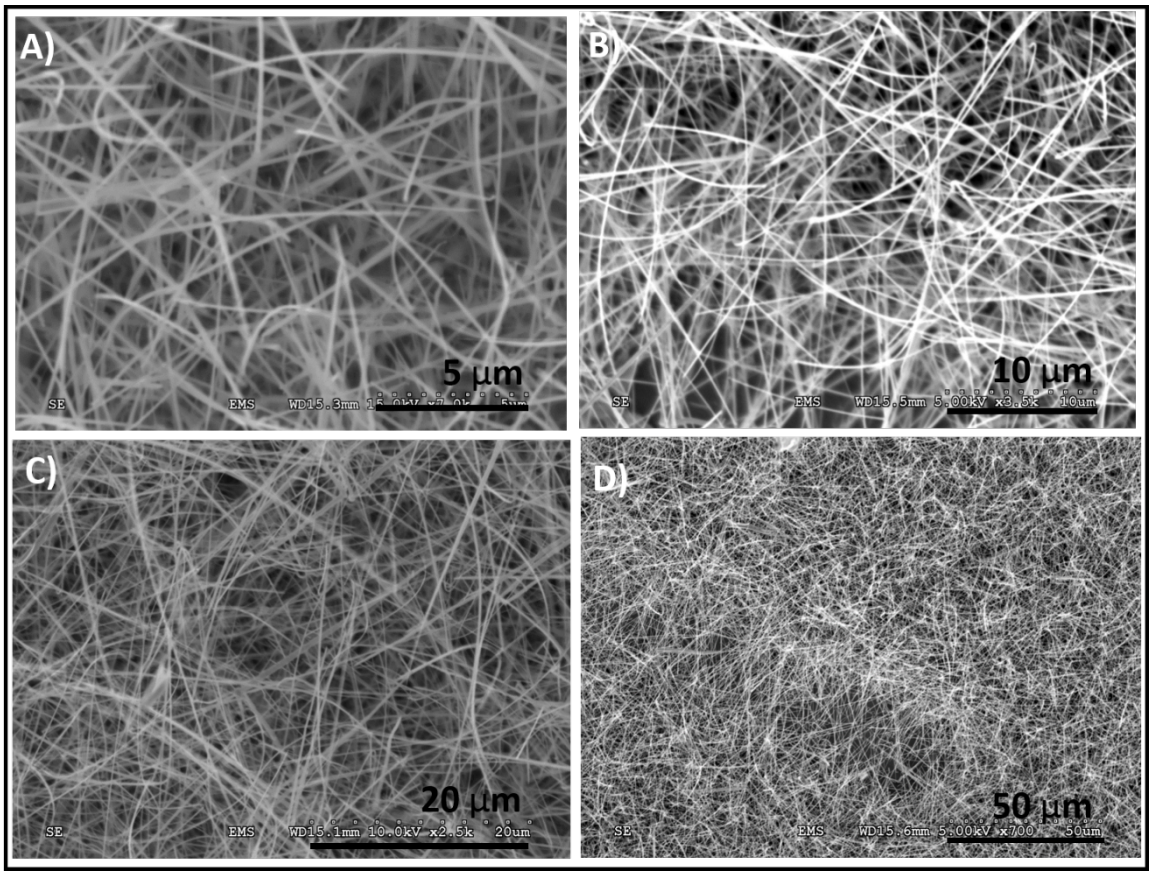

Figure 18 (a)-(d): Sample B: SEM images of ultra long As-grown ZnO NWs under appropriate growth conditions with different scale bars images (5, 10, 20 & 50 μm respectively).

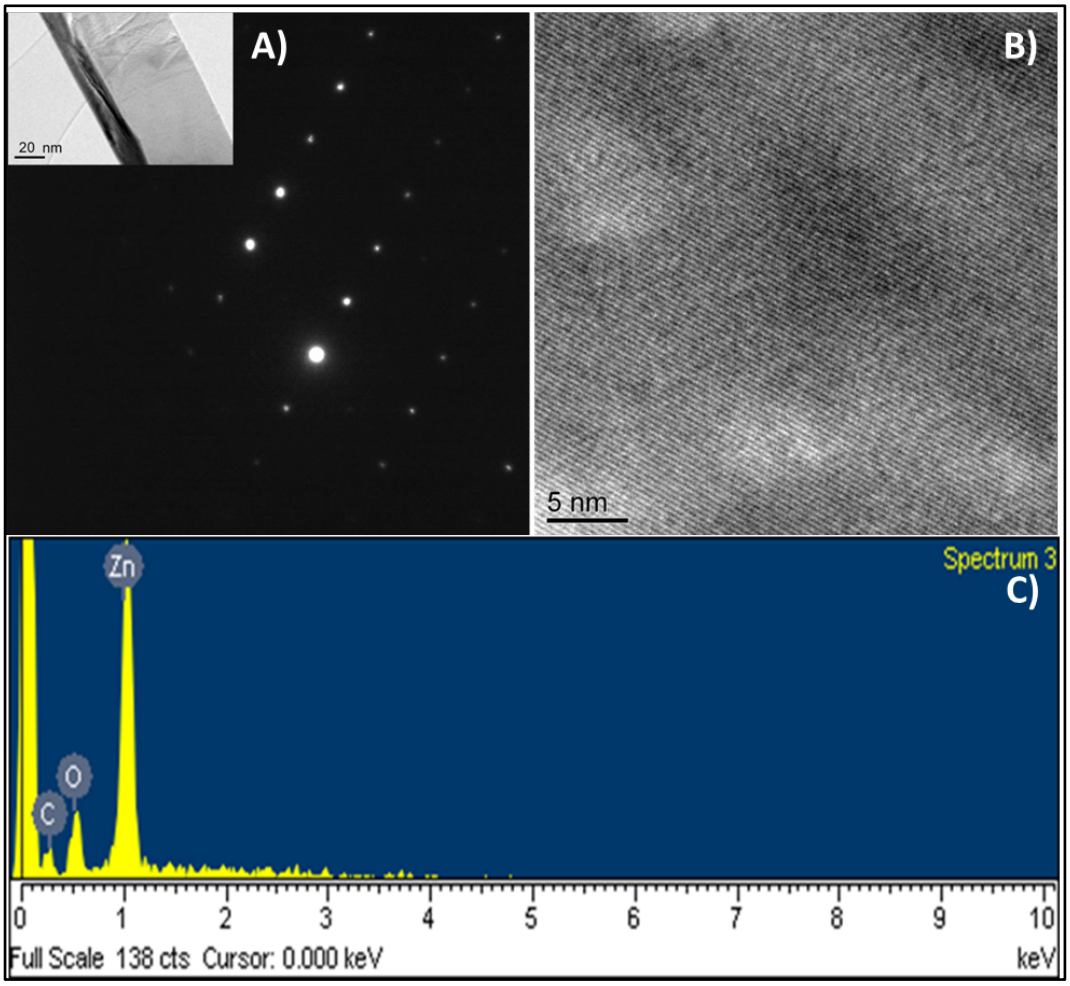

Figure 19: a) Selected area electron diffraction pattern (SAED) of ZnO nanowire; inset shows a TEM image of a single nanowires; b) Lattice fringes from a ZnO nanowire; c) XEDS profile of as grown ZnO nanowires showing zinc, oxygen and carbon content taken from a SEM operating at 5 keV.

3. Sample C: Over growth conditions for Zinc oxide Nanowires

Third case tested is the growth of ZnO NWs with the same gas flow as employed in appropriate growth condition for *sample B* but duration for growth increased to 1.5 hours after the temperature is stabilized at 910 ^{o}C. It is observed that increased growth time resulted in excessive multilayer growth of ZnO nanowires with wider diameter as

compared to *Sample B* as shown in SEM images in figure 20(a)-(b). For some cases, these excessive growths appear to be coated on top of a zinc oxide nanobelts structures as highlighted in figure 20(d) while in some cases nanowires appear to twist from the edges in the form of spirals (figure 22(c)). Oversupply of source vapors along with surface energies of the wires and the catalyst can result in instability of the ZnO nuclei resulting in such oscillatory multilayered growth of ZnO structures.

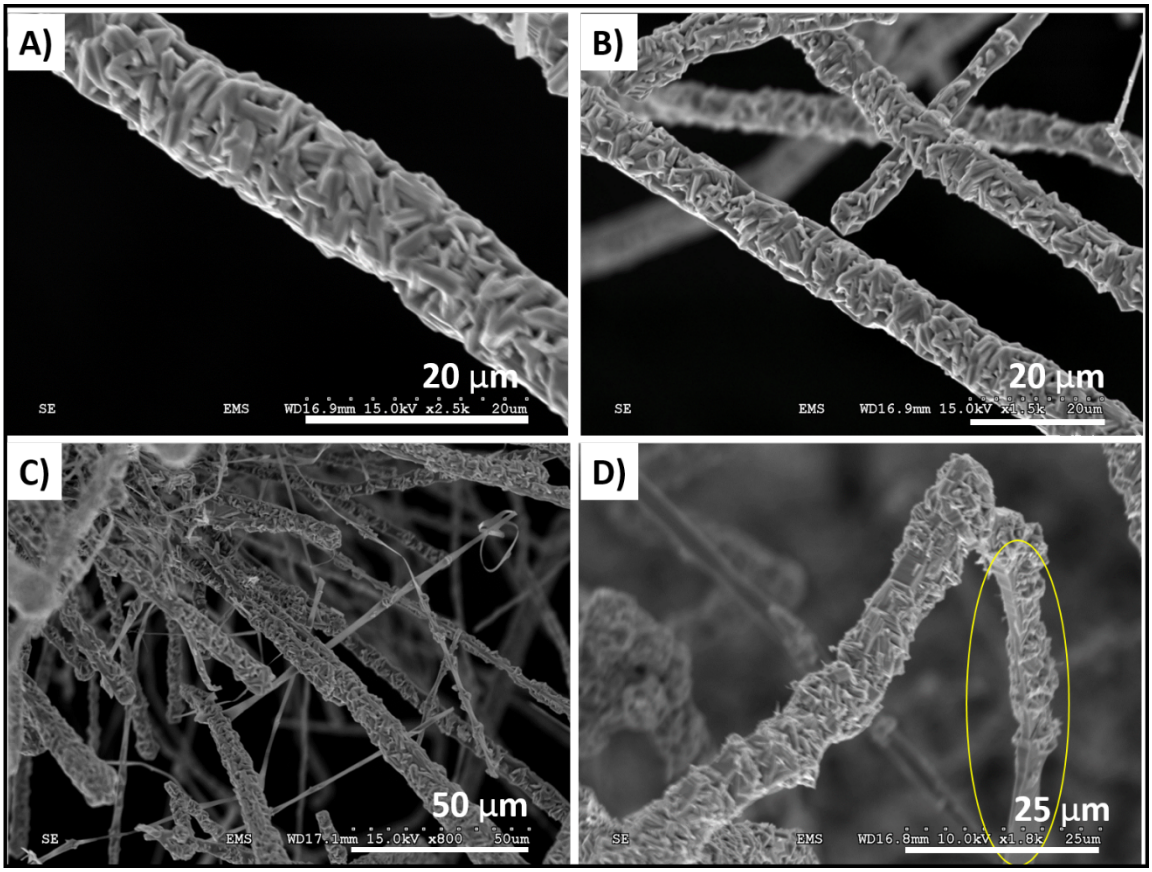

Figure 20 (a)-(d): Sample C: Over growth of zinc oxide nanowires at different scale bars; highlighted area in figure 20(d) indicates excessive growth layer on top of ZnO nanobelt-like structures.

4. Sample D: Star-shaped formation of Zinc oxide nanostructures

For Sample D; we kept the gas flow, temperature and duration exactly the same as *sample B* (appropriate growth condition) but we increased the distance of the substrate from the source *d* to ~ 6 cm. To our surprise, this condition resulted in star shaped nanostructures of ZnO as shown in SEM image in figure 21. The lengths of the legs of ZnO stars are ~ 1 μm while the center nucleus is ~ 200- 300 nm. Further investigation into the possibility of nanostars growth revealed that when the distance of the source and substrate is increased, the temperature of substrate is decreased. It is important to note that temperature at different positions of the quartz tube is different, source being in the middle of the tube is at the desired temperature (910 ^{o}C) but moving the substrate apart resulted in measured temperature of the substrate to be around 600-650 ^{o}C.

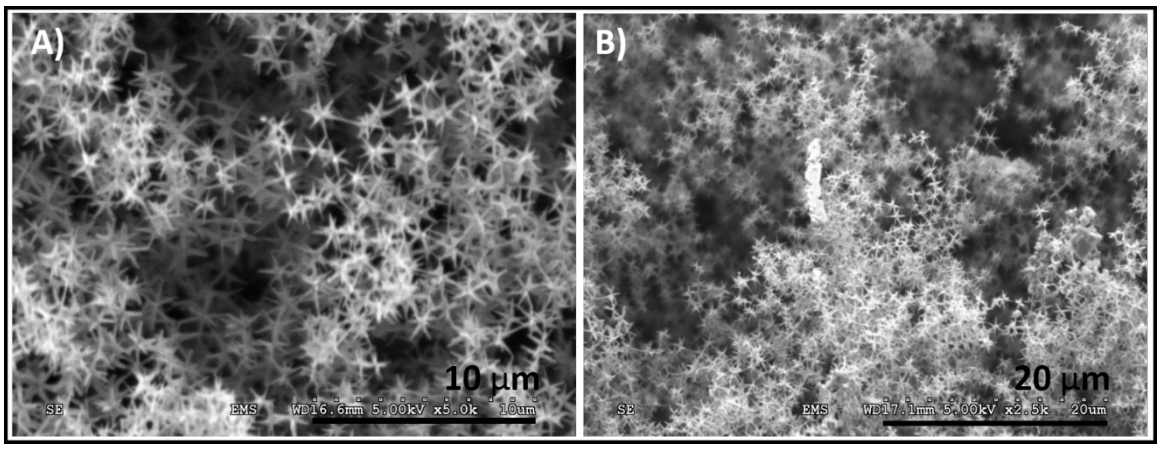

Figure 21: Sample D: Star-shaped formation of Zinc oxide Nanostructures; a) 0 degree angled image; b) 40 degrees angled image.

It is reported that morphology of the structures formed during VLS growth depends on number of factors including substrate temperature, concentration of Zn and O_2 vapors as well as surface diffusion rates [147]. Surface diffusion that is related to the

motion of molecules at solid material surfaces depends highly on temperature effects with the rate of motion typically increase with the increased temperature and vice versa. This can also be well explained by the surface diffusion kinetics (Γ) equation defined as [148]:

$$\Gamma = v \exp(-E_{diff}/K_bT) \quad (11)$$

Where E_{diff} be the potential energy barrier to diffusion, v being the vibrational frequency of the adatom, T the temperature and K_b is the Boltzmann constant.

For our case, in the lower temperature regime, a relatively lower surface diffusion rate occurs. This decreased surface diffusion rate and the decrease in supply of Zn and O_2 vapors results in affecting the rate of nucleation and growth morphology of zinc oxide crystals. After the substrate is loaded into the lower temperature region of the furnace, three step procedure possibly had happened which is also explained schematically in fig. 24.

a. Zn and O_2 vapors transported by the carrier gas (Ar) condense on the surface of Si substrate in the form of ZnO droplets (figure 22(b).
b. Formation of ZnO nuclei occurs from the ZnO droplets as the super saturation level increases (figure 22(c)).
c. Growth of nanowires/legs of ZnO nuclei happen at the preferred *c*-axis due to continuous feeding of source vapors from the ZnO nuclei but due to decreased surface diffusion energy and lower substrate temperature, growth stopped after formation of nanostars-like structures overlapping each other instead of ultra-long nanowires (figure 22(d)).

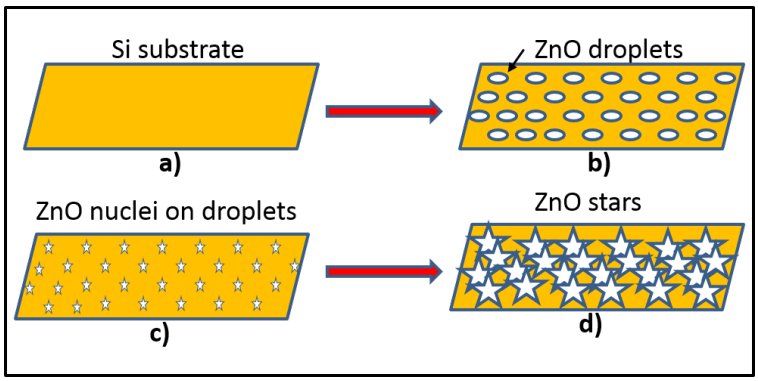

Figure 22: Schematic illustration of growth mechanism of star shaped zinc oxide nanostructures.

For the zinc oxide stars, a detailed TEM analysis is done as shown in figure 23. Fig 23 (a)-(b) shows the TEM image of a single ZnO star whereas figure 23 (c) and (e)-(f) shows the lattice fringes pattern of different areas (top, middle and bottom) of leg 5 of ZnO NS. If we see the lower part of leg SAD5, we can clearly see that the lattice fringes reveals single crystallinity. However if we see the junction of the two legs of star, we see mixed fringes pattern in two or more directions along with ripple like contrast most likely coming from the strain occurring at the intersection of the two legs. Figure 23(d), (g)-(m) shows SAED pattern of all the legs of a nanostar. Individually all the legs indicates single crystallinity but if we see the overall star, *c*-axis for all different legs are pointing in different directions depending on the growth direction of the individual leg.

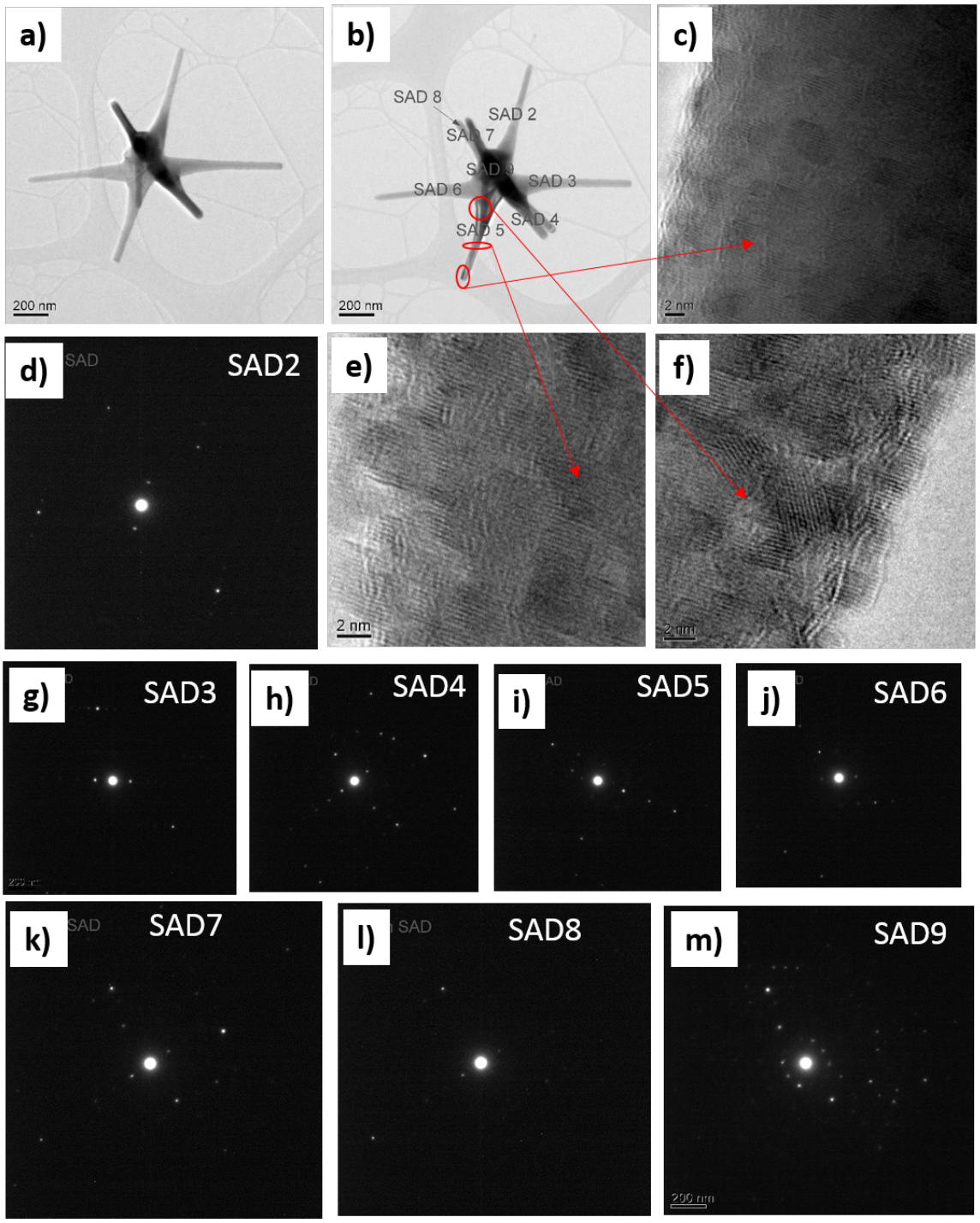

Figure 23: TEM images of (a)-(b) ZnO star showing corners of six legs marked; (c),(e),(f) HRTEM image showing lattice fringes of the selected area; (g),(e)-(f) SAED patterns of different areas of stars as indicated in image (b)

5.4. Photoluminescence studies of ZnO Nanostructures

1. Comparison of As-grown ZnO Nanowires and ZnO Nanostars

The room temperature PL spectra for the as grown ZnO nanowires *(Sample B)* is shown in figure 24. We observe a near band edge UV emission peak at ~381 nm which corresponds to about 3.25 eV. This emission band corresponds to free excitonic emission from the wide band gap of ZnO nanowires [149]. Another band at ~505 nm is also detected from the ZnO nanowires. This green emission is attributed to a point defect in the nanowire arising from the impurities or the structural defects. Such an emission band is usually associated with ionized oxygen vacancy and interstitials of zinc that originates from the recombination of a photo generated hole with the singly ionized charged state of the defect [150]. This peak is broad and seems to have another shoulder at ~ 470 nm. This could be the result of convolution of more than one peak in the structure resulting in broader spectrum. It is also noted that this green emission is much stronger than that from the UV emission. Such an enhancement is possibly related to the high quantity of the surface oxygen vacancies of the nanowires. These oxygen vacancies can cause defect levels to form close to the conduction band minima that can make an electron from the valence band to trap and contribute to the luminescence as seen in our case. These surface oxygen vacancies are extremely important in determining the conductivity of ZnO [151]. Large concentrations of intrinsic dopants can cause high conductivity in the device. One of the applications for these high mobility carriers can be in sensing applications.

We also did PL studies for the zinc oxide stars to reveal its optical properties as shown in figure 24. A very intensive sharp near band edge emission peak with full width half maxima of ~100 meV is observed as compared to nanowires whereas negligible or

no green emission is observed. This result indicates that the ZnO star shaped nanostructures shows less impurity or defect states that results in suppression of green emission as compared to as grown nanowires.

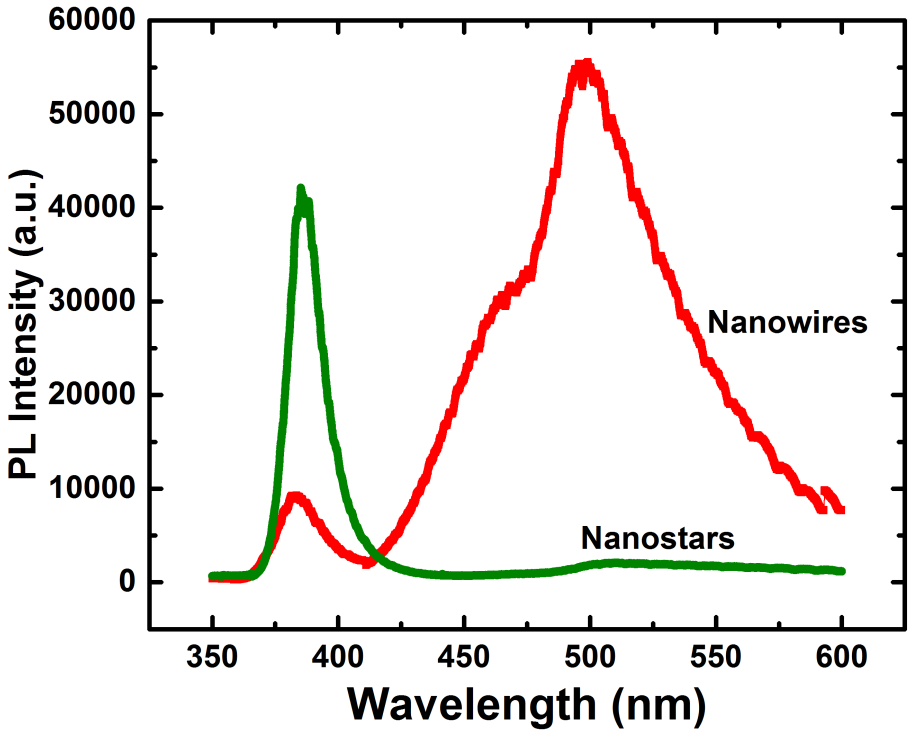

Figure 24: Room temperature photoluminescence spectra of ZnO nanowires and ZnO stars excited at 325 nm laser.

2. ZnO nanowires diameter dependent studies

It is also found that green emission of ZnO is also related to the diameter of the nanowire. We compared our nanowires having diameters ranging from 50-100 nm with the commercially available ZnO NWs with a much wider diameter of ~ 500 nm. We observe that thicker nanowires did not show any green emission as compared to thinner nanowires whereas UV emission is also enhanced as indicated in figure 25. This reveals that wires with thicker diameters possess fewer oxygen vacancies resulting in larger no.

of electrons getting trapped on the surface. Since the wires with wider diameters have larger oxygen anions surface concentrations, it results in more oxygen desorption causing a whole new distribution of electrons that are conducting [146]. Additionally strong UV emission peak is also obtained for thicker nanowires. It is also been modelled theoretically by researchers earlier that the ratio of near band edge emission to deep level emission intensities changes significantly with the diameter of nanowires [152]. Hence we have revealed through experimental measures that wires with thinner diameters shows more oxygen vacancies and hence can be utilized efficiently for sensing applications in terms of their conductivity.

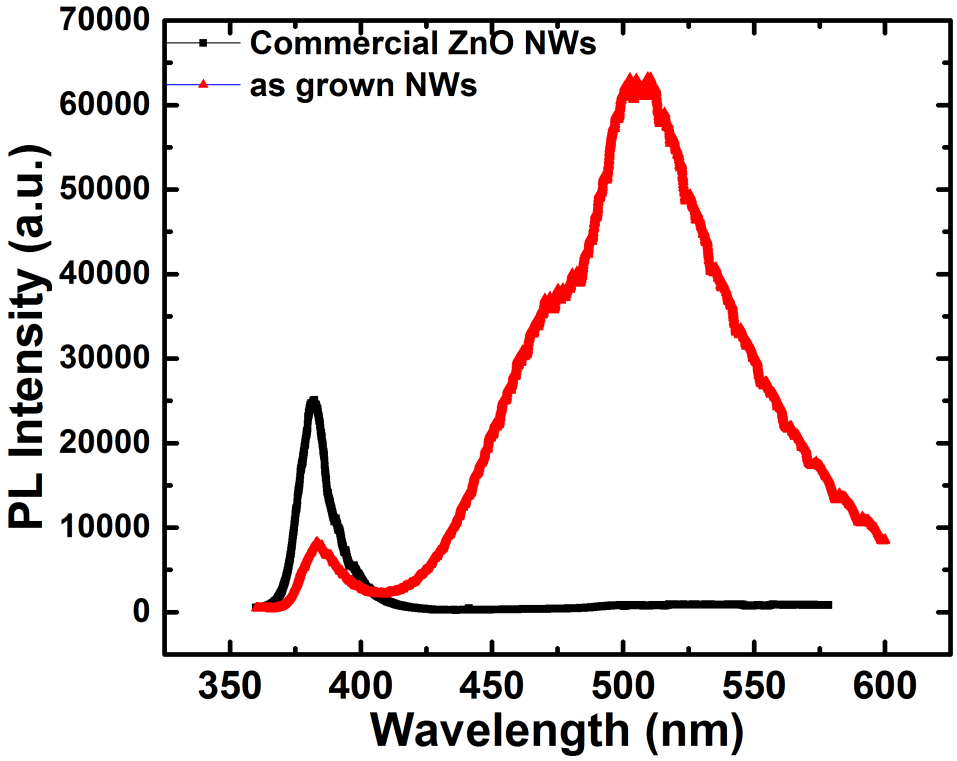

Figure 25: Photoluminescence spectra of ZnO nanowires with 50-100 nm diameter and ZnO nanowires with 500 nm diameters excited at 325 nm laser.

3. Low Vs high density of Zinc oxide nanowire arrays

We performed some photoluminescence analysis on the regions of samples with high density of zinc oxide as compared to low density of nanowires as shown in figure 26. We did not observe much difference in the near band edge emission for both the regions but it is seen that very highly densely packed nanowires shows significantly large green emission but less density of nanowires shows quenching of green emission band. This explains that denser the arrays of nanowires are, we expect to have more oxygen vacancies as compared to loosely packed nanowires arrays which are verified by our results.

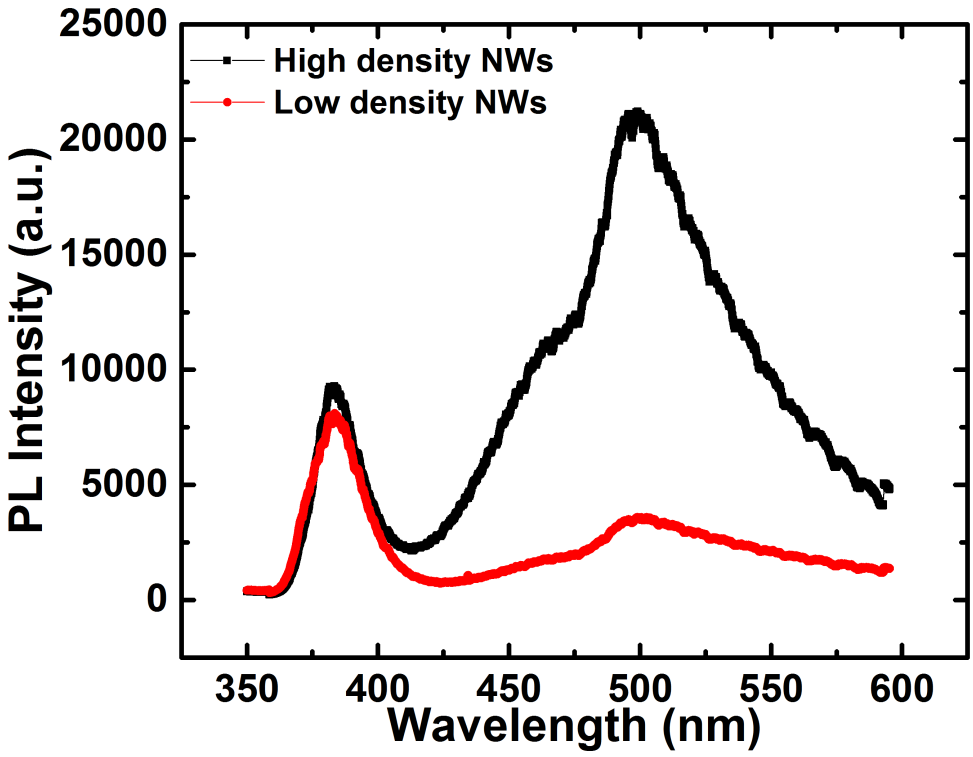

Figure 26: Room temperature PL spectra of as grown nanowires at densely packed (top curve) and less dense regions (bottom curve) of nanowires excited by 325 nm laser line.

4. Annealed induced effects on As-grown ZnO NWs

We did some post annealing treatment on ZnO nanowires. Two samples of nanowires underwent two different post growth treatments. For first sample, annealing was done at 500 ^{o}C under oxygen ambient whereas for second sample, annealing was carried out at 700 ^{o}C in O_2 atmosphere. After annealing in oxygen, intensity of green emission as well near band edge emission decreased as compared to as grown nanowires (figure 27). These suggest that overall oxygen related defects level has decreased for heating treatments. This is also observed by Ye. Sun *et al.* 2006 and Cross *et al.* 2005 [153-154] who shows decreased emission in UV as well as visible region for annealing in O_2 atmosphere and explained this quenching to be attributed to decrease in oxygen vacancies within ZnO nanowires.

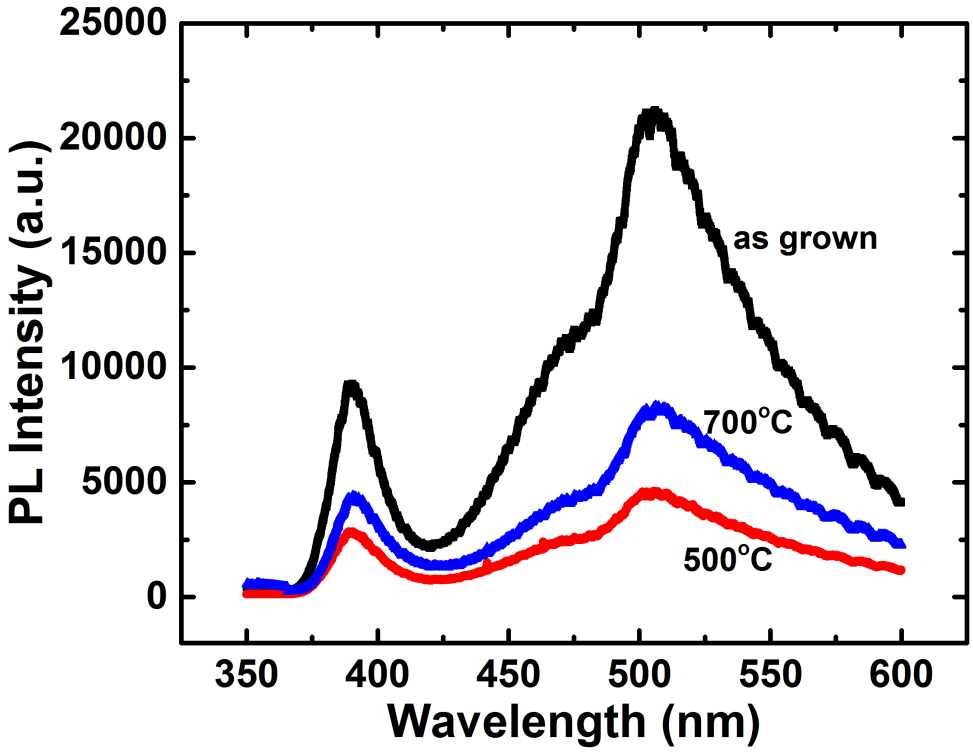

Figure 27: Room temperature PL spectra of ZnO nanowires annealed at 500 ^{o}C and 700 ^{o}C in oxygen for 2 hr.

5.5. Raman studies of ZnO Nanostructures

5.5.1. Raman of As-grown Nanowires

Figure 28 shows the Raman spectrum of as-grown ZnO nanowires measured at room temperature. With our randomly oriented nanowires, we observe Raman mode frequencies at 384.9 cm^{-1}, 440.5 cm^{-1}, 587.5 cm^{-1} and 335.6 cm^{-1}. ZnO as one of the simplest uniaxial crystal with its wurtzite structure belonging to C^4_{6v} space group. In case of perfect ZnO crystal, only the optical phonons at the Brillouin zone Γ point are involved in the first order Raman process [155]. According to group theory; for the wurtzite crystals, Raman active optical modes are A_1, E_1 and E_2 modes whereas B_1 branch is silent according to the following equation [156].

$$\Gamma_{(opt)} = A_1 + 2B_1 + E_1 + 2E_2 \qquad (12)$$

Where A_1 and E_1 modes are polar modes and consists of longitudinal optical (A_1 *(LO) and* E_1 *(LO))* and transverse optical (*A_1 (TO) and E_1 (TO))* components. E_2 mode also split into low and high frequency phonon modes (*E_2 (low) and E_2 (high))* that are related to the vibration of heavy zinc sublattice and O_2 atoms respectively. The Raman modes that are visible in a particular geometry are dictated by the Raman selection rules. Each active vibrational mode in a Raman spectrum corresponds to a particular band on the spectrum and intensity of these bands depends on the scattering cross section of these modes.

Depending on the polarization of incoming and outgoing light as well as particular crystal orientation with respect to light propagation, certain modes are allowed

and others are not in a particular configuration [132]. For our experimental setup, non-resonant laser excitation of 514 nm in a back scattering geometry is used. For this configuration, E_2-high mode is the dominant feature in the spectrum whereas for the case when the laser incident light is directed in parallel to the preferred *c*-axis of the nanowires, A_1 (LO) is also an allowed mode. Since we have nanowires oriented in random directions, the mode frequencies we observe at 384.9 cm^{-1} & 587.5 cm^{-1}, both seems to be slightly different from either of the E1 or A_1 modes of the Raman single crystals. We explained this discrepancy according to the quasi phonon modes nature.

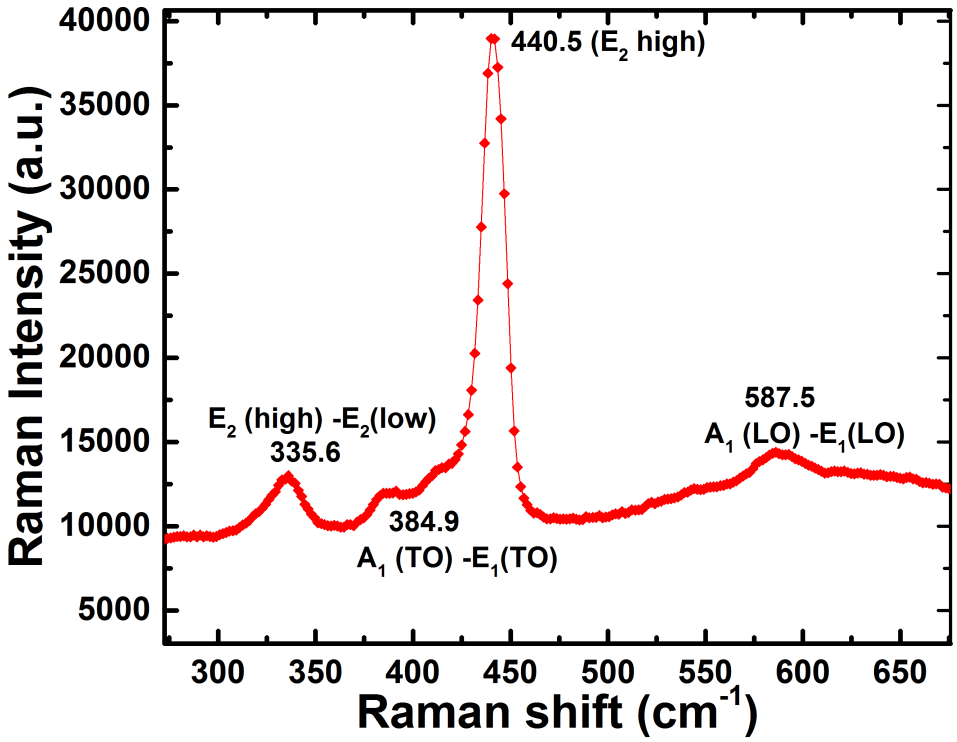

Figure 28: Raman spectrum of ZnO nanowires having 50 -80 nm diameters.

Theory of quasi mode nature of phonon is explained earlier in chapter 3. According to well known Loudon's model, quasi *TO* mode frequency should lie between

the frequency of pure A_1 *(TO)* and E_1 *(TO)* modes whereas quasi *LO* mode frequency should lie between the frequency of pure A_1 *(LO)* and E_1 *(LO)* [132]. The quasi *LO* and TO mode frequencies can be described according to the following relation:

$$\omega_q{}^2(LO) = \omega^2{}_{A1(LO)} \cos^2\theta + \omega^2{}_{E1(LO)} \sin^2\theta \tag{13}$$

$$\omega_q{}^2(TO) = \omega^2{}_{A1(TO)} \cos^2\theta + \omega^2{}_{E1(TO)} \sin^2\theta \tag{14}$$

Where θ is the phonon propagation angle with respect to *c*- axis of the crystal lattice. By rearranging equation *2* and ignoring the higher order terms, we have for the *TO* mode frequency described as:

$$\langle \omega_q(TO) \rangle = \left[1 + \frac{1}{3} \frac{\omega^2{}_{A_1(TO)} - \omega_o{}^2}{\omega_o{}^2} + \frac{1}{6} \frac{\omega^2{}_{E_1(TO)} - \omega_o{}^2}{\omega_o{}^2} \right] \omega_o \tag{15}$$

From equation 3, ω_o can be given as

$$\langle \omega_q(TO) \rangle^2 = \omega_o{}^2 = \frac{2\omega^2{}_{A_1(TO)} + \omega^2{}_{E_1(TO)}}{3} \tag{16}$$

Inserting the values for $E_1(TO)$ and $A_1(TO)$ modes as reported in literature as 407.1 cm^{-1} and 374.6 cm^{-1} respectively in *eq. 4*, we obtain quasi *TO* mode at 385.4 cm^{-1} which is very close to the observation at 384.9 cm^{-1} in our study, thus can be associated with the quasi phonon modes nature [30]. Similarly quasi phonon modes nature of *LO* mode is also calculated using the frequencies of $E_1(LO)$ and $A_1(LO)$ modes as 591 cm^{-1} and 579 cm^{-1} and it is found to be at 587 cm^{-1} which is also very close to the observation we see at 587.5 cm^{-1} in our experiment [158][132]. Therefore we have assigned Raman peaks seen at 587.5 cm^{-1} and 385.4 cm^{-1} to be defined as quasi *LO* mode A_1 *(LO)* – E_1 *(LO)* and quasi *TO* mode A_1 *(TO)* – E_1 *(TO)* respectively. We also observe a dominant E_2

(high) mode at 440.5 cm^{-1} which is an allowed mode for the back scattering geometry in our experiment. Another mode at 335.6 cm^{-1} is assigned to E_2 *(high)* – E_2 *(low)* which might be related to second order Raman process as explained by some researchers which needs further investigation [159]. In order to explore the laser irradiation effect on the sample, we varied the laser excitation input and decreased it to 75%, 50%, 25% and 1% as indicated in figure 29. We did not observe any shift in the wavenumber when laser power is decreased thus eliminating the possibility of laser irradiation heating effect on the vibrational modes [101].

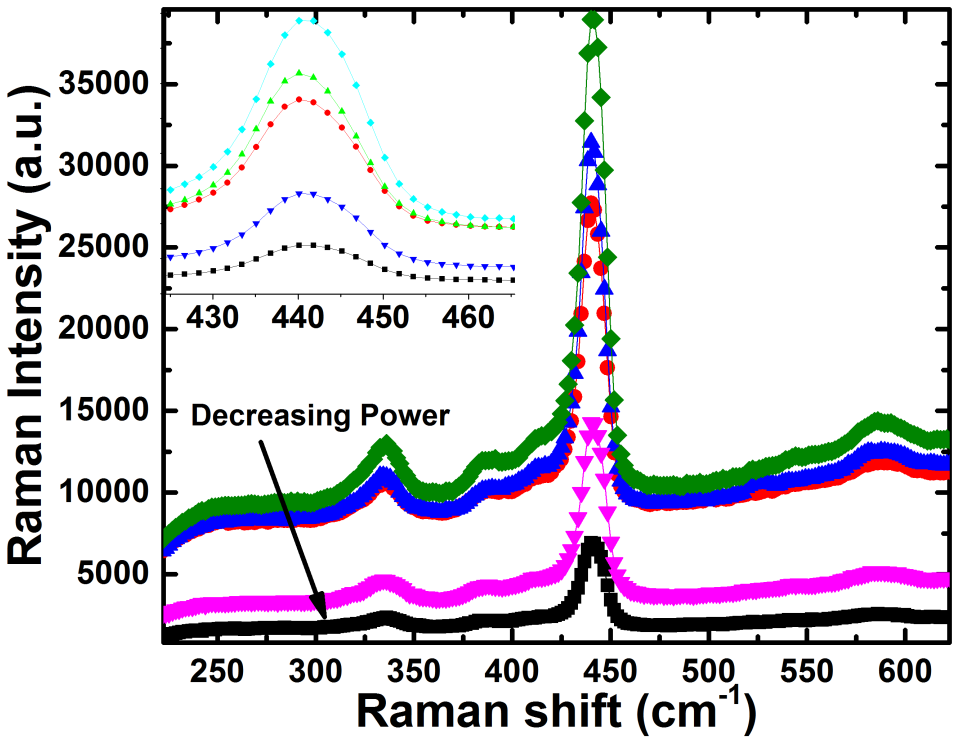

Figure 29: Raman spectrum of ZnO nanowires on decreasing laser excitation power from 100 % (top curve) to 75%, 50%, 25% and 1%.

5.5.2. Raman spectra at varied growth times

We modulated growth times for ZnO nanowires in order to find the most appropriate growth conditions with the help of Raman spectroscopy which appears to be an efficient way to pick the appropriate growth time. In effort to do that, VLS growth was carried out for a duration ranging from 5 mins till 60 mins keeping the temperature and gas flow constant whereas Raman spectra is recorded for each interval. Bare Si spectra is also taken for calibration. Figure 30a indicates Raman spectra for all the ZnO growth durations whereas figure 30b is scaled on the y-axis for more clarity on the spectra. It is seen that for 5 min growth condition, only a small E_2 (high) peak is seen whereas sharp Si peak is seen in the spectra. As the growth time increases, this Si peak coming from the bare substrate decreases and E_2 (high) mode enhance. As growth time reaches to 45 min, E_2 (high) mode becomes the most dominant mode whereas LO and TO modes are also visible. The detailed analysis is already done for this growth condition in the previous section. On increasing the growth time to 60 min, we still see E_2 (high) mode to be the prominent mode but intensity of this peak is less than as for 45 min time. Based on these growth analysis, we choose the growth time to be at 45 min after the temperature is stabilized at 910 ^{o}C for best case scenario.

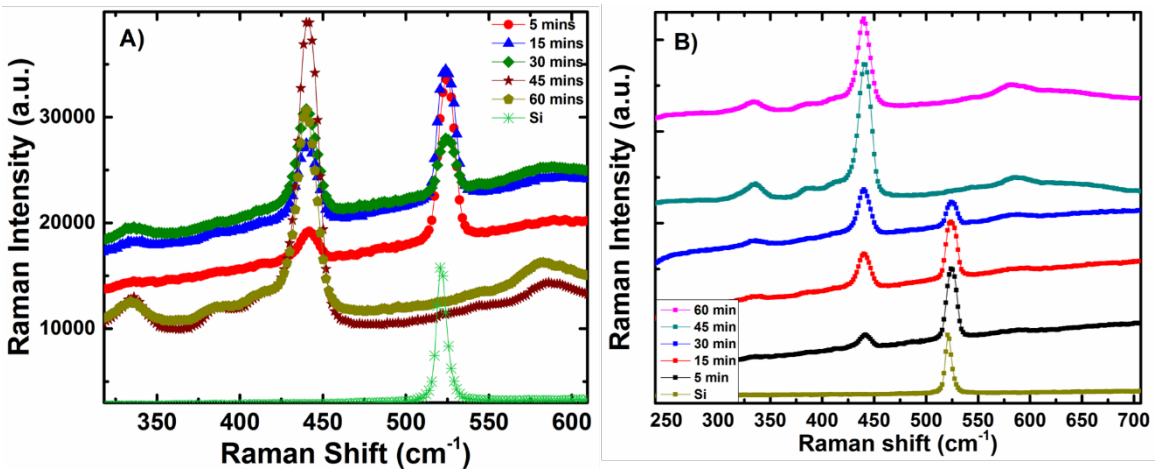

Figure 30: a) Raman spectrum of ZnO nanowires and Si at varied growth times ranging from 5 – 60 min; b) Offset y-axis for clarity.

5.6. Electrostatic force analysis for zinc oxide nanowires and nanostars

5.6.1. Spontaneous Polarization in ZnO

Polar ZnO crystals are generally of three types, wurtzite, zinc blende and the rock salt. Wurtzites are the most stable ones and mostly considered at the ambient conditions. Wurtzite ZnO crystals have electrical polarity and their polarization can be categorized as either induced polarization such as piezoelectric interaction or built-in spontaneous polarization [160]. The piezoelectric polarization occurs due to an external strain that causes the piezoelectric crystal to have a macroscopic polarization as a result of displacement of ions, which has been well researched so far [161]. Unlike piezoelectricity, ZnO also tend to have a built-in spontaneous polarization along the growth axis (c-axis). This built-in spontaneous polarization induces a natural electric field in these crystals that affects device properties significantly. Such an effect can be utilized in many device structures such as bio-nano interfaces or HEMT structures taking advantage of induced electric field from these polar crystals lacking an inversion

symmetry thus opening possibilities in various applications such as nanobiosciences, optoelectronics etc [162-163].

Semiconductor nanoparticles such as ZnO with built-in spontaneous polarization can generate sufficient electric fields that can be utilized for various applications such as voltage gated ion channels, nanobiosciences and optoelectronic devices [162-163]. Considering that wurtzite ZnO have electrical polarity and normally grows along its *c* axis, only *c*-component of the spontaneous polarization exits. For our case of nanowires, we know that the nanowire consists of a unit cell however this is not always the case. If the ZnO crystal consists of a unit cell, its layers along the c-axis should start with Zn atoms and terminate with O or vice versa. However in the case when crystal is terminated by either of Zn or O on top and bottom layers, this implies that we have extra ions in addition to the unit cells. These extra ions or additional charges will change the spontaneous polarization in the crystal. Effects of these charges becomes more dominant when the size of crystal becomes smaller; for example in the case of a quantum dot with nanosized dimensions. Therefore it is very important to estimate the magnitude of electric field due to spontaneous polarization in nanoscale structures. We have observed from our TEM measurements that ZnO nanowire consists of a single crystal (figure 19) whereas *c*-axis of a nanostar is oriented in random directions and so as their dipole moments (DM) (figure 23). This is depicted in schematic as shown in figure 31 (a) and (b) for the case of NW and NS respectively. We have developed a model in our previous study to calculate the strength of electrostatic field produced by ZnO quantum dots [164]. This model becomes complex for the case of nanowires and especially nanostars. We are utilizing the

effects produced due to the spontaneous polarization from ZnO nanowires and nanostars using EFM measurements and mathematical modeling [82].

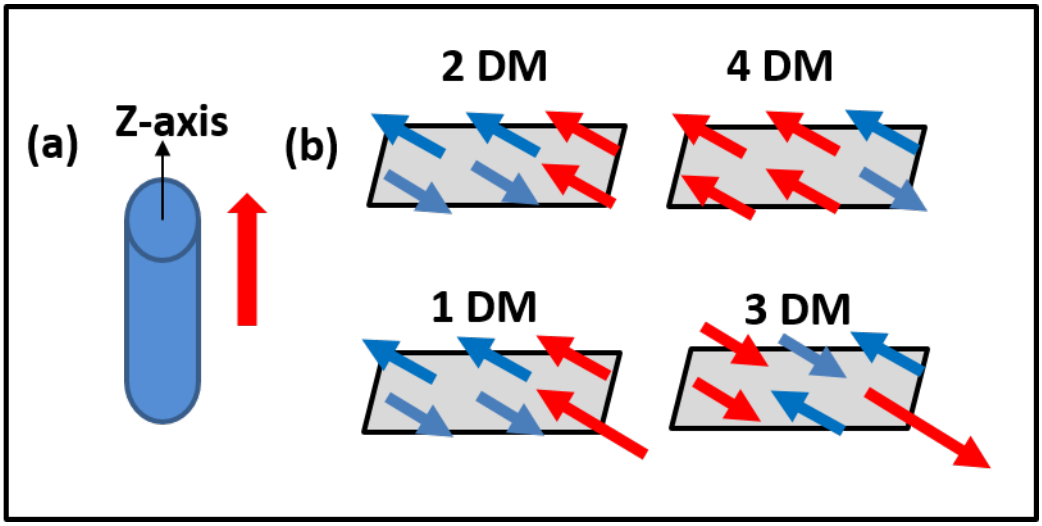

Figure 31: Schematic illustration of (a) growth direction and c-axis for ZnO NW; (b) Different scenarios for the net dipole moments (DM) of random orientations of a ZnO NS [82]

5.6.2. Electric field estimation from Electrostatic Force analysis

For the atomic force microscopy measurements, ZnO NW and NS samples were scratched and drop cast on a gold coated Si substrate to extract a single NW and NS as shown in the SEM images of figure 32.

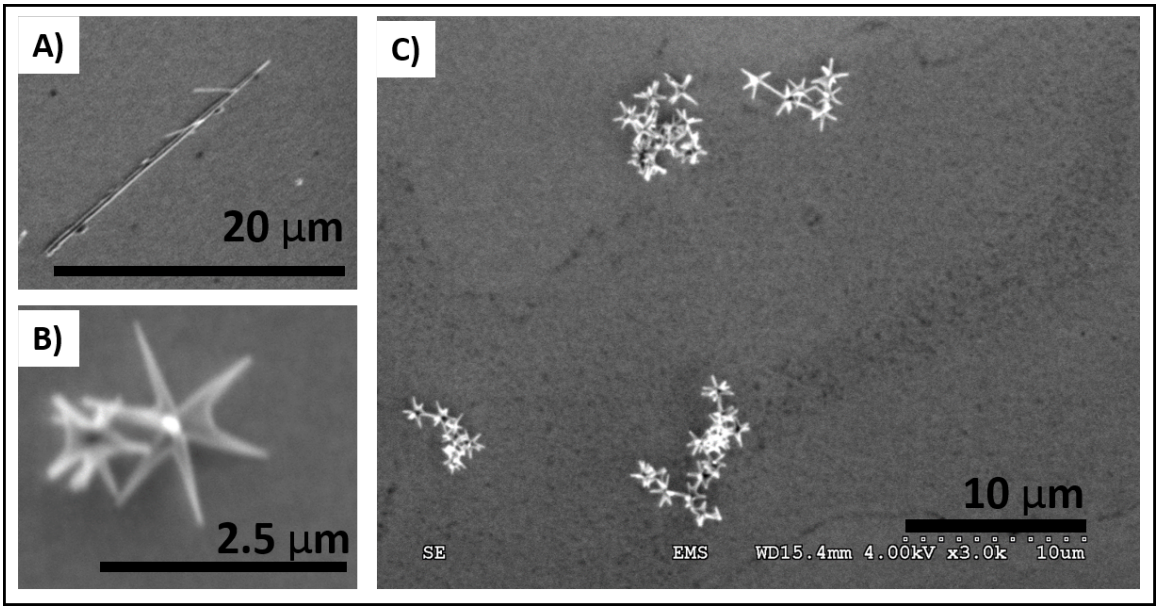

Figure 32: SEM image of a (a) single nanowire; (b)-(c) Nanostar dropped on gold coated substrate after scratching the sample for AFM measurements.

Figure 33 (b)-(c) shows the typical pattern of ZnO NW and NS with corresponding height profiles for selected (dash lined) regions obtained from these samples. Figure 33(a) shows AFM height profile of gold coated Si substrate for reference purposes. It appears that the gold coated Si substrate shown in 1 μm by 1 μm area scan has a height profile ranging from 4- 5 nm. ZnO NWs as shown in figure 33(b) shows height of NWs lying on the substrate to be 50- 100 nm which is close to the diameter of a nanowire whereas NS shows ~ 1 μm of NS height.

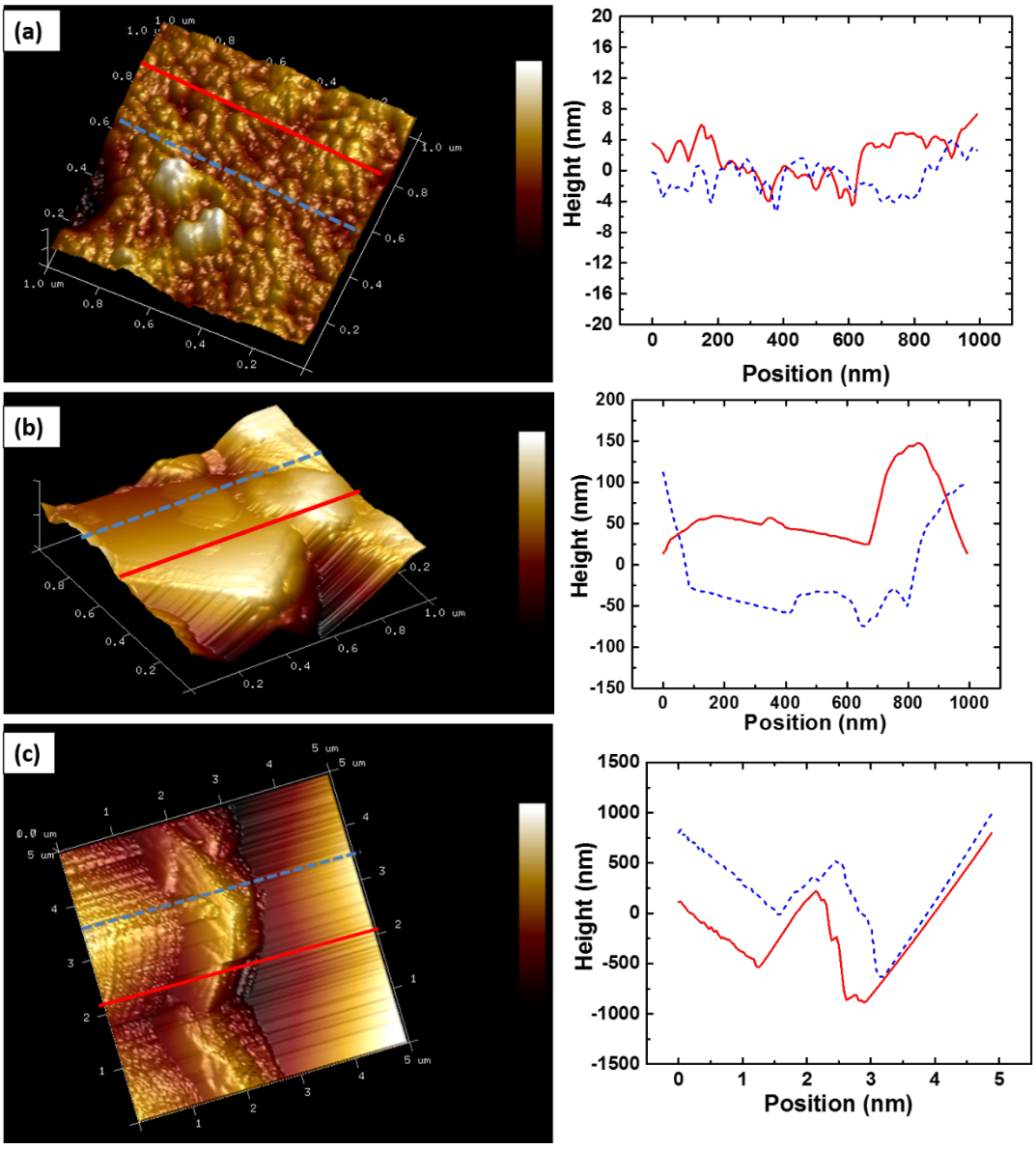

Figure 33: Typical AFM patterns with corresponding height profiles for selected (dashed lined) regions of (a) a gold coated Si substrate (b) ZnO NW; (c) ZnO NS [82]

The EFM measurements are used here to study the electric field produced by ZnO nanostructures due to its built-in spontaneous polarization effects. Using the AFM in the lift mode profile, probe displacement is found that is used to calculate the electrostatic force. Resulting electric field is calculated using the net surface charge of the ZnO NWs

and NSs. Figure 34 shows the EFM pattern with the corresponding probe displacement profiles of the NW and NSs. Lift scan is done for all three samples, it is seen that the sample for Si+Au substrate (figure 34a) do not attract the probe and their interleave amplitude is in 50 - 100 picometer range (figure 34b) as indicated by the two marked regions in (figure 34a) which means that the regions are without any electrostatic force. EFM pattern for ZnO NWs is shown in figure 34c with multiple regions scanned for estimating the interleave amplitude profile for comparison. We first scanned a ZnO NW region a (red circled areas) that shows huge attraction for the probe as seen by the large change in interleave amplitude scan (figure 34d) ranging from 10 - 15 nm range. For comparison, we scanned region b with no nanowire that does not show any change in interleave amplitude confirming that the attraction of the probe is from the spontaneous polarization induced electric field from ZnO nanowire. Figure 34e shows EFM pattern from NSs. We saw attractions from two different places of region c of the magnitude of ~ 25 - 40 nm (figure 34f). We performed SEM measurements on them and figured out the larger lift height areas are the ones with multiple nanostars clustered together whereas smaller area indicate a single NW however both cases clearly exhibit strong electrostatic force attractions.

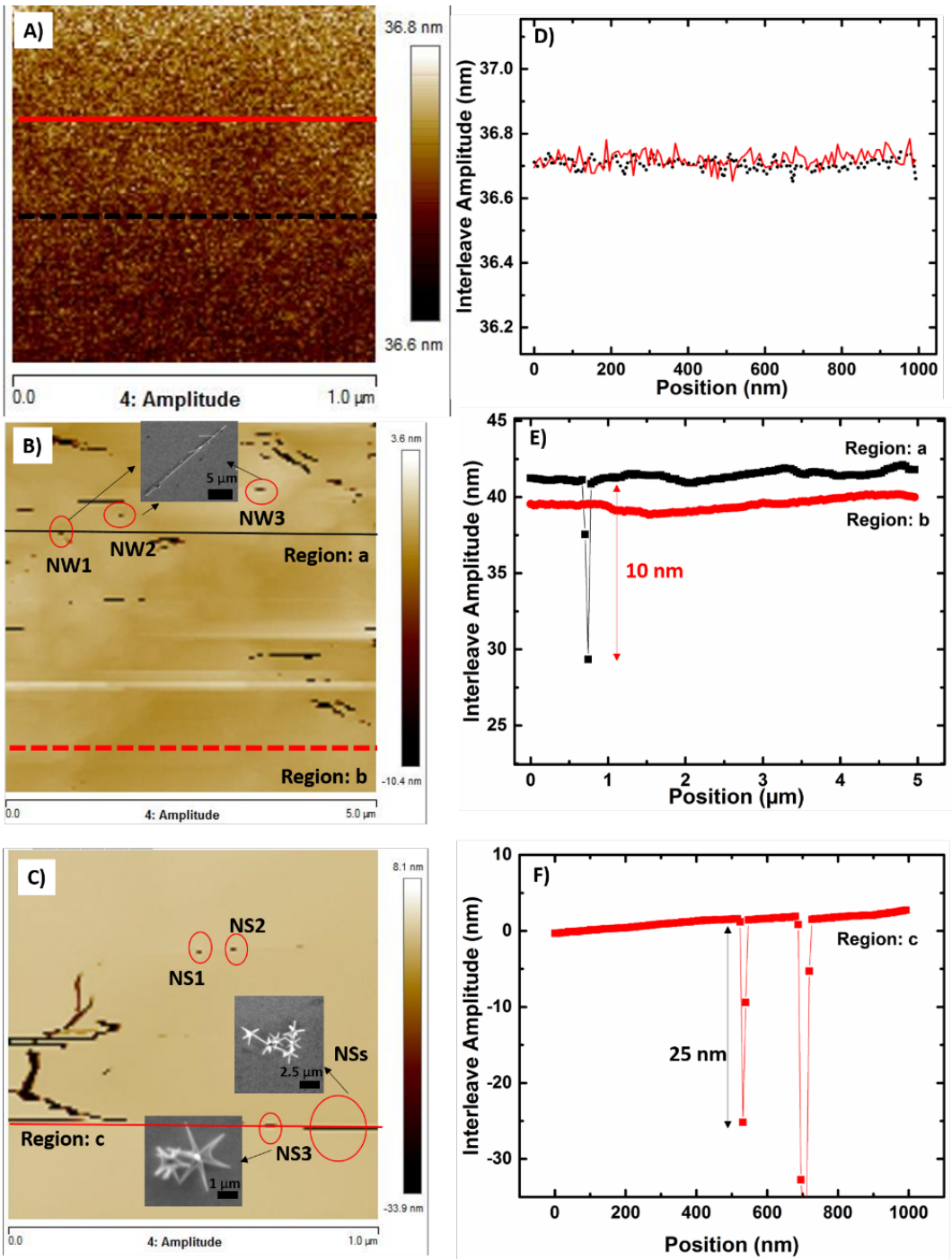

Figure 34: a) Interleave amplitude for Si and gold coated substrate for reference; b) Interleave amplitude for ZnO NW with red solid circles indicating areas of NWs, subset indicates SEM image of a single NW; c) Interleave amplitude for ZnO NS with small red solid circles indicating single NS areas while bigger red circle indicating multiple stars as shown by SEM images in subsets; (d)-(f) Displacement profile images for the Si+Au substrate, NW and NSs respectively whereas dashed and solid lines in (a)-(c) indicate areas scanned for displacement profiles

Numerical analysis is done using Lorentz's law as shown by the following equation:

$$F = qE,$$

where F is the electrostatic force, q is the charge, and E is the electric field.

Our AFM probe has the spring constant of 2.8 N/m, the corresponding force calculated from Lorentz law to the 10 nm and 25 nm displacements are 28 and 70 nN. Further exposed surface areas for the NW and NS are calculated considering nanowires as a cylinder with surface area of $\pi r^2 + 2\pi rL$. Length of a nanowire is taken as 5 μm whereas length of a star arm is taken as 1 μm. However for the case of nanostar with six arms, effective surface area with three different cases of orientation dependence is considered. As seen in the TEM image of ZnO stars in figure 23, we see random orientations of the preferred c-axis of nanostar. We have simplified the case and assumed three different cases of overall polarization effect. This includes effective dipole moments due to two, three and four arms of the stars while considering rest of the dipoles cancel the effects of each other as depicted schematically in figure 31. In that case, effective area for all three different cases of star is considered separately and net electric field is calculated.

In order to estimate the charge, it is important to consider the capacitance between the tip and the surface as well. Using a simplified parallel plate capacitor model, capacitance(C) can be expressed as $C = \epsilon_o \epsilon_r \frac{A}{d}$, where ϵ_o= 8.85 x 10^{-12} F/m as the vacuum permittivity and ϵ_r = 8.91 as the permittivity of ZnO. With a 0.3 V electric potential applied during EFM measurements, charge is estimated using $Q = CV$. The

amplitude of the electric field is thus calculated by $E = \frac{F}{q}$ and turns out to be on the order of 10^7 V/m for nanowire and in the range of 1.5 x 10^8 – 4.6 x 10^8 V/m for nanostars.

5.7. Conclusions

Growth conditions of ZnO nanowires is evaluated, discussed and optimized. As grown ultra- long single crystal zinc oxide nanowires have been grown in appropriate growth conditions whereas decreasing substrate temperature results in star-like complex ZnO nanostructures. As grown ZnO nanowires shows near band edge emission as well as strong green emission that is related to intrinsic dopants. Large concentrations of intrinsic dopants can cause high conductivity in the device that can be used in sensing applications. Nanostars show enhanced UV emission and less intrinsic defects. Diameter dependent studies of zinc oxide nanowires reveals lower concentration of surface states for thicker nanowires. Results from anneal induced effects shows decrease in UV as well as green emission which is attributed to expanded depletion region causing decrease in oxygen vacancies within ZnO nanowires. Raman studies of randomly oriented nanowires under appropriate growth conditions shows quasi phonon modes nature of the vibrational modes whereas Raman studies on modulating growth times helped choosing best growth conditions for the VLS growth of ZnO nanowires. Measurements of the electrostatic force analysis due to the spontaneous polarization of ZnO NWs and NSs are done and the orientation dependence is taken into account to quantify built-in electric fields from ZnO NWs and NSs which may be pursed in future research.

6. INDIUM INCORPORATED ZINC OXIDE NANOWIRES

Indium-doped zinc oxide nanowires grown by vapor-liquid-solid technique with 1.6 at. % indium content show intense room temperature photoluminescence that is red shifted to 20 meV from band edge emission of zinc oxide. We report on a combination of nanowires and nanobelts-like structures with enhanced optical properties after indium doping. The near band edge (NBE) emission shift gives an estimate for the carrier density as high as 5.5 x 10^{19} cm^{-3} for doped nanowires according to Mott's critical density theory. Quenching of the visible green peak is seen for doped nanostructures indicating lesser oxygen vacancies and improved quality. Photoluminescence (PL) and Transmission Electron Microscopy (TEM) measurements confirm indium doping into the ZnO lattice whereas temperature dependent PL data gives an estimation of the donor and acceptor binding energies that agrees well with indium doped nanowires. This provides a non-destructive technique to estimate doping for 1-D structures as compared to the traditional FET approach. Furthermore, indium content is varied from 3-11 wt. % and their photoluminescence properties and transmittance characteristics are explored. These indium doped nanowires can be a potential candidate for transparent conducting oxides (TCO) applications and spintronic devices with controlled growth mechanism. This work is reproduced from my published article as cited in [86].

6.1. Background on Indium doped zinc oxide nanostructures

The greatest challenge in realizing photonic devices based on zinc oxide based nanowires is heterostructures, doping, and band gap engineering [165]. Doping in semiconductor materials with selective elements significantly alter optical, electrical and

magnetic properties which is indeed very critical and important for device applications [166]. Doping controls and manipulates semiconductor properties and thus plays a key role in nanotechnology and nanosciences. Properties of ZnO can "magically alter" when doped with semiconductors or transition metals. ZnO band gap energy can also be tuned by substituting divalent onto cation sites in order to produce heterostructures.

ZnO has a band gap of 3.37 eV at room temperature. Group III elements like *Ga*, *Al* and *In* can be used as an *n*-type dopant whereas group V elements like *Sb, As, P* and *N* are candidates for *p*-type doping in ZnO [167]. Although *p*- type doping in ZnO still remains a challenge, it is equally important to achieve *n*-type doping in ZnO with controllable carrier concentrations and high crystallinity that can be used for optoelectronic and spintronic applications [168]. Furthermore, if we need to alter the bandgap of ZnO that could result in expanding or shrinking of band gap, band gap engineering needs to be done by introducing alloys to ZnO which will also be discussed in this chapter. Band gap engineering of semiconductor materials is an important strategy for custom tuning the physical properties of these materials in optoelectronic devices. The fundamental band gap energy of zinc oxide based alloys can be increased from 3.37 eV to ~ 4.0 eV or can be decreased to ~3.0 eV by doping .

From group III elements, most of the research has been done using Aluminum as a dopant. One of the main reasons for this being the ionic radius of Aluminum is much smaller than that of Indium and Gallium. However considering the thermodynamic data, it is revealed that the free energy for the formation of Al_2O_3 is lower as compared to zinc oxide suggesting that aluminum oxide has significantly higher reactivity with oxygen [169]. In this scenario, indium possesses greater resistivity to oxidation along with less

reactivity as compared to *Al* making it a suitable and attractive dopant for fabricating *n-type* ZnO. Indium is one of the candidates of interest in zinc oxide because it can efficiently improve the optoelectronic properties of ZnO. In_2O_3 is a metal oxide semiconductor with a wide band gap of 3.6 eV. So far few researchers have tried to fabricate indium doped ZnO thin films and investigated their electrical and structural properties of fabricated films [170-171]. Some studies have also reported *n*-type conducting ZnO nanowires using pulsed laser or thermal evaporation techniques but most of them reported structural or room temperature PL studies [172]. There are only a few reports on temperature dependent PL studies on indium doped ZnO nanowires [167][173-174] Amongst them, Chen *et al.* [173] prepared *ZnO:In* nanorods by sol-gel technique, Morales *et al.* [167] synthesized indium doped nanostructures using chemical synthesis technique whereas Liu *et al.* [174] reported temperature dependent studies of In doped ZnO nanowires grown on sapphire substrates. In this study, S. Farid *et al*. [86] used a vapor-liquid-solid (VLS) growth technique to dope 1D ZnO nanostructures on silicon substrates for better control, optimization and cheaper solution and explored optical and structural properties. Along with this, we have also performed a deep defect state analysis of doped ZnO NWs using temperature dependent PL studies since that can provide useful information on the dissociation processes due to the impurity bound excitons. Further we have tuned the room temperature photoluminescence spectra of the indium incorporated ZnO nanowires while adjusting the In_2O_3 concentration and explored its transmittance properties. We have achieved enhanced optical properties from In doped ZnO NWs (IZO) [86] owing it to be a good candidate for future spintronic devices, transparent conducting oxide materials, photodetectors and gas sensors applications [174-175].

6.2. Experimental

Synthesis of Indium incorporated ZnO nanostructures was carried out using a vapor transport process in a single zone tube furnace using VLS growth method. ZnO (99.99%, Sigma Aldrich) and graphite powder (99.9%, Sigma Aldrich) are mixed together first in a weight ratio of 1:1. In_2O_3 (99.99%, Sigma Aldrich) is then added as a reaction source to the ZnO mixture at a weight ratio of 3% ZnO and mixed together thoroughly in a centrifugal speed mixer at 1000 rpm for uniform distribution of powder. The mixture was then placed in the ceramic boat and placed in the middle of the 2 inch quartz tube in the furnace. This boat was positioned in the center of the quartz furnace tube and the Si substrate with <100> crystal orientation coated with 4 nm gold was placed 2 cm downstream from the mixed powders. The growth was carried out at 910 ^oC for ~40 min duration at 150 sccm at that temperature and then allowed it to cool at room temperature before taking the substrates out of the furnace. Structure was characterized using a variable-pressure Hitachi S-3000N scanning electron microscope (SEM). Optical properties are investigated using photoluminescence spectroscopy at room temperature with a 325 nm He-Cd laser using an Acton 2500i spectrometer while low temperature PL investigation is done in a closed cycle helium cryostat. Optical transmittance measurements were carried out using UV-VIS spectrophotometer. TEM is used to observe the crystal structures and diffraction patterns for the doped ZnO structures using JEOL JEM 3010 electron microscope.

6.3. Results and Discussions

6.3.1. Structural Analysis of Indium doped ZnO NWs

Figure 35(a) shows SEM image of as-grown ZnO NWs and indium doped ZnO (IZO) NWs side by side for comparison. It can be seen that the Si substrate is covered with tangled ZnO nanowires with diameters of 50-100 nm and lengths up to 10-50 μm. In case of IZO samples, along with nanowires, we observe a few nanobelts (NBs) dispersing in nanowires. Fig. 35(b) – (d) shows indium doped NWs and NBs at different magnifications. Diameters of doped NWs are in the range of 100-200 nm whereas NBs reveal widths up to 500 nm and thickness ~ 20nm. Some of the NBs appear to be smooth along their lengths while some shows a zig zag structure.

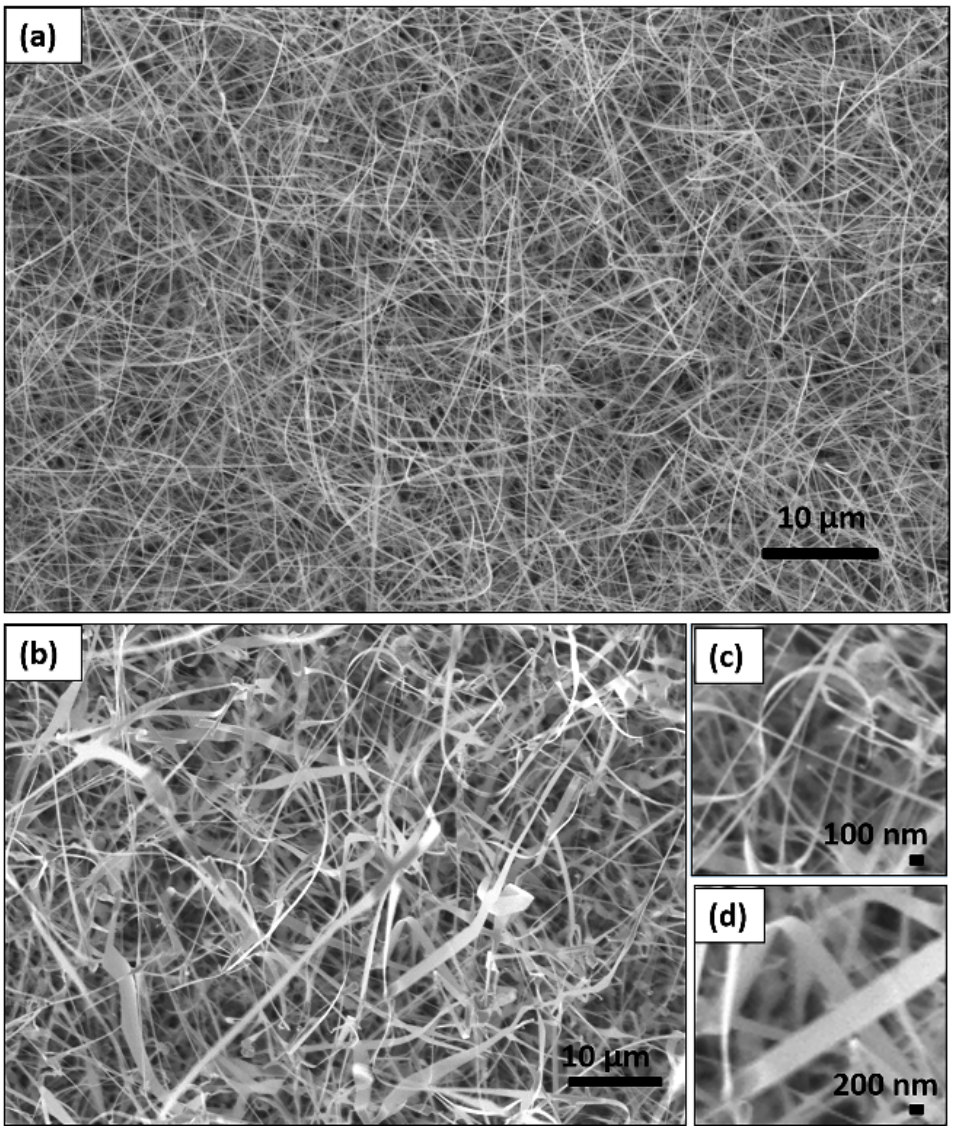

Figure 35: SEM image of a) ZnO NWs; b) IZO NWs and NBs; c) IZO NWs with ~50-100 nm diameter; d) IZO NBs with ~500 nm diameter.

For obtaining more insight into individual nanowires and nanobelts of doped ZnO structures, HRTEM, SAED and EDX measurements have been carried and the results are shown in figure 36 (a) – (f). We did not observe any lattice distortions, stacking faults or evidence of amorphous outer layer from the TEM profile. For doped NWs, the hexagonal

lattice fringes are spaced ~ 2.94±0.01 A^o apart (figure. 36(a)) which is slightly greater than the as-grown ZnO lattice spacing of ~ 2.83±0.01 A^o (figure 36(b)). A possible reason for the increase in *d* spacing could be doping related as indium ionic radius is higher than ZnO that accounts for variation in lattice spacing [176]. This variation in *d* spacing could not be explained by the TEM measurement's error bar, which is less than 0.01 A^o. SAED measurement is performed to confirm the crystal structure of doped NWs (figure 36(c)). Hexagonal diffraction pattern are consistent with the wurtzite structure with single crystalline properties. From these measurements, we can also reveal that the doped NWs are grown along [0001] direction. EDX measurements have also been made on many doped ZnO structures and *In* peak is found in most of them (figure 36(f)). The atomic percentage estimated from EDX for IZO nanowires is ~ 1.6%. We also observed some of the NBs seems to be non-uniform through its length as shown in figure 36(d).

In order to investigate further into the possible reasons for the structural change from the thinner NWs to larger diameter of nanowires and nanobelts with increasing the concentration of Indium, an understanding of the possible growth process is necessary. An important factor to consider is the surface energy that affects the growth of nanowires and determines the necessary controlled nucleation growth conditions. For our case, indium content is much lower than the zinc content, zinc and indium are transported to the substrate at elevated temperature. These vapors further react with *Au* and gives rise to a *Au-In-Zn* ternary phase. Since the surface free energy is defined as the free excess surface energy per unit area for a particular crystal geometry and face, a certain strain resulting from ternary *Au-In-Zn* phase gives rise to variations of surface free energy that disturbs the equilibrium crystal shape and modifies the nucleation behavior of zinc oxide

resulting in nanobelts formation. Similar observation of a ternary *Au-Zn-In* phase has been observed by Fan *et al*. [189]. As for the non-uniform belts, it might be due to some thermal instability or strain during the liquid-solid interface phase for the VLS growth mechanism that can also explain the possible cause for the wider diameters of the nanowires for the *In* doped ZnO structures.

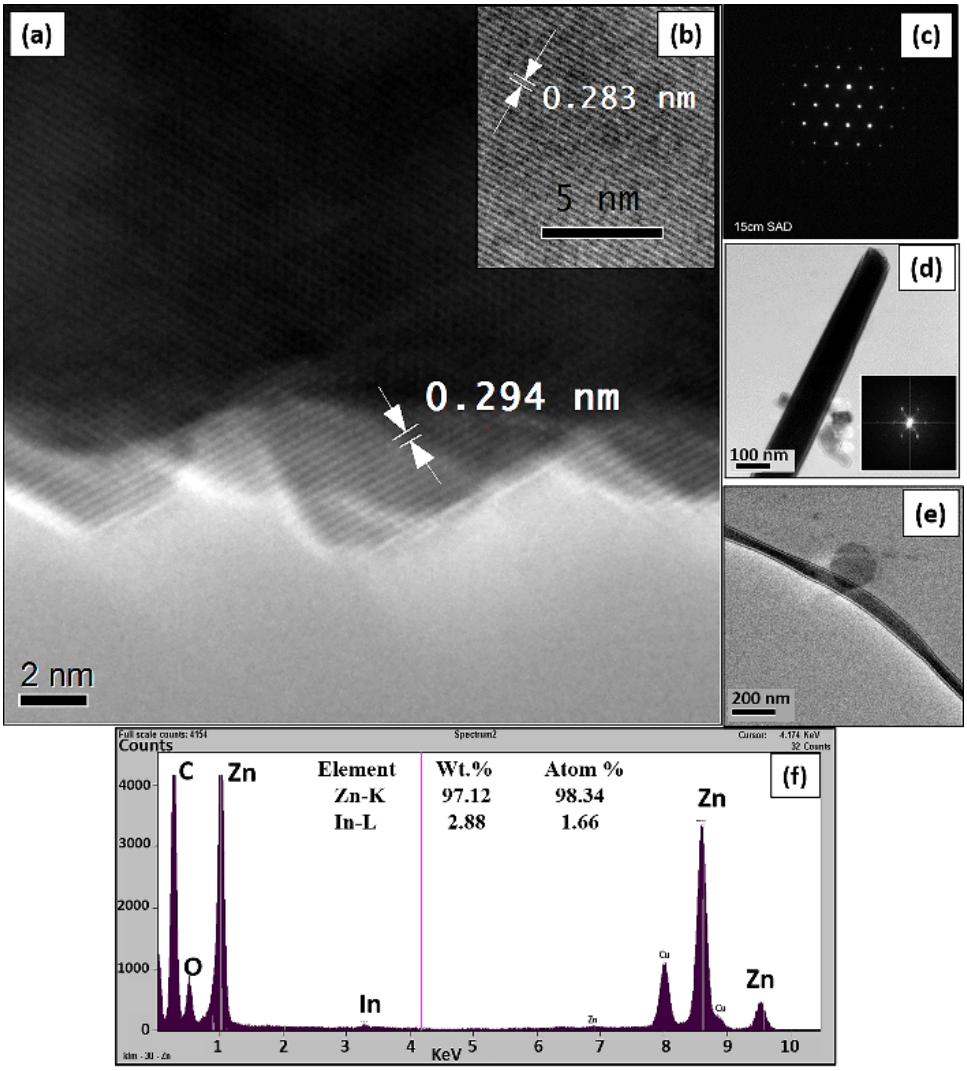

Figure 36: a) TEM image of IZO nanowires showing lattice spacing of 0.294 nm; b) TEM image of undoped ZnO nanowires with 0.283 nm lattice spacing; c) SAED pattern for indium doped zinc oxide nanostructures; d) TEM image of 100 nm IZO NW (inset shows Fast Fourier transform measurements for IZO nanostructures); e) TEM image of a non-uniform IZO NB; f) EDX profile for obtaining elemental composition of IZO nanostructures

6.3.2. Defect State analysis of Indium doped ZnO NWs

Figure 37(a) shows the PL spectra of ZnO and IZO NWs at room temperature together for comparison. As it can be seen that the undoped ZnO NWs shows weak near-band-edge (NBE) emission at 3.25 eV (381.5 nm) while broad strong visible emission (VE) at 2.45 eV due to deep level defect states often related to oxygen vacancies is seen which has been extensively studied in the past decade [177-178]. Interestingly, after *In* doping, we see a strong enhancement in NBE peak which is almost 20 times stronger than pure ZnO nanowires while VE is decreased significantly owing to change in the growth kinetics due to *In* supply which helps to reduce the number of defects states resulting in improved crystal quality. Along with enhancement in NBE peak, we also observe a red shift in energy to 3.23 eV (383.9 nm) as observed by other researchers [179-180] as well due to *In* doping in GaN and GaAs based thin-films and nanostructures. Such a red shift could be a result of potential fluctuation induced by the introduction of impurity atoms resulting in optical band gap narrowing of nanostructures [176]. Also according to Motts critical density theory, band gap tends to increase if the impurity is kept under Motts critical density limit. After the conduction band is already filled and more impurity atoms are added to the semiconductor, merging of conduction and donor band levels happen and the band gap tends to decrease [181]. Based on the calculations presented by Kim *et al.* [182], we estimate the carrier concentration for our indium doped nanowires to be ~ 5.5 x 10^{19} cm^{-3}.

The reason for an enhanced NBE peak could be explained in two different ways; either this effect is due to the lower concentrations of surface states in thicker doped NWs diameters that can be explained by the lesser surface to volume ratio as compared to their

undoped thinner counterparts or it is also expected that the formation of bound electrons in the indium doped samples is enhanced that resulted in strong NBE peak [183]. Morales *et al.* [167] also observed 10 times enhancement from indium doped samples which is suggested to be a transition from a shallow defect state and a deep level.

We explored this effect in detail at low temperature PL spectra and found a clear difference in the PL spectra of doped and undoped nanowires at 20K as shown in figure 37(b). For undoped ZnO NWs, the dominant peak is seen at 3.351 eV attributed to the bound exciton emission peak, likely originating from D^oX. A small peak at the high energy side of D^oX (3.358 eV) is contributed to the surface bound excitons (SX) that completely disappears at higher temperatures (shown later in figure 39(a)). We also observe an emission at 3.31 eV which is attributed to donor-acceptor pair (DAP) recombination and matches well with others in literature [184-185]. Another weak broad band at 3.07 eV is seen which becomes significant for *In* doped NWs. We did not see this peak for doped nanowires in previous efforts [173-174] and its origin is still under investigation. This peak may be associated with the phonon replicas of free excitons in case it falls into the LO phonon replicas of ZnO (~72 meV) which is hard to extract from our results due to the broadened and smeared nature of the peak or purely related to *In* doping effect. After *In* doping, the PL spectra at 20K indicates some different features compared to pure ZnO NWs. This PL spectra can be well fitted by five Gaussian peaks as shown in Fig. 39 (b). We found that D^oX happens at 3.34 eV instead of 3.357 eV which is generally documented for doped indium films indicating that we have achieved heavily doped ZnO nanowires with 1.6 at.% indium content [173]. A similar observation is seen by He *et al.* [184] who confirmed 3.346 eV emission obtained for 1.4 at.% indium doping

due to exciton bound to *In* site confirming that *In* atoms have been doped into the ZnO lattice. We did not observe any SX emission for doped NWs. Intensity of DAP also increases with a small shift towards the lower energy side which is believed to be due to increased bound exciton formation due to *In* doping [167][186]. We also observe another emission band at 3.23 eV which was not seen for undoped NWs. We assign this peak to be LO phonon replica of DAP recombination as it has an energy ~ 70 meV lower than DAP [186]. In order to further investigate and verify our assignments, temperature dependent PL experiments were carried out.

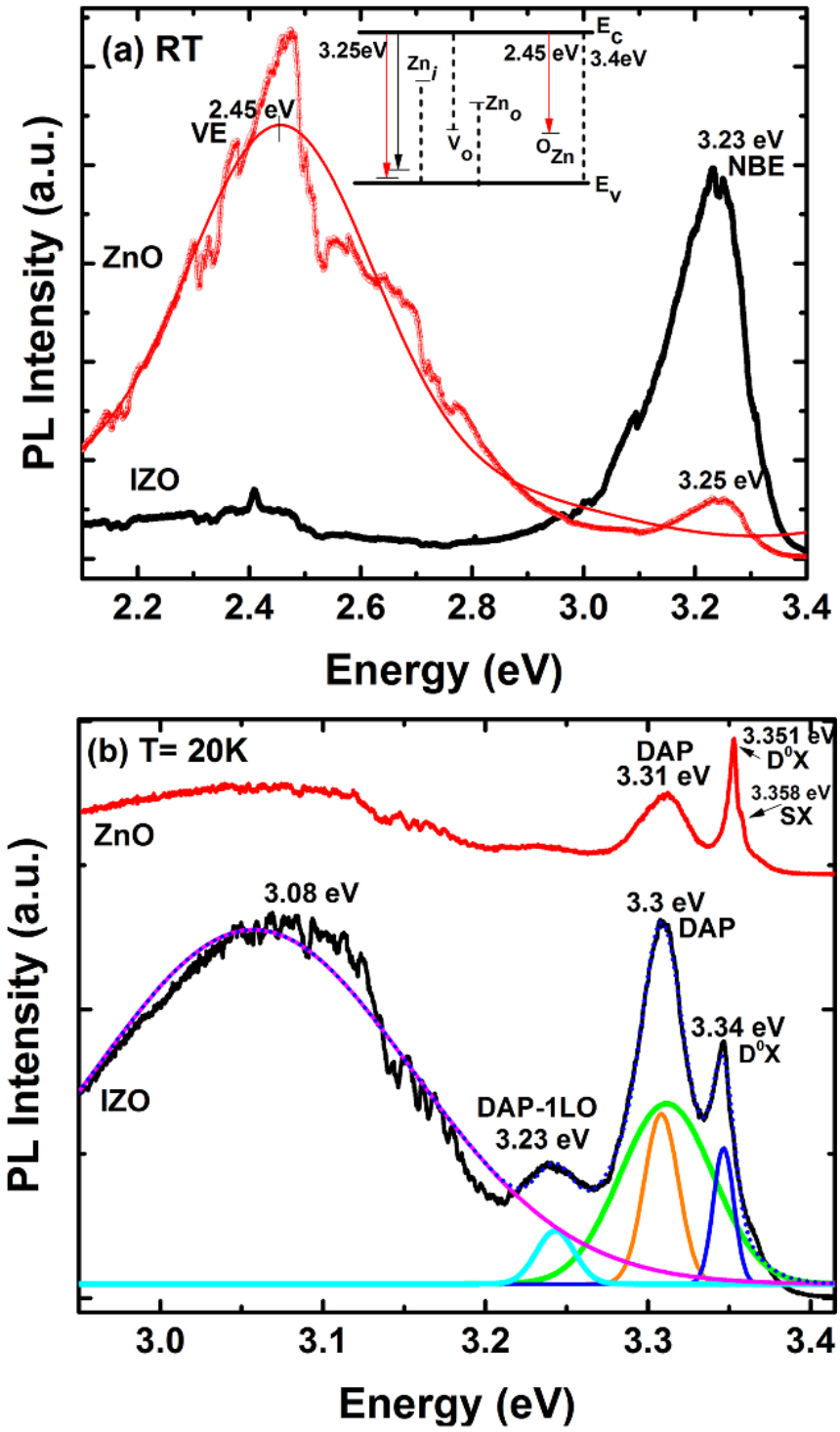

Figure 37: a) Room temperature (RT) PL spectra for the ZnO & IZO NWS; ZnO VE is fitted with Gaussian fit to account for peak variances; Inset indicates schematic of possible transitions from ZnO structures, (NBE emission at 3.25 eV, oxygen antisite (O_{Zn}), oxygen vacancies (V_o) or Zinc vacancies (Zn_o), Zinc antisites in the oxide (Zn_i)); b) PL spectra at 20K for ZnO & IZO NWs with Gaussian peak fits presented for IZO nanowires.

4.

Figures 38 (a) & (b) show temperature dependent PL of ZnO and IZO, respectively. For ZnO NWs (figure 38a), the intensity of D^0X and DAP decreased significantly as the temperature increases and a shift in lower energy side is observed. The SX emission disappears completely at >30K temperature as shown in the inset of figure 38a confirming our assignment related to surface excitons. D^0X emission attenuated and merged into DAP which is reasonable as the free excitons thermalizes and are unable to be seen at higher temperatures. Since the curves at each temperatures have been offset with respect to each other for more visibility, the emissions at higher temperature appears to be less visible. For *In* doped NWs, we did not see any SX emission at all which agrees with Liu *et al*. [173]. With increasing temperatures, the peaks overlap with each other and ultimately shift and merge to a broader peak possibly due to the phonon scattering effects as the temperature reaches to higher orders. Taking a close look at DAP, it is seen that it is broader as compared to D^0X line. We did a quantitative evaluation of the temperature dependence of DAP transition intensities as presented in the inset of figure 38b. The dotted squares presents experimental data and curve is fitted by well known Arrhenius equation using the following formula [9]

$$I(T) = \frac{I_0}{1+A_1 \exp\left(-\frac{E_1}{K_B T}\right)+A_2 \exp\left(-\frac{E_2}{K_B T}\right)} \qquad (1)$$

Here $I(T)$and I_0 are the PL intensities at temperature T and 20K respectively; E_i is the activation energy, K_B is the Boltzmann constant, and A_i is the constant. By making A_2 zero and considering there is only one quenching channel contributing to decrease in intensity of DAP with temperature, we are not able to obtain the best fit curve for the

data. By using a two channel fit and considering both A_1 and A_2 constants, we found E_1 and E_2 to be 32 meV and 9 meV respectively. We suggest that the small activation energy corresponds to the effective ionization energy for the donors whereas acceptor like states is activated at 32 meV. Recent experimental and theoretical results have shown that for *n* type doped ZnO, acceptor like complexes can act as a compensating center [184, 187-188]. This allows us to conclude that the direct transitions between the tails of valence and conductions bands accounts for the remarkable PL intensity for indium doped IZO nanowires [184].

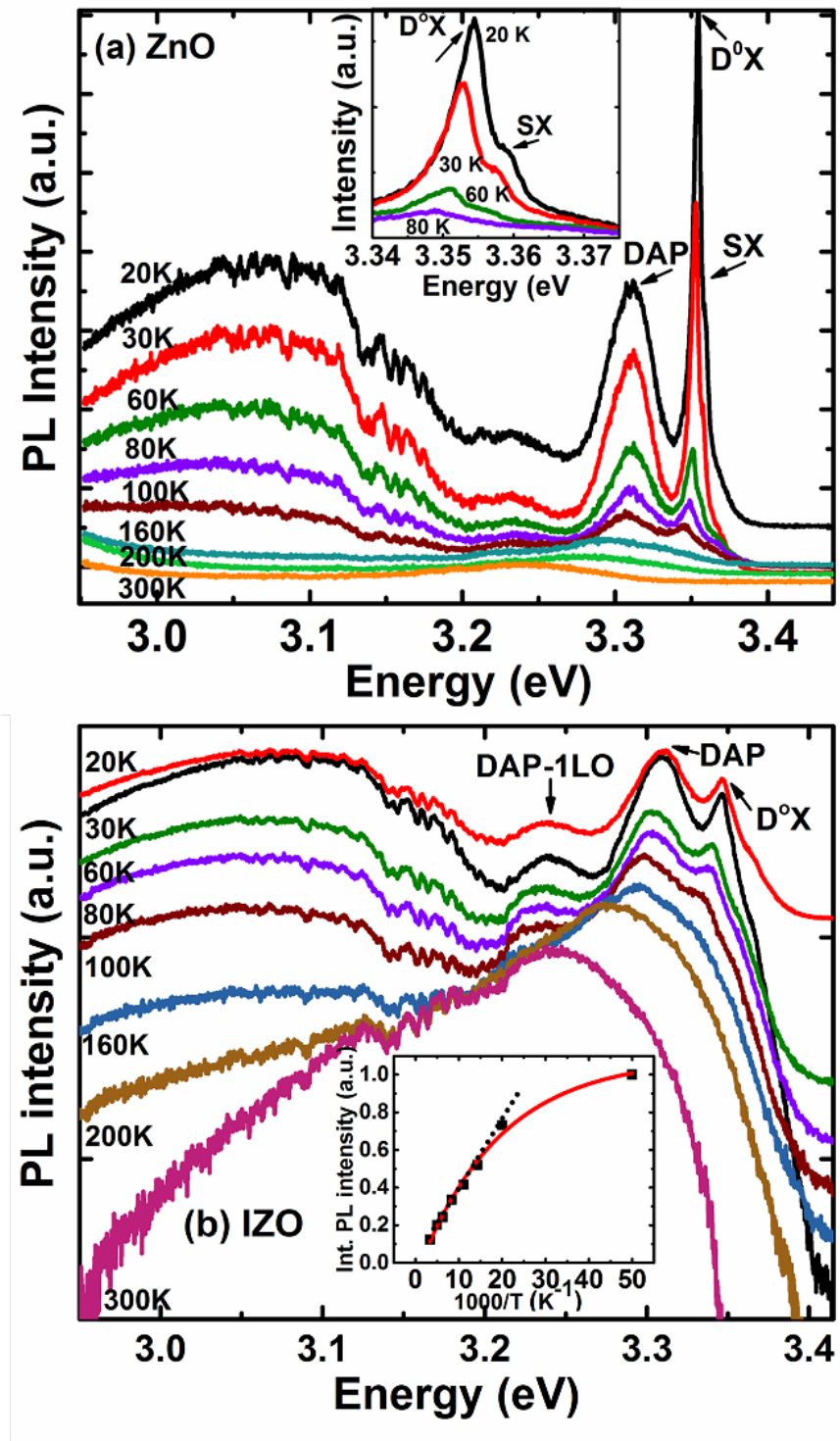

Figure 38: a) Temperature dependent PL spectra of a) ZnO; b) IZO NWs (The inset shows temperature dependence of DAP on PL intensities)

6.3.3. Effect of indium doping Concentration variations

In order to explore more on the impacts of varying indium oxide doping concentration, we varied the concentration from 3% - 15% (wt.) and characterized their optical properties. PL results as indicated in figure 39a reveals that increasing the doping concentration from 0- 7% shift the ZnO band gap from 382 nm to 390 nm pushing it more towards the visible region boundary. On increasing the dopant concentration to 11%, band gap narrows even more (figure 39b). Pushing the dopant limit to 15% does not reduce the band gap further rather slight increase in band gap is observed and the UV peak is reduced significantly. These observations can be explained as when the dopant concentration is low, In_2O_3 tends to act as a dopant in ZnO resulting in no significant change in bandgap, increasing the concentration to higher values tends to form Indium-zinc-oxide alloys resulting in shifting of wavelength more towards edge of visible region. Increasing the concentration further to 15% tends to segregate the dopants in the nanowire boundaries thus resulting in stress due to difference in the ionic size between the dopant and the zinc oxide.

Also according to Motts critical density theory as explained earlier, band gap tends to increase if the impurity is kept under Motts critical density limit. When more impurity is added into the semiconductor, band gap tends to decrease. We observe an increase in band gap on increasing the dopant concentration. This is seen for concentration until 11% but this bandgap starts to move back for concentrations upto 15% until which we tried experimentally and quenching of UV peak is also seen. This possible effect could be due to the segregation of Indium rich domains present within the doped nano crystals.

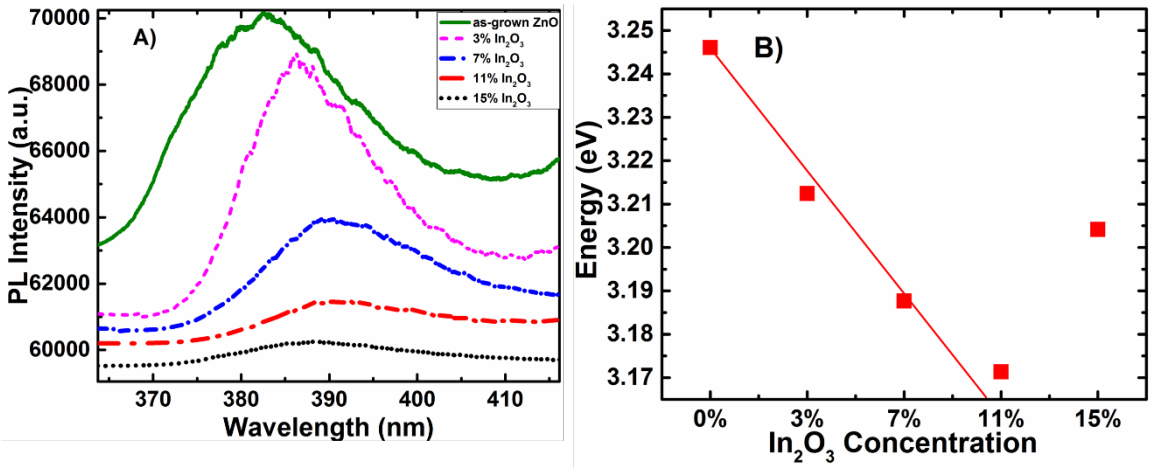

Figure 39: a) Photoluminescence spectra for the 3% - 15% wt. indium doped ZnO nano structures; b) Plot of photon energy on variation of indium oxide concentration in ZnO.

6.3.4 Zinc-indium oxide as a promising candidate of TCO

Another application of ZnO which has not been paid much attention to is the use of ZnO as an alternative candidate for transparent conductive oxide films other than indium tin oxide or tin oxide materials. The electrical conductivity of pure ZnO is mainly due to the extrinsic and intrinsic defects occurring dominantly due to oxygen vacancies or excess of zinc at interstitial positions. Absorption of oxygen in ZnO seems to reduce the conductivity due to its sensitivity to oxidation. Extended lifetimes and minimum power consumptions of display panels such as plasma display's, liquid crystal displays and other optoelectronics devices could not have been possible without achieving lower resistivity and higher transmittance for the TCO films [189]. So far most of the TCO films used in these applications are composed of compound called ITO [190]. Fewer studies have been done using zinc oxide thin films structures as a candidate for TCO. Focusing on this

background, we have attempted to achieve doped zinc oxide nanowires by introducing indium doping that can be used in optoelectronics applications.

Doped and undoped zinc oxide nanowires were transferred onto glass substrates for a transmittance measurements on these samples. Samples were scratched from the silicon substrates and drop casted onto glass substrates using iso propanol as the solvent material and let it dry at room temperature. Optical transmittance measurements were carried out using UV-VIS spectrophotometer. The optical transmittance spectra of doped and undoped ZnO is presented ranging from 200 to 900 nm wavelengths as shown in figure 40. The transmittance of the films doped with 3% and 7% indium oxide are higher as compared to 11% and 15% dopant. In particular, transmittance of the films doped with 3% and 7% doping concentrations was greater than 90% for wavelengths greater than ~400nm till the edge of IR region. Transmittance decreases for higher concentrations of dopants and appear to be even lower than undoped films. This might be due to increase in optical scattering due to segregation caused by increasing dopants or rough surface morphology.

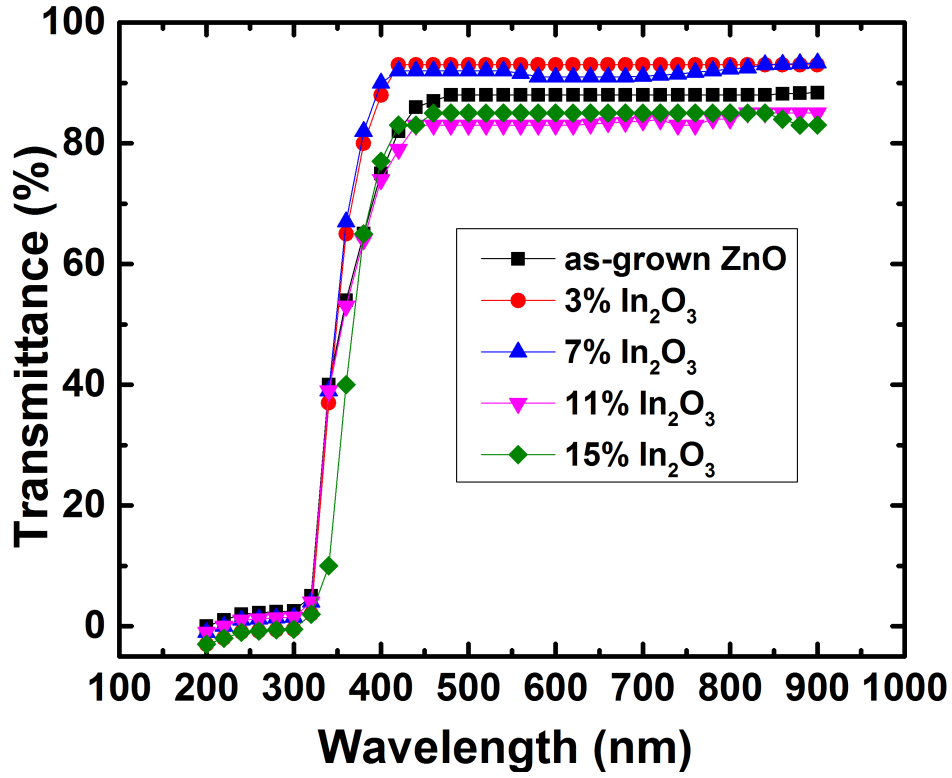

Figure 40: Optical transmittance data for doped and undoped doped zinc oxide nanostructures.

6.4. Conclusions

In summary, we have achieved an intense NBE peak in ZnO NWs after doping it with 1.6 at.% In content. SEM images reveal the formation of NWs and NBs after doping with indium oxide with thicker diameter and larger width to thickness ratios. TEM and SAED measurements confirms indium doping into ZnO lattice and resulting structure has high crystalline quality. We also observed a reduction in VE, indicating fewer oxygen vacancies and improved optical properties for doped NWs. The PL shows a redshift of peak energy for doped NWs and the carrier concentration is estimated according to Mott's critical density theory to be 5.5 x 10^{19} cm^{-3}. Emission peak at 3.34 eV for 1.6 at.% indium doped nanowires is found to be due to exciton bound to In site confirming that In atoms have been doped into the ZnO lattice. Low temperature PL spectra indicates that

D^0X merges and DAP recombination dominates at higher temperatures for indium doped NWs. Thermal quenching of PL at higher temperatures reveals activation energy for the donor and acceptor to be 32 meV and 9 meV respectively. Photoluminescence measurements shows that less doping concentrations of In_2O_3 from 3% -7% resulting in higher carrier concentrations as compared to as grown zinc oxide nanowires. Transmittance of greater than 90% is achieved for doped nanostructures from 3% -7% which can be used as a potential candidate for TCO. Our works provides a non-destructive way for estimating doping using PL measurements and suggests that *In* doping in ZnO NWs can be used for advancements in optoelectronics and spintronic devices.

7. CONCLUSIONS AND FUTURE WORK

7.1. Conclusions

The process of refining nanotechnology especially cutting edge photonic based devices requires knowledge of fundamental and diverse technologies along with nanosized semiconductor fabrication techniques where just a handful of atoms in any one of a dozen of processes can make the difference [191].

The preceding chapters have followed this theme and we have introduced device characterization as well optimization of CdTe/CdS based photodetectors and successful uniform gold nanodots arrays synthesis using block copolymer lithography as a power platform for many diverse applications. CdTe thin films have been grown using e-beam evaporation tool which has not been paid sufficient attention too in the past instead of commonly employed deposition techniques and reported excellent film purity. This thesis also presents a unique route to dope ZnO nanowires with transition metals using VLS growth technique and present a detailed defect state analysis with indium oxide doping proving enhanced optical properties which has not been explored sufficiently earlier. Also this is the first time VLS growth technique was used to dope ZnO NWs in our lab at UIC. Conditions for optimal and non-optimal growth of ZnO NWs were investigated. Varying some of the experimental growth conditions of ZnO resulted in very interesting complex structures such as star shaped and multilayer ZnO NWs growth. A unique way of estimating spontaneous polarization induced electric fields in ZnO nanostructure is explored using electrostatic force analysis. Lastly enhanced optical properties is achieved using indium oxide doped zinc oxide nanowires using VLS growth mechanism.

In the first part of thesis, we have presented characterization of CdS thin films deposited on ITO coated glass surfaces. CdS layer is often used as a window layer for photovoltaics applications as well as employed in many optoelectronic devices. As deposited and annealed CdS thin films are grown by thermal evaporation technique. We report multiple phonon Raman peaks up to fourth order for the annealed CdS nanocrystals and excellent film quality is revealed after annealing. We have shown asymmetry in the line shape of LO phonon modes to be attributed to the phonon confinement effects and fitted well with the spatial correlation model. Improved crystalline quality is achieved for annealed CdS films as compared to as-grown samples and detailed study on the line widths and integrated intensities ratio of 2-LO to 1-LO phonon modes is done. Asymmetry and wide broadness indicated from photoluminescence green emission peak around 2.42 eV is attributed to the sulfur deficiencies in CdS films. Excitation dependent photoluminescence and Raman spectra is taken to see any underlying recombination effects and band to band transition as well as improved CdS film quality is reported.

In the second part of thesis, we have characterized as deposited and $CdCl_2$ treated polycrystalline CdTe thin films deposited by e-beam evaporation techniques. As compared to the traditional chemical methods, physical method such as e-beam evaporation is used that tends to appear more promising candidate for growing active layer. Temperature dependent PL spectra reveal energy transitions at 1.577 eV which is assigned to electron to acceptor transition while a donor to acceptor transition occurs at 1.573 eV. A broad spectrum at 1.45 eV is associated with A-center chlorine based acceptor complex. AFM study on the grain sizes for as grown and chlorine treated films

revealed grains of 0.2 μm and approximately 2-3 μm respectively. Quasi mode nature for the LO phonon modes of mixed symmetry is observed from the Raman spectra of the polycrystalline CdTe structures at 166 cm^{-1} whereas A1 and TO modes at 118.9 cm^{-1} and 136.5 cm^{-1} respectively correspond to phonon vibrations from hexagonal Te structure indicating Te rich surface.

Later in the thesis, a simpler and flexible route to the fabrication of nanoscale arrays of Au metal dots and nanoporous films is presented. Block copolymer self-assembly is used to fabricate oriented cylindrical microdomains with potential use either as a positive or a negative template. In this context, the cylindrical patterns we obtained can be extended further into not only applications in photovoltaics but also fabrication of high-density arrays of more complex or striped patterns that can be utilized for bit-patterned media and in the semiconductor industry. After removal of cylinders and cleaning the pores with oxygen plasma etching, successful fabrication of highly dense Au nanoparticles is realized on the nanoporous film. These materials are anticipated to be of use in the fabrication of hybrid solar cells involving inorganic semiconductor nanorods grown using VLS methods.

Further growth conditions of ZnO nanowires is evaluated, discussed and optimized. As grown ultra- long single crystal zinc oxide nanowires have been grown in appropriate growth conditions whereas decreasing substrate temperature results in star-like complex ZnO nanostructures. As grown ZnO nanowires shows near band edge emission as well as strong green emission that is related to intrinsic dopants. Large concentrations of intrinsic dopants can cause high conductivity in the device that can be used in sensing applications. Nanostars show enhanced UV emission and less intrinsic

defects. Electrostatic force measurements shows electric field from ZnO nanowires and stars in the order of 10^8 V/cm due to built-in spontaneous polarization effects. Diameter dependent studies of zinc oxide nanowires reveals lower concentration of surface states for thicker nanowires. Results from anneal induced effects shows decrease in UV as well as green emission which is attributed to decrease in oxygen vacancies within ZnO nanowires. Raman studies of randomly oriented nanowires under appropriate growth conditions shows quasi phonon modes nature of the vibrational modes whereas Raman studies on modulating growth times helped choosing best growth conditions for the VLS growth of ZnO nanowires.

Key achievement was the doping and enhanced optical properties of zinc oxide nanowires using vapor liquid solid growth mechanism after incorporation with indium oxide resulting in enhanced optical properties. SEM images reveal formation of nanobelts and nanowires after doping with indium oxide with thicker diameter and larger width to thickness ratios. TEM and SAED measurements show nanobelts with a very high crystalline quality whereas a detailed. Reduction in visible emission after doping with 1.6 at.% indium oxide indicates fewer oxygen vacancies along with a red shift in visible emission. Carrier concentration is estimated according to Mott's critical density theory to be around 5.5 x 10^{19} cm^{-3}. Low temperature PL spectra indicates that D^0X merges and DAP recombination dominates at higher temperatures for indium doped NWs. Thermal quenching of PL at higher temperatures reveals activation energy for the donor and acceptor to be 32 meV and 9 meV respectively. Photoluminescence measurements on varying indium oxide concentrations shows that concentrations of In_2O_3 from 3% -11% results in band gap narrowing of zinc oxide nanowires whereas higher concentrations

does not facilitate band gap narrowing. Transmittance of greater than 90% is achieved for doped nanostructures from 3% -7% which can be used as a potential candidate for TCO.

7.2. Future Work

There are many challenges left with realizing some of these ideas in mature devices and I expect progress to continue, because this field has a lot of forward potential.

1. Optimization of polycrystalline thin films CdTe based detectors and passivation of recombination sites achieved in this work can be applied for applications in photovoltaics and IR detectors as well as can also be used for the detection of X-rays and gamma rays.
2. Dimensions of the nanoporous template achieved can be tuned by changing the molecular weight of block copolymer. Based on specific applications, dimensional feature of Au nanodots can be varied and this could be one of the future paths. Detailed analysis on the Au nanodots can be done and effect of plasmonics can be investigated.
3. Au nanodots arrays can be engineered to use as a template for the VLS growth of nanowires. This technique can also be used to develop a hybrid CdS/polymer based solar cell. Highly dense and ordered gold nanodots arrays achieved in this work can be used as a catalyst for VLS growth of CdS nanorods and polymer can be used as a subsequent layer. This can result in improved photo carrier collection and separation as well as improved absorption of carriers resulting in enhanced device efficiency.

4. Detailed analysis on the investigations of the electrical properties of doped ZnO NWs is suggested as future work of this study. Further doping in ZnO can be achieved using similar technique suggested in this work with other elements like *Ga, Cd, Co* and *Mn* depending on applications.

APPENDICES

APPENDIX A

- Chapter 3 page 24-34 has been reproduced from my own article published in Materials Research Express as:

  Farid, Sidra, Souvik Mukherjee, Hyeson Jung, Michael A. Stroscio, and Mitra Dutta. "Analysis on the structural, vibrational and defect states of chlorine treated polycrystalline cadmium telluride structures grown by e-beam evaporation." Materials Research Express 2, no. 2 (2015): 025007.

  Copyright information on IOP publications is mentioned in Appendix C

- Chapter 6 page 76-95 has been reproduced from my own article published in Applied Physics Letters as:

  Farid, S., S. Mukherjee, K. Sarkar, M. Mazouchi, M. A. Stroscio, and M. Dutta. "Enhanced optical properties due to indium incorporation in zinc oxide nanowires." Applied Physics Letters 108, no. 2 (2016): 021106.

  Copyright information on AIP publications is mentioned in Appendix B

- Chapter 2 page 13-15 has been reproduced from my own conference article published by AIP conference proceedings as:

  Farid, Sidra, Michael A. Stroscio, and Mitra Dutta. "Raman scattering investigations of CdS thin films grown by thermal evaporation." In PHONONS 2012: XIV International Conference on Phonon Scattering in Condensed Matter, vol. 1506, no. 1, pp. 45-48. AIP Publishing, 2012.

  Copyright information on AIP publications is mentioned in Appendix B

APPENDIX B

AIP POLICY ON THESES AND DISSERTATIONS

Reprinted from the American Institute of Physics official website.

"AIP permits authors to include their published articles in a thesis or dissertation. It is understood that the thesis or dissertation may be published in print and/or electronic form and offered for sale, as well as included in a university's repository. Formal permission from AIP is not needed. If the university requires written permission, however, we are happy to supply it."

APPENDIX C

IOP POLICY ON THESES AND DISSERTATIONS

Reprinted from IOP science official website.

"Upon transfer of copyright, IOP and/or the copyright owner grants back to authors a number of rights. These include the right to copy the article for teaching purposes, and to include the article in research theses or dissertations. Please include citation details and for online use, a link to the Version of Record. IOP's permission will be required for commercial use of an article published as part of your thesis."

APPENDIX D

IEEE POLICY ON THESES AND DISSERTATIONS

Reprinted from the Institute of Electrical and Electronics Engineers official website.

"Thesis / Dissertation Reuse:

The IEEE does not require individuals working on a thesis to obtain a formal reuse license, however, you may print out this statement to be used as a permission grant:

Requirements to be followed when using an entire IEEE copyrighted paper in a thesis:

1) The following IEEE copyright/ credit notice should be placed prominently in the references: [year of original publication] IEEE. Reprinted, with permission, from [author names, paper title, IEEE publication title, and month/year of publication]

2) Only the accepted version of an IEEE copyrighted paper can be used when posting the paper or your thesis on-line.

3) In placing the thesis on the author's university website, please display the following message in a prominent place on the website: In reference to IEEE copyrighted material which is used with permission in this thesis, the IEEE does not endorse any of [university/educational entity's name goes here]'s products or services. Internal or personal use of this material is permitted.

If applicable, University Microfilms and/or ProQuest Library, or the Archives of Canada may supply single copies of the dissertation."

CITED LITERATURE

[1] Feynman, R. P. (1960). There's plenty of room at the bottom. Engineering and science, 23: 22-36.

[2] Macilwain, C. (2000). Nanotech thinks big. Nature, 405(6788), 730-732.

[3] Toumey, C. (2009). Plenty of room, plenty of history. Nature nanotechnology,4(12), 783-784.

[4] Junk, A., & Riess, F. (2006). From an idea to a vision: there's plenty of room at the bottom. American journal of physics, 74(9), 825-830.

[5] Mukherjee, S., Meshik, X., Choi, M., Farid, S., Datta, D., Lan, Y., Poduri, S., Sarkar, K., Baterdene, U., Huang, C.E. and Wang, Y., (2015). A graphene and aptamer based liquid gated FET-like electrochemical biosensor to detect adenosine triphosphate, 14(8), 967 – 972.

[6] Xu, K., Purahmad, M., Brenneman, K., Meshik, X., Farid, S., Poduri, S., ... & Dutta, M. (2014). Design and Applications of Nanomaterial-Based and Biomolecule-Based Nanodevices and Nanosensors. In Design and Applications of Nanomaterials for Sensors (pp. 61-97). Springer Netherlands.

[7] Tittel, F. K., Richter, D., & Fried, A. (2003). Mid-infrared laser applications in spectroscopy. In Solid-State Mid-Infrared Laser Sources (pp. 458-529). Springer Berlin Heidelberg.

[8] Mukherjee, S., Farid, S., Stroscio, M.A. and Dutta, M., 2015, September. Modeling polycrystalline effects on the device characteristics of cdte based solar cells. In Computational Electronics (IWCE), 2015 International Workshop on (pp. 1-4). IEEE.

[9] Farid, S., Mukherjee, S., Jung, H., Stroscio, M.A. and Dutta, M., (2015). Analysis on the structural, vibrational and defect states of chlorine treated polycrystalline cadmium telluride structures grown by e-beam evaporation. Materials Research Express, 2(2), 025007.

[10] Driscoll, J. B., Ophir, N., Grote, R. R., Dadap, J. I., Panoiu, N. C., Bergman, K., & Osgood, R. M. (2012). Width-modulation of Si photonic wires for quasi-phase-matching of four-wave-mixing: experimental and theoretical demonstration. Optics express, 20(8), 9227-9242.

[11] Dankovic, T., Punchihewa, K. A. G., Zaker, E., Farid, S., Habibimehr, P., Feinerman, A., & Busta, H. (2012). Extension of Operating Range Towards Lower Pressures of MEMS-based Thermal Vacuum Gauges by Laser-Induced Heating. Procedia Engineering, 47, 1243-1246.

[12] Zaker, E., Farid, S., Selvaraj, S. K., Bhavanarayana, C., Sorto, D., Kaur, R., ... & Busta, H. (2012, July). Thermal-based MEMS vacuum gauges for measuring pressures from 10− 2 Torr to 10− 6 Torr. In Vacuum Nanoelectronics Conference (IVNC), 2012 25th International (pp. 1-2). IEEE.

[13] Bao, Q., & Loh, K. P. (2012). Graphene photonics, plasmonics, and broadband optoelectronic devices. ACS nano, 6(5), 3677-3694.

[14] Driscoll, J. B., Grote, R. R., Souhan, B., Dadap, J. I., Lu, M., & Osgood, R. M. (2013). Asymmetric Y junctions in silicon waveguides for on-chip mode-division multiplexing. Optics letters, 38(11), 1854-1856.

[15] Driscoll, J. B., Liu, X., Yasseri, S., Hsieh, I., Dadap, J. I., & Osgood, R. M. (2009). Large longitudinal electric fields (E z) in silicon nanowire waveguides.Optics express, 17(4), 2797-2804.

[16] Rohatgi, A. (1992). A study of efficiency limiting defects in polycrystalline CdTe/CdS solar cells. International journal of solar energy, 12(1-4), 37-49.

CITED LITERATURE (continued)

[17] Szeles, C. (2004). CdZnTe and CdTe materials for X-ray and gamma ray radiation detector applications. physica status solidi (b), 241(3), 783-790.

[18] Wald, F. V. (1977). Applications of CdTe. A review. Revue de Physique Appliquée, 12(2), 277-290.

[19] Levi, D., Albin, D., & King, D. (2000). Influence of surface composition on back-contact performance in CdTe/CdS PV devices. Progress in Photovoltaics: Research and Applications, 8(6), 591-602.

[20] Hawkins, G., & Hunneman, R. (2004). The temperature-dependent spectral properties of filter substrate materials in the far-infrared (6–40 μm). Infrared physics & technology, 45(1), 69-79.

[21] Pantazis, J., Huber, A., Okun, P., Squillante, M. R., Waer, P., & Entine, G. (1994). New, high performance nuclear spectroscopy system using Si-PIN diodes and CdTe detectors. Nuclear Science, IEEE Transactions on, 41(4), 1004-1008.

[22] Hoke, W. E., & Traczewski, R. (1983). Metal-organic vapor deposition of CdTe and HgCdTe films. Journal of applied physics, 54(9), 5087-5089.

[23] Dinan, J. H., & Qadri, S. B. (1985). Heteroepitaxial growth of ZnCdTe by molecular beam epitaxy. Journal of Vacuum Science & Technology A, 3(3), 851-854.

[24] Fiederle, M., Ebling, D., Eiche, C., Hofmann, D. M., Salk, M., Stadler, W., ... & Meyer, B. K. (1994). Comparison of CdTe, Cd 0.9 Zn 0.1 Te and CdTe 0.9 Se 0.1 crystals: application for γ-and X-ray detectors. Journal of crystal growth,138(1), 529-533.

[25] Takahashi, T., & Watanabe, S. (2001). Recent progress in CdTe and CdZnTe detectors. Nuclear Science, IEEE Transactions on, 48(4), 950-959.

[26] Kiefer, J. E., & Yariv, A. (1969). ELECTRO-OPTIC CHARACTERISTICS OF CdTe AT 3.39 AND 10.6 μ. Applied Physics Letters, 15(1), 26-27.

[27] Birkmire, R. W., McCandless, B. E., & Hegedus, S. S. (1992). Effects of processing on CdTe/CdS materials and devices. International journal of solar energy, 12(1-4), 145-154.

[28] Britt J and Ferekides C (1993) Appl. Phys. Lett. 62 2851-52.

[29] R. Karmakar, S. Mukherjee, A.Deyasi, "Numerical Analysis of Transmission Coefficient of Double Quantum Well Triple Barrier Structure for Variable Effective Mass using Transfer Matrix.", IESPC, IEEE, 2011.

[30] Farid S, Stroscio M A and Dutta M 2012 Phonons 2012: XIV Int. Conf. on Phonon Scattering in Condensed Matter (Ann Arbor, MI USA) vol. 1506 (AIP Publishing) pp 45-8

[31] S. Mukherjee, R. Karmakar, A. Deyasi, "Theoretical computation of transmission coefficient of double quantum well triple barrier structure in presence of electric field", Int. J. of Soft Computing. and Engineering (IJSCE), vol. 1, pp. 41-44, 2011.

[32] Steckel J S, Zimmer J P, Coe-Sullivan S, Stott N E, Bulović V and Bawendi M G 2004 Angew. Chem. Int. Ed. 43 2154-58

CITED LITERATURE (continued)

[33] Farid S, Purahmad M, Stroscio M A and Dutta M 2012 IEEE Computational Electronics (IWCE), 2012 15th Int. Workshop (Madison, WA) pp 1-3

[34] Gopal V, & Harrington J 2003 Opt. Express 11 3182-87

[35] Kim D K, Lai Y, Diroll B T, Murray C B and Kagan C R 2012 Nat. Commun. 3 1216

[36] Sakaide, R., & Shank, C. (1974). U.S. Patent No. 3,849,653. Washington, DC: U.S. Patent and Trademark Office.

[37] Dankovic T et al 2012 Procedia Engineering 47 1243-46

[38] Nair P K, Campos J and Nair M T S 1988 Semicon. Sci. Technol 3 134

[39] Wang Z, Zhang N, Brenneman K, Wu T C, Jung H, Biswas S and Dutta M 2012 Optoelectronic Applications of Colloidal Quantum Dots. InQuantum Dot Devices (New York: Springer) pp 351-67

[40] Fainer N I, Kosinova M L, Rumyantsev Y M, Salman E G and Kuznetsov F A 1996 Thin Solid Films 280 16-19

[41] Tong X L, Jiang D S, Li Y, Liu Z M and Luo M Z 2006 Physica B: Condensed Matter 382 105-109

[42] Conde O, Rolo A G, Gomes M J M, Ricolleau C and Barber D J 2003 Journal of crystal growth 247 371-380

[43] Feng, Z. C., Chou, H. C., Rohatgi, A., Lim, G. K., Wee, A. T. S., & Tan, K. L. (1996). Correlations between CdTe/CdS/SnO2/glass solar cell performance and the interface/surface properties. Journal of applied physics, 79(4), 2151-2153.

[44] Wu, X. (2004). High-efficiency polycrystalline CdTe thin-film solar cells. Solar energy, 77(6), 803-814.

[45] Elliott, C. T. (2001). Photoconductive and non-equilibrium devices in HgCdTe and related alloys. In Infrared Detectors and Emitters: Materials and Devices(pp. 279-312). Springer US.

[46] Peng, H. I., & Miller, B. L. (2011). Recent advancements in optical DNA biosensors: exploiting the plasmonic effects of metal nanoparticles. Analyst,136(3), 436-447.

[47] Mappes, T., Jahr, N., Csaki, A., Vogler, N., Popp, J., & Fritzsche, W. (2012). The Invention of Immersion Ultramicroscopy in 1912—The Birth of Nanotechnology. Angewandte Chemie International Edition, 51(45), 11208-11212.

[48] Edwards, P. P., & Thomas, J. M. (2007). Gold in a Metallic Divided State—From Faraday to Present-Day Nanoscience. Angewandte Chemie International Edition, 46(29), 5480-5486.

[49] Polavarapu, L., & Liz-Marzán, L. M. (2013). Towards low-cost flexible substrates for nanoplasmonic sensing. Physical Chemistry Chemical Physics,15(15), 5288-5300.

[50] Jun, Y. W., Seo, J. W., & Cheon, J. (2008). Nanoscaling laws of magnetic nanoparticles and their applicabilities in biomedical sciences. Accounts of chemical research, 41(2), 179-189.

CITED LITERATURE (continued)

[51] Matheu, P., Lim, S. H., Derkacs, D., McPheeters, C., & Yu, E. T. (2008). Metal and dielectric nanoparticle scattering for improved optical absorption in photovoltaic devices. Applied Physics Letters, 93(11), 113108.

[52] Manfrinato, V. R., Zhang, L., Su, D., Duan, H., Hobbs, R. G., Stach, E. A., & Berggren, K. K. (2013). Resolution limits of electron-beam lithography toward the atomic scale. Nano letters, 13(4), 1555-1558.

[53] Ruiz, R., Kang, H., Detcheverry, F. A., Dobisz, E., Kercher, D. S., Albrecht, T. R., ... & Nealey, P. F. (2008). Density multiplication and improved lithography by directed block copolymer assembly. Science, 321(5891), 936-939.

[54] Moore, J. S. (1997). Shape-persistent molecular architectures of nanoscale dimension. Accounts of chemical research, 30(10), 402-413.

[55] Lazzari, M., & López-Quintela, M. A. (2003). Block copolymers as a tool for nanomaterial fabrication. Advanced Materials, 15(19), 1583-1594.

[56] Lodge, T. P. (2003). Block copolymers: past successes and future challenges.Macromolecular chemistry and physics, 204(2), 265-273.

[57] Stevens, M. P. (1990). Polymer chemistry. New York: Oxford univ. press.

[58] Ulrich, R., Chesne, A. D., Templin, M., & Wiesner, U. (1999). Nano-objects with Controlled Shape, Size, and Composition from Block Copolymer Mesophases.Advanced Materials, 11(2), 141-146.

[59] Ray, D. (2013). Synthesis and characterization of block Copolymer-mediated gold nanoparticles.

[60] Russell, T. P., Hjelm Jr, R. P., & Seeger, P. A. (1990). Temperature dependence of the interaction parameter of polystyrene and poly (methyl methacrylate). Macromolecules, 23(3), 890-893.

[61] Darling, S. B. (2009). Block copolymers for photovoltaics. Energy & Environmental Science, 2(12), 1266-1273.

[62] Mansky P, Liu Y, Huang E, Russell T P and Hawker C 1997 Science 275 1458-1460

[63] Cheng J Y, Ross C A, Thomas E L, Smith H I and Vancso G J 2002 Appl. Phys. Lett. 81 3657-3659

[64] Darling S B 2009 Energy Environ. Sci. 2 1266-1273

[65] Kim, Felix Sunjoo, Guoqiang Ren and Samson A. Jenekhe 2010 Chem. Mater. 23 682-732

[66] Hamley I W 2004 Developments in block copolymer science and technology (J. Wiley)

[67] Yang, P. (2005). The chemistry and physics of semiconductor nanowires. MRS bulletin, 30(02), 85-91.

[68] Samuelson, L., Thelander, C., Björk, M. T., Borgström, M., Deppert, K., Dick, K. A., ... & Wallenberg, L. R. (2004). Semiconductor nanowires for 0D and 1D physics and applications. Physica E: Low-dimensional Systems and Nanostructures, 25(2), 313-318.

CITED LITERATURE (continued)

[69] Kind, H., Yan, H., Messer, B., Law, M., & Yang, P. (2002). Nanowire ultraviolet photodetectors and optical switches. Advanced materials, 14(2), 158.

[70] Cui, Y., Zhong, Z., Wang, D., Wang, W. U., & Lieber, C. M. (2003). High performance silicon nanowire field effect transistors. Nano letters, 3(2), 149-152.

[71] Johnson, J. C., Choi, H. J., Knutsen, K. P., Schaller, R. D., Yang, P., & Saykally, R. J. (2002). Single gallium nitride nanowire lasers. Nature materials,1(2), 106-110.

[72] Patolsky, F., Zheng, G., & Lieber, C. M. (2006). Nanowire-based biosensors.Analytical Chemistry, 78(13), 4260-4269.

[73] Chen, X., Wong, C. K., Yuan, C. A., & Zhang, G. (2013). Nanowire-based gas sensors. Sensors and Actuators B: Chemical, 177, 178-195.

[74] Kind, H., Yan, H., Messer, B., Law, M., & Yang, P. (2002). Nanowire ultraviolet photodetectors and optical switches. Advanced materials, 14(2), 158.

[75] Purahmad, M., Stroscio, M. A., & Dutta, M. (2014). Strong Enhancement of Near-Band-Edge Photoluminescence of ZnO Nanowires Decorated with Sputtered Metallic Nanoparticles. Journal of electronic materials, 43(3), 740-745.

[76] Lu, W., & Lieber, C. M. (2007). Nanoelectronics from the bottom up. Nature materials, 6(11), 841-850.

[77] Purahmad, M. (2013). Nanomaterials, Devices and Interface Circuits: Applications for Optoelectronic and Energy Harvesting (Doctoral dissertation, University of Illinois at Chicago).

[78] Cao, G. (2004). Synthesis, Properties and Applications. Imperial college press, London.

[79] Wang, Z. L. (2004). Zinc oxide nanostructures: growth, properties and applications. Journal of Physics: Condensed Matter, 16(25), R829.

[80] Park, W. I., Kim, D. H., Jung, S. W., & Yi, G. C. (2002). Metalorganic vapor-phase epitaxial growth of vertically well-aligned ZnO nanorods. Applied Physics Letters, 80(22), 4232-4234.

[81] Yu, H., Zhang, Z., Han, M., Hao, X., & Zhu, F. (2005). A general low-temperature route for large-scale fabrication of highly oriented ZnO nanorod/nanotube arrays. Journal of the American Chemical Society, 127(8), 2378-2379.

[82] S. Farid, M. Choi, D. Datta, M. A. Stroscio and M. Dutta, Spontaneous polarization induced electric field from zinc oxide nanowires and nanostars, *In preparation*

[83] Yang, Y., Jin, Y., He, H., Wang, Q., Tu, Y., Lu, H., & Ye, Z. (2010). Dopant-induced shape evolution of colloidal nanocrystals: the case of zinc oxide. Journal of the American Chemical Society, 132(38), 13381-13394.

[84] Fukumura, T., Jin, Z., Ohtomo, A., Koinuma, H., & Kawasaki, M. (1999). An oxide-diluted magnetic semiconductor: Mn-doped ZnO. Applied Physics Letters, 75(21), 3366-3368.

[85] Yang, Z. (2009). Doping in zinc oxide thin films.

CITED LITERATURE (continued)

[86] S. Farid, S. Mukherjee, K. Sarkar, M. Mazouchi, M. A. Stroscio and M. Dutta (2016). Enhanced optical properties due to indium incorporation in zinc oxide nanowires, Applied Physics Letters, 108, 021106

[87] Xu, Ke. "Graphene-based Nanostructures and DNA-based Biomolecule Sensors." (2014).

[88] Farid, S., Meshik, X., Choi, M., Mukherjee, S., Lan, Y., Parikh, D., Poduri, S., Baterdene, U., Huang, C.E., Wang, Y.Y. and Burke, P., (2015) Detection of Interferon gamma using graphene and aptamer based FET-like electrochemical biosensor. Biosensors and Bioelectronics, 71, 294-299.

[89] Chuu D S, Dai C M, Hsieh W F and Tsai C T 1991 Journal of applied physics 69 8402-8404.

[90] Dai C M, Horng L, Hsieh W F, Shih Y T, Tsai C T and Chuu D S 1992 Journal of Vacuum Science & Technology A 10 484-488

[91] Kale R B and Lokhande C D 2005 Semicon. Sci. Technol. 20 1

[92] Ingale A A, Mishra S, Roy U N, Tiwari P and Kukreja L M 2009 J. Appl. Phys. 106 084315

[93] Astratov V N, Bogomolov V N, Kaplyanskii A A, Prokofiev A V, Samoilovich L A, Samoilovich S M and Vlasov Y A 1995 II Nuovo Cimento D 17 1349-54

[94] Tsai C T, Chuu D S, Chen G L and Yang S L 1996 J.Appl. Phys. 79 9105

[95] Tell B, Damen T C and Porto S P S 1966 Phys. Rev. 144 771

[96] Shiang J J, Risbud S H and Alivisatos A P 1993 J. Chem. Phys. 98 8432-8442

[97] Debernardi A, Pyka N M, Gobel A, Ruf T, Lauck R, Kramp S and Cardona M 1997 Solid State Commun. 103 297

[98] Campbell I H, Fauchet P M 1986 Solid State Commun. 58 739

[99] Olego D J, Raccah P M and Faurie J P 1986 Phys. Rev. B 33 3819

[100] Paillard V, Puech P, Laguna M A, Carles R, Kohn B and Huisken F 1999 J. Appl. Phys 86 1921-24

[101]Sahoo S and Arora A K 2010 J. Phys. Chem. B 114 4199- 203

[102] Prabhu R R and Khadar M A 2008 Bull. Mater. Sci. 31 511-5

[103] Wang R P, Xu G, Jin P, 2004 Phys. Rev. B 69 113303

[104] Sivasubramanian V, Arora A K, Premila M, Sundar C S and Sastry V S 2006 Physica E: Low-dimensional Systems and Nanostructures 31 93-8

[105] Yang J, Meldrum F C and Fendler J H 1995 J. Phys. Chem. 99 5500

[106] Cousins M A and Durose K 2000 Thin Solid Films 361 253-257.

[107] Kampmann A, Cowache P, Vedel J and Lincot D 1995 Journal of Electroanalytical Chemistry 387 53-64.

CITED LITERATURE (continued)

[108] Aranda J, Morenza J L, Esteve J and Codina J M 1984 Thin Solid Films 120 23-30.

[109] Boone J L, Van Doren, T P and Berry A K 1982 Thin Solid Films 87 259-264.

[110] Gupta A and Compaan A D 2004 Applied Physics Letters 85 684-686.

[111] Duffy N W, Peter L M, Wang R L, Lane D W and Rogers K D 2000 Electrochimica acta 45 3355-3365

[112] Takacs L A, Kusner R E and Mearini G T 2001 Patent and Trademark Office Patent No. 6,244,212. Washington, DC: U.S

[113] Håkansson G, Hultman L, Sundgren J E, Greene J E and Münz W D 1991 Surface and Coatings Technology 48 51-67.

[114] Rose D H, Hasoon F S, Dhere R G, Albin D S, Ribelin R M, Li X S and Sheldon P 1999 Prog. Photovoltaics Res. Appl. 7 331-340.

[115] Moutinho H R, Al-Jassim M M, Levi D H, Dippo P C and Kazmerski L L 1998 J. Vac. Sci. Tech. A 16 1251-1257.

[116] Metzger W K, Albin D, Romero M J, Dippo P and Young M 2006 J. Appl. Phys. 99 103703-103703.

[117] Rohatgi A 1992 Int. J. Sol. Energy 12 37-49.

[118] de Moure-Flores F, Quiñones-Galván J G, Guillén-Cervantes A, Santoyo-Salazar J, Hernández-Hernández A, Olvera M and Meléndez-Lira M 2012 AIP Advances 2 022131.

[119] Krustok J, Valdna, V, Hjelt K and Collan H 1996 J. Appl. Phys. 80 1757-1762.

[120] Kosyak V, Opanasyuk A, Bukivskij P M and Gnatenko Y P 2010 J. Cryst. Growth 3121726-1730.

[121] Corwine C R, Sites J R, Gessert T A, Metzger W K, Dippo P, Li J and Teeter G 2005 Appl. Phys. Lett. 86 221909.

[122] Van Gheluwe J, Versluys J, Poelman D and Clauws P 2005 Thin Solid Films 480 264-268.

[123] Kraft C, Metzner H, Hädrich M, Reislöhner U, Schley P, Gobsch G and Goldhahn R 2010 J. Appl. Phys. 108 124503.

[124] C. Onodera and T. Taguchi 1990 J. Cryst. Growth 101 502

[125] Moutinho H R, Al-Jassim M M, Levi D H, Dippo P C and Kazmerski L L 1998 J. Vac. Sci. Tech. A 16 1251-1257.

[126] Metzger W K, Albin D, Romero M J, Dippo P and Young M 2006 J. Appl. Phys. 99 103703-103703.

[127] Furstenberg R and White J O 2007 J. Cryst. Growth 305 228-236

[128] N C Giles-Taylor, R N Bicknell, D K Blanks, T H Myersa and J F Schetzina 1985 J. Vac. Sci. Technol. A 3 76.

[129] Neu G, Marfaing Y, Legros R, Triboulet R and Svob L 1980 Journal of Luminescence 21 293-304.

CITED LITERATURE (continued)

[130] Krustok J, Madasson J, Hjelt K and Collan H 1997 J. Mater. Sci. 32 1545-1550.

[131] Morell G, Reynés-Figueroa A, Katiyar R S, Farías M H, Espinoza-Beltran F J, Zelaya-Angel O and Sánchez-Sinencio F 1994 J. Raman Spectrosc. 25 203-207.

[132] Sen B, Stroscio M and Dutta M 2011 J. Electron Mater. 40 2015-2019.

[133] Darling S B 2007 Prog. Polym. Sci. 32 1152-1204.

[134] Shin K et al. 2002 Nano Lett. 2 933-936.

[135] Wang Y, Meng G, Zhang L, Liang C and Zhang J 2002 Chem. Mater. 14 1773-1777.

[136] Tsukazaki, A., Ohtomo, A., Onuma, T., Ohtani, M., Makino, T., Sumiya, M., ... & Kawasaki, M. (2005). Repeated temperature modulation epitaxy for p-type doping and light-emitting diode based on ZnO. Nature materials, 4(1), 42-46.

[137] Heo, Y. W., Tien, L. C., Kwon, Y., Norton, D. P., Pearton, S. J., Kang, B. S., & Ren, F. (2004). Depletion-mode ZnO nanowire field-effect transistor. Applied Physics Letters, 85(12), 2274-2276.

[138] Chen, Z., Shan, Z., Cao, M. S., Lu, L., & Mao, S. X. (2004). Zinc oxide nanotetrapods. Nanotechnology, 15(3), 365.

[139] Wahab, R., Kim, Y. S., Mishra, A., Yun, S. I., & Shin, H. S. (2010). Formation of ZnO micro-flowers prepared via solution process and their antibacterial activity. Nanoscale research letters, 5(10), 1675-1681.

[140] Xing, Y. J., Xi, Z. H., Xue, Z. Q., Zhang, X. D., Song, J. H., Wang, R. M., ... & Yu, D. P. (2003). Optical properties of the ZnO nanotubes synthesized via vapor phase growth. Applied Physics Letters, 83(9), 1689-1691.

[141] Ye, J., Gu, S., Zhu, S., Chen, T., Hu, L., Qin, F., ... & Zheng, Y. (2002). The growth and annealing of single crystalline ZnO films by low-pressure MOCVD.Journal of Crystal Growth, 243(1), 151-156.

[142] Yao, B. D., Chan, Y. F., & Wang, N. (2002). Formation of ZnO nanostructures by a simple way of thermal evaporation. Applied Physics Letters, 81(4), 757-759.

[143] Sun, Y., Ndifor-Angwafor, N. G., Riley, D. J., & Ashfold, M. N. (2006). Synthesis and photoluminescence of ultra-thin ZnO nanowire/nanotube arrays formed by hydrothermal growth. Chemical Physics Letters, 431(4), 352-357.

[144] Baxter, J. B., & Aydil, E. S. (2005). Nanowire-based dye-sensitized solar cells.Applied Physics Letters, 86(5), 053114.

[145] http://en.wikipedia.org/wiki/Vapor%E2%80%93liquid%E2%80%93solid_method

[146] Kar, A. (2012). Defect Passivation in Nanowires and Demonstration of Nanowire Devices for Use in Sensing Applications (Doctoral dissertation, NASA, Ames Research Center).

[147] Gao, P. X., & Wang, Z. L. (2004). Nanopropeller arrays of zinc oxide. Applied physics letters, 84(15), 2883-2885.

[148] http://en.wikipedia.org/wiki/Surface_diffusion

CITED LITERATURE (continued)

[149] Liu, C., Zapien, J. A., Yao, Y., Meng, X. M., Lee, C. S., Fan, S. S., ... & Lee, S. T. (2003). High-Density, Ordered Ultraviolet Light-Emitting ZnO Nanowire Arrays. Advanced materials, 15(10), 838-841.

[150] Xing, Y. J., Xi, Z. H., Xue, Z. Q., Zhang, X. D., Song, J. H., Wang, R. M., ... & Yu, D. P. (2003). Optical properties of the ZnO nanotubes synthesized via vapor phase growth. Applied Physics Letters, 83(9), 1689-1691.

[151] Djurišić, A. B., & Leung, Y. H. (2006). Optical properties of ZnO nanostructures. Small, 2(8-9), 944-961.

[152] Park, W. I., Jun, Y. H., Jung, S. W., & Yi, G. C. (2003). Excitonic emissions observed in ZnO single crystal nanorods. Applied Physics Letters, 82(6), 964-966.

[153] Sun, Y., Ndifor-Angwafor, N. G., Riley, D. J., & Ashfold, M. N. (2006). Synthesis and photoluminescence of ultra-thin ZnO nanowire/nanotube arrays formed by hydrothermal growth. Chemical Physics Letters, 431(4), 352-357.

[154] Cross, R. B. M., De Souza, M. M., & Narayanan, E. S. (2005). A low temperature combination method for the production of ZnO nanowires.Nanotechnology, 16(10), 2188.

[155] Zhang, R., Yin, P. G., Wang, N., & Guo, L. (2009). Photoluminescence and Raman scattering of ZnO nanorods. Solid State Sciences, 11(4), 865-869.

[156] Stroscio, M. A., & Dutta, M. (2001). Phonons in nanostructures. Cambridge University Press.

[157] E.A. Llado, R. Cusco, L. Artus, J. Jimenez, B. Wang, and M. Callahan, J. Phys. Condens. Matter 20, 445211 (2008).

[158] C.A. Arguello, D.L. Rousseau, and S.P.S. Porto, Phys. Rev. 181, 1351 (1969).

[159] O. Lupan, L. Chow, L.K. Ono, B.R. Cuenya, G. Chai, H. Khallaf, S. Park, and A. Schulte, J. Phys. Chem. 114, 12401 (2010).

[160] Dal Corso, A., Posternak, M., Resta, R. and Baldereschi, A., 1994. Ab initio study of piezoelectricity and spontaneous polarization in ZnO. Physical Review B, 50(15), p.10715.

[161] Gopal, P. and Spaldin, N.A., 2006. Polarization, piezoelectric constants, and elastic constants of ZnO, MgO, and CdO. Journal of electronic materials,35(4), pp.538-542.

[162] Wang, Z.L., 2004. Nanostructures of zinc oxide. Materials today, 7(6), pp.26-33.

[163] Miyasato, K., Abe, S., Takezoe, H., Fukuda, A. and Kuze, E., 1983. Direct method with triangular waves for measuring spontaneous polarization in ferroelectric liquid crystals. Japanese Journal of Applied Physics, 22(10A), p.L661.

[164] Choi, M.S., Meshik, X., Mukherjee, S., Farid, S., Doan, S., Covnot, L., Dutta, M. and Stroscio, M.A., 2015. Electrostatic force analysis, optical measurements, and structural characterization of zinc oxide colloidal quantum dots synthesized by sol-gel method. Journal of Applied Physics,118(19), p.194304.

[165] Wang, N. W., Yang, Y. H., & Yang, G. W. (2009). Indium Oxide− zinc Oxide Nanosized Heterostructure and Whispering Gallery Mode Luminescence Emission. The Journal of Physical Chemistry C, 113(35), 15480-15483.

CITED LITERATURE (continued)

[166] Yang, Y., Jin, Y., He, H., Wang, Q., Tu, Y., Lu, H., & Ye, Z. (2010). Dopant-induced shape evolution of colloidal nanocrystals: the case of zinc oxide.Journal of the American Chemical Society, 132(38), 13381-13394.

[167] Morales, A. E., Zaldivar, M. H., & Pal, U. (2006). Indium doping in nanostructured ZnO through low-temperature hydrothermal process. Optical Materials, 29(1), 100-104.

[168] Shen, L., Wu, R. Q., Pan, H., Peng, G. W., Yang, M., Sha, Z. D., & Feng, Y. P. (2008). Mechanism of ferromagnetism in nitrogen-doped ZnO: First-principle calculations. Physical Review B, 78(7), 073306.

[169] Singh, G., Shrivastava, S. B., Jain, D., Pandya, S., Shripathi, T., & Ganesan, V. (2010). Effect of indium doping on zinc oxide films prepared by chemical spray pyrolysis technique. Bulletin of Materials Science, 33(5), 581-587.

[170] Biswal, R., Maldonado, A., Vega-Pérez, J., Acosta, D. R., & De La Luz Olvera, M. (2014). Indium Doped Zinc Oxide Thin Films Deposited by Ultrasonic Chemical Spray Technique, Starting from Zinc Acetylacetonate and Indium Chloride. Materials, 7(7), 5038-5046.

[171] Yadav, P., Mandalia, H. C., Pathak, C., & Pandey, K. (2012). Indium Doped Zinc Oxide Thin Films. International Journal of Chemical and Analytical Science, 3(3).

[172] Tahar, R. B. H., Ban, T., Ohya, Y., & Takahashi, Y. (1998). Tin doped indium oxide thin films: Electrical properties. Journal of Applied Physics, 83(5), 2631-2645.

[173] Y. W. Chen, Y. C. Liu, S. X. Lu, C. S. Xu, C. L. Shao, C. Wang, J. Y. Zhang, Y. M. Lu, D. Z. Shen, and X. W. Fan, The Journal of chemical physics 123, 134701 (2005).

[174] K. W. Liu, M. Sakurai and M. Aono, Journal of Applied Physics 108, 043516 (2010).

[175] K. Ellmer, A. Klein and B. Rech, Transparent conductive zinc oxide: basics and applications in thin film solar cells (Springer Science & Business Media, 2007) Vol. 104.

[176] J. Jie, G. Wang, X. Han, J. G. Hou, J. Phy. Chem. B 108, 17027 (2004).

[177] B. D. Yao, Y. F. Chan and N. Wang, Applied Physics Letters 81, 757 (2002).

[178] Y. Li, G. W. Meng, L. D. Zhang and F. Phillipp, Applied Physics Letters 76, 2011 (2000).

[179] H. Kumano, K. Hoshi, S. Tanaka, I. Suemune, X. Shen, P. Riblet, P. Ramvall and Y. Aoyagi, Applied physics letters 75, 19 (1999).

[180] Y. Kim, H. J. Joyce, Q. Gao, H. H. Tan, C. Jagadish, M. Paladugu, J. Zou and A. A. Suvorova, Nano letters 6, 4 (2006).

[181] B. E. Sernelius, K. F. Berggren, Z. C. Jin, I. Hamberg and C. G. Granqvist, Physical Review B 37, 10244 (1988).

[182] K. J. Kim and Y. R. Park, Applied Physics Letters 78, 475 (2001).

[183] A. Kar, M. A. Stroscio, M. Meyyappan, D. J. Gosztola, G. P. Wiederrecht and M. Dutta, Nanotechnology 22, 285709 (2011).

CITED LITERATURE (continued)

[184] H. P. He, Z. Wang, H. F. Duan and Z. Z. Ye, Physical Chemistry Chemical Physics 17, 17552 (2015).

[185] Q. Jijun, X. Li, W. He, S. Park, H. Kim, Y. Hwang, J. Lee and Y. Kim, Nanotechnology 20, 155603 (2009).

[186] L. Duan, B. Lin, W. Zhang, S. Zhong and Z. Fu, Applied physics letters 88, 232110 (2006).

[187] J. E. Stehr, K. M. Johansen, T. S. Bjørheim, L. Vines, B. G. Svensson, W. M. Chen and I. A. Buyanova, Physical Review Applied 2, 021001 (2014).

[188] E. Iliopoulos, D. Doppalapudi, H. M. Ng and T. D. Moustakas, Applied physics letters 73, 375 (1998).

[189] Fan, H. J., Fuhrmann, B., Scholz, R., Himcinschi, C., Berger, A., Leipner, H., ... & Zacharias, M. (2006). Vapour-transport-deposition growth of ZnO nanostructures: switch between c-axial wires and a-axial belts by indium doping. Nanotechnology, 17(11), S231.

[190] http://en.wikipedia.org/wiki/Surface_energy

[191] Driscoll, J. B. (2014). Silicon Photonics: All-Optical Devices for Linear and Nonlinear Applications.

VITA

NAME SIDRA FARID

EDUCATION PhD, University of Illinois at Chicago, 2016

M.S., University of Engineering & Technology, Lahore, 2009

B.Sc., University of Engineering & Technology, Lahore, 2006

EXPERIENCE Graduate Technical Intern, Intel Corporation, CA, USA 2013-2014

Hardware Validation Intern, Facebook Inc. CA, USA May 2015-Aug 2015

Research Assistant at Argonne National Laboratory, IL, USA 2012-2013

Research Assistant at Electrical and Computer Engineering Department, UIC, USA 2010-2016

Teaching Assistant at at Electrical and Computer Engineering Department, UIC, USA Jan 2016- May 2016

Lecturer at Electrical Engineering Department, University of Engineering & Technology, Lahore 2006-2010

Intern at Innovative Automation Limited, Lahore May 2004- Aug 2004

HONORS Fulbright Scholar, Institute of International Education (IIE), USA 2010- 2015

Graduate Student Representative, ECE Deptt., University of Illinois Chicago 2011-2012

Graduate Student Travel Award, University of Illinois Chicago 2012

VITA (continued)

PUBLICATIONS **Journal Publications**

Sidra Farid, Souvik Mukherjee, Ketaki Sarkar, Mojgan Mazouchi, Michael A.Stroscio and Mitra Dutta, " Enhanced optical properties due to indium incorporation in zinc oxide nanowires ", *Applied Physics Letters*, 108(2), 021106, 2016

Sidra Farid, Souvik Mukherjee, Hyeson Jung, Michael A. Stroscio and Mitra Dutta, " Analysis on the structural, vibrational and defect states of chlorine treated polycrystalline cadmium telluride structures grown by e-beam evaporation ", *Materials Research Express*, 2(2), 025007, 2015

Sidra Farid *et al.,* "Detection of Interferon Gamma using graphene and aptamer based FET-like electrochemical biosensor", *Biosensors and Bioelectronics,* 71, 294-299, 2015

Min S Choi, Xenia Meshik, Souvik Mukherjee, **Sidra Farid**, Samuel Doan, Leigha Covnot, Mitra Dutta, Michael A Stroscio, "Electrostatic force analysis, optical measurements, and structural characterization of zinc oxide colloidal quantum dots synthesized by sol-gel method", *Journal of Applied Physics,* 118(19), 194304, 2015

Souvik Mukherjee, Xenia Meshik, Min Choi, **Sidra Farid**, Debopam Datta, Yi Lan, Shripriya Poduri, Ketaki Sarkar, Undarmaa Baterdene, Ching-En Huang, Yung Wang, Peter Burke, Mitra Dutta, Michael Stroscio, "A graphene and aptamer based liquid gated FET-like electrochemical biosensor to detect adenosine triphosphate" *IEEE Transactions on NanoBioscience*, 14(8), 967 – 972, 2015

Xenia Meshik, Min Choi, Adam Baker, R Malchow, Leigha Covnot, Samuel Doan, Souvik Mukherjee, **Sidra Farid**, Mitra Dutta, Michael Stroscio, "Modulation of voltage-gated conductances of retinal horizontal cells by UV-excited TiO2 nanoparticles" *In Press*, Feb 2016

Xenia Meshik, **Sidra Farid**, Min Choi, Yi Lan, Souvik Mukherjee, Debopam Datta, Mitra Dutta, and Michael A. Stroscio, Biomedical Applications of Quantum Dots, Nucleic-acid-based Aptamers, and Nanostructures for Biosensors, Critical Reviews™ in Biomedical Engineering, *In Press* 2015

VITA (continued)

Sidra Farid *et al.,* "Spontaneous polarization induced electric field in Zincoxide nanowires and nanostars", *In Press*

Sidra Farid *et al.*, "Multiphonon resonant Raman scattering and photoluminescence studies of cadmium sulphide nanocrystals", *In preparation*

Sidra Farid *et al.*, "Exploring indium concentration effects on the optical properties of zinc oxide nanowires", *In preparation*

Book Chapter

Xu, Ke, Mohsen Purahmad, Kimber Brenneman, Xenia Meshik, **Sidra Farid**, Shripriya Poduri, Preeti Pratap *et al.* "Design and Applications of Nanomaterial-Based and Biomolecule-Based Nanodevices and Nanosensors." In Design and Applications of Nanomaterials for Sensors, pp. 61-97. Springer Netherlands, 2014. (Book Chapter) http://link.springer.com/chapter/10.1007/978-94-017-8848-9_3

Conference Publications & Presentations

Souvik Mukherjee, **Sidra Farid**, Michael A.Stroscio and Mitra Dutta, "Modeling polycrystalline effects on the device characteristics of CdTe based solar cells", In International Workshop on Computational Electronics (IWCE) 2015, pp. 1-4. IEEE, 2015.

Sidra Farid, Mohsen Purahmad, Michael A. Stroscio and M. Dutta, "Computational analysis on the emission of ZnO Nanowires and coreshell CdSe/ZnS quantum dots deposited on different substrates", International Workshop on Computational Electronics (IWCE), pp.1-3 , May 2012

Sidra Farid, Michael A. Stroscio and Mitra Dutta, "Raman Scattering investigations of CdS thin films grown by Thermal Evaporation", AIP Conf. Proc. 1506, pp. 45-48, Volume 1506, Phonons 2012 , July 2012

Evan Zaker, **Sidra Farid** *et al.* ,"Thermal-based MEMS vacuum gauges for measuring pressures from 10−2 Torr to 10−6 Torr", Vacuum Nanoelectronics Confer (IVNC), 2012

VITA (continued)

Tatjana Dankovic, Kasun Anupama Gardiye Punchihewa, Evan Zaker, **Sidra Farid**, Payam Habibimehr, Alan Feinerman, Heinz Busta, "Extension of Operating Range Towards Lower Pressures of MEMS-based Thermal Vacuum Gauges by Laser-Induced Heating", Procedia Engineering, Volume 47, 2012, Pages 1243–1246

Sidra Farid, Michael A.Stroscio and Mitra Dutta, "Investigation of anneal induced recrystallization properties of CdTe thin films", MSME 2014, March 2014 (Oral Presentation)

Sidra Farid, Michael A. Stroscio and Mitra Dutta, "Modeling CdS/CdTe interface properties for improving solarcell photoelectric quantum yield", AAAS, Feb 2014 (Poster Presentation)

Sidra Farid, Michael A. Stroscio and Mitra Dutta , "Optical Characterization Of CdS Window Layer For CdTe/CdS Based Solar Cell", APS/CNM/EMC 2012 User meeting (Poster Presentation)

Michael A. Stroscio, Mitra Dutta, Xenia Meshik, **Sidra Farid** *et al.*, "Nanotechnology-based Tools for the Study of the Affinity and Selectivity of Antigens for Small Molecular Targets Underlying Drug Discovery and Therapeutics", Drug Discovery & Therapy World Congress 2015, July 22-25, 2015, Boston, MA, USA

Sidra Farid, "Nanostructures, Nanowires and device characterization for applications in Optoelectronic devices and Energy harvesting", **National University of Singapore (NUS)** (Invited Talk), Oct 2014 http://www.nusnni.nus.edu.sg/events/nanostructures-nanowires-and-device-characterization-for-applications-in-optoelectronic-devices-and-energy-harvesting/